This is to certify that the

thesis entitled

EXPERIMENTAL CHARACTERIZATION OF A
[redacted] COMPACT MPDR PLASMA SOURCE
EMPLOYING THREE DIFFERENT COUPLING GEOMETRIES.

presented by

AMIR HALIM KHAN

has been accepted towards fulfillment
of the requirements for

Master's degree in Electrical Engineering

Major professor
Dr. Jes Asmussen

Date 5/5/99

EXPERIMENTAL CHARACTERIZATION OF A COMPACT MPDR PLASMA SOURCE EMPLOYING THREE DIFFERENT COUPLING GEOMETRIES.

By

Amir Halim Khan

A THESIS

Submitted to

Michigan State University

in partial fulfillment of the requirements

for the degree of

MASTER OF SCIENCE

Department of Electrical Engineering

1999

ABSTRACT

EXPERIMENTAL CHARACTERIZATION OF A COMPACT MPDR PLASMA SOURCE EMPLOYING THREE DIFFERENT COUPLING GEOMETRIES.

By

Amir Halim Khan

In this thesis three compact microwave plasma disc reactor (MPDR) plasma sources, i.e. MPDR 7 - Side Feed (SF), MPDR 7 - End Feed Probe (EFP) and MPDR 7 - End Feed Loop (EFL), have been experimentally characterized by varying the input variables space (U_1) and keeping the reactor geometry variables space (U_2) fixed. The influence of three different coupling structures on the plasma source performance have been evaluated and compared with the global plasma model.

The measured internal variables (X) and output variables (Y) for the three plasma sources are: 1) plasma density, 2) absorbed power, 3) ion saturation current, 4) electron temperature, and 5) ion production costs. Additionally, electron energy distribution function, plasma potential, absolute and spatial electric fields are measured for the side feed excitation. The experimental technique involves single and double Langmuir probe measurements and E-field probe measurements.

The performance of the three investigated sources are compared in terms of ion production costs. The performance predictions from the global plasma model and the experimental results are compared and the differences are analyzed. Finally, an improved plasma source design is proposed.

Dedicated to my parents, my wife, and our sons Waleed and Saif

ACKNOWLEDGEMENTS

I would like to thank Dr. Jes Asmussen for his continuous guidance and support which helped in developing skills that were required to carry out this research. My special thanks goes to Mark Perrin for his training, useful discussions and the time we made enjoyable in the laboratory. I extend my thanks to Dr. Timothy Grotjohn who was always there to assist us during experiments. I would like to thank Dr. Don Reinhard for being my committee member. Finally, I would thank Jay Kumar for being an excellent team member.

TABLE OF CONTENTS

Chapter 2

Experimental systems

Chapter 3

Experimental techniques

Chapter 4

Experimental Results

Chapter 5

Conclusion

LIST OF TABLES

LIST OF FIGURES

Chapter 1

Chapter 2

Chapter 3

Chapter 4

Chapter 1

Introduction

1.1 Research motivation

Impact of integrated circuit (IC) technology on our lives has been pervasive, and its domain ranges from consumer goods to information technology, from business management to manufacturing control. As a result of the exponential growth in IC fabrication processes, very large scale (VLSI) and Ultra large-scale integrated circuitry (ULSI) has made a single chip so dense that it bears tens of thousands of transistors. Figure 1.1 displays the critical dimensions of a single transistor embedded on a silicon wafer. This dramatic reduction in terms of feature size, and supply voltage, and the enhancements in processor speed and storage capacity is shown in the Table 1.1. The quest for an optimum processing speed, minimal dissipated power, least device failure rate, compact circuit area, blended with a fierce cost competition has revolutionized the electronic industry. In order to meet the dynamic consumer requirements, manufacturing groups in the IC industry should be equipped with all the tools that permit them to face this challenge.

For some time in the semiconductor industry low-pressure gas discharges or plasmas have been one of the process tools that have enabled the etching of anisotropic sub-micron features. Besides sub-micron anisotropic etching, many additional plasma based applications exist in the automotive, aerospace, biomedical and steel manufacturing industries. Plasmas are also being utilized in material processing such as plasma assisted crystal growth, i.e. in particular plasma assisted CVD diamond film growth. The last two decades have seen high density plasma sources, such as electron cyclotron resonance (ECR) based plasma processing machines edging out parallel plate plasma sources in terms of high plasma density, high etch rate, low sheath potential etc. These plasma processing ECR reactors can be configured in a number of ways [1] e.g. Slot-Antenna (SLAN) reactors, Divergent Field ECR reactor, Cylindrical Distributed ECR reactor (DECR), Uniform Distributed ECR reactor (UDECR) etc. An additional ECR concept, the multi-polar ECR reactor or microwave plasma disc reactor (MPDR), which was developed and patented by Michigan State University researchers [2], is the subject of this thesis research. These computer-controlled reactors have been demonstrated to fulfill the highest level of process uniformity and process speed which are the required criteria for the contemporary 0.35μm IC fabrication industry [1].

Even though the microwave plasma disc reactor (MPDR) ion/plasma sources have matured into a commercial product, there still are a number of unanswered questions related to the performance of these sources. The motivation for manipulating the complex chemical, physical and electromagnetic reactions within the gas discharge generated by MPDR ion sources is to obtain selectivity, stability and controllability in the plasma processing mechanism. Thus, in sequel to the on going experimental evaluation of MPDR ion sources, this study builds upon the research of earlier investigators and aims at design optimization of MPDR plasma sources developed at MSU.

Technology	Year				
	1992	1994	1996	1998	2000
Channel Length(μm)	0.5	0.4	0.3	0.2	0.1
DRAM Bits(MB)	16	64	64	256	256
Supply Voltage(V)	3.3/5.0	3.3	2.5	2.5/3.3	2.5
Logic Gates (x 1000)	200	400	600	1000	2000
Supply Voltage(V)	3.3	3.3	2.5	2.5	1.5
Processor Speed(MHz)	50	100	150	200	500

Table 1.1 The trend in IC growth

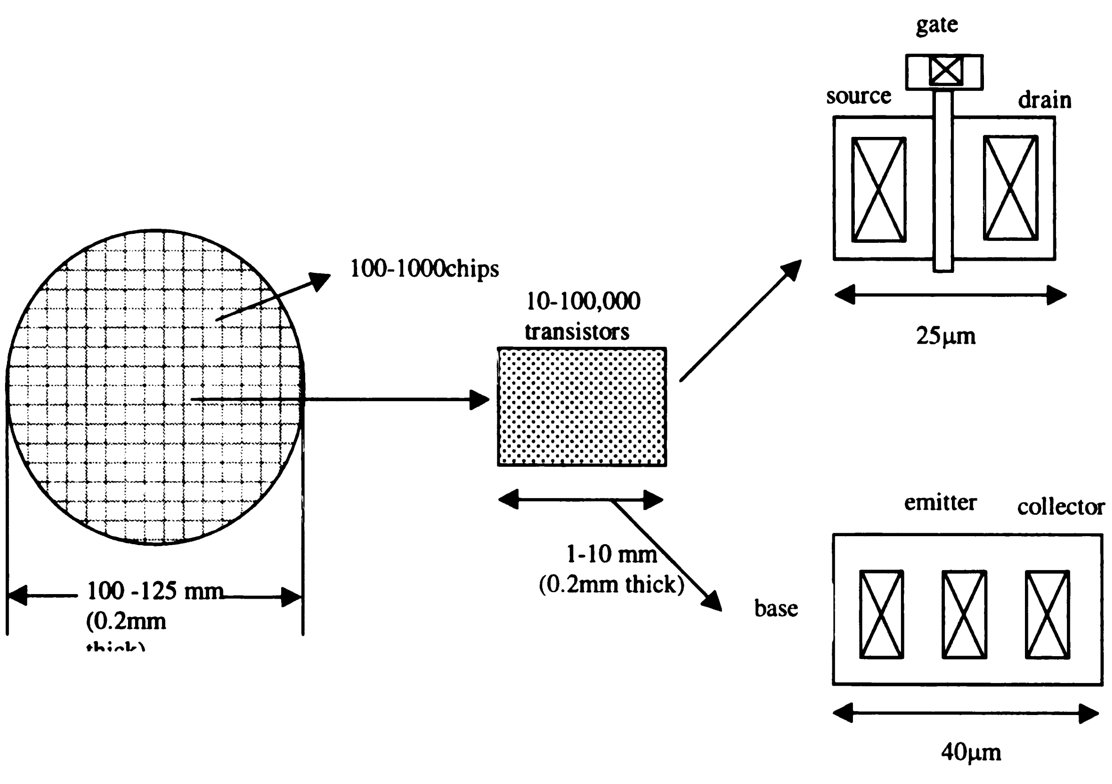

Figure 1.1 Silicon wafer, IC, and transistor

1.2 Generic microwave plasma reactor

1.2.1 Physical description and operation

Although the MPDR sources exist in a number of geometrical configurations, for ease in understanding the fundamental concepts they can be represented by a generic reactor model. Figure 1.2 displays a generic low-pressure microwave plasma processing reactor and Figure 1.3 displays typical applications of ECR plasma reactors, i.e. as an ion beam source and a plasma processing source. The typical reactor can be broadly divided in two parts: 1) the plasma source and 2) process chamber. The plasma source consists of three sub-assemblies: a) microwave cylindrical cavity applicator and matching network, b) discharge chamber and c) ECR magnets. The cylindrical cavity shell is usually made from either brass or stainless steel. A sliding short plate forms its top, and the bottom contains the quartz discharge chamber. Once the high vacuum pump brings the system to a low base pressure, the process gas is let in. The microwave applicator focuses the microwave energy into the discharge chamber and creates a microwave discharge. This discharge or plasma consists of charged particles and chemically active radicals. As shown in Figure 1.3a, these species diffuse out through the discharge chamber (quartz) opening at the $z = 0$ plane into the processing chamber. Alternately, as shown in the Figure 1.3b, a single or a set of double accelerating grids located at the source output, i.e. at the $z = 0$ plane, can be utilized to extract an ion beam from the source. The radius and height of the quartz dome, 'R' and 'L' defines the discharge volume. The radius 'R_C' and length 'L_C' bounds the cylindrical process chamber. The process zone is defined by a substrate of radius 'R_S' which is positioned downstream at a $z > 0$ plane. This substrate is mounted on an adjustable holder. The operating chamber pressure is maintained by continuously pumping down the working gas.

In low-pressure discharges the mean free path of radicals is much larger than the reactor's dimensions. Thus in contrast to high-pressure discharges they are dominated by wall recombination instead of volume recombination. The low-pressure discharges require the presence of strong external magnetic fields, which are provided either by permanent magnets or electromagnetic coils. The magnetic fields reduce the surface diffusion losses to the walls and assist in the discharge stability and improve the reactor efficiency.

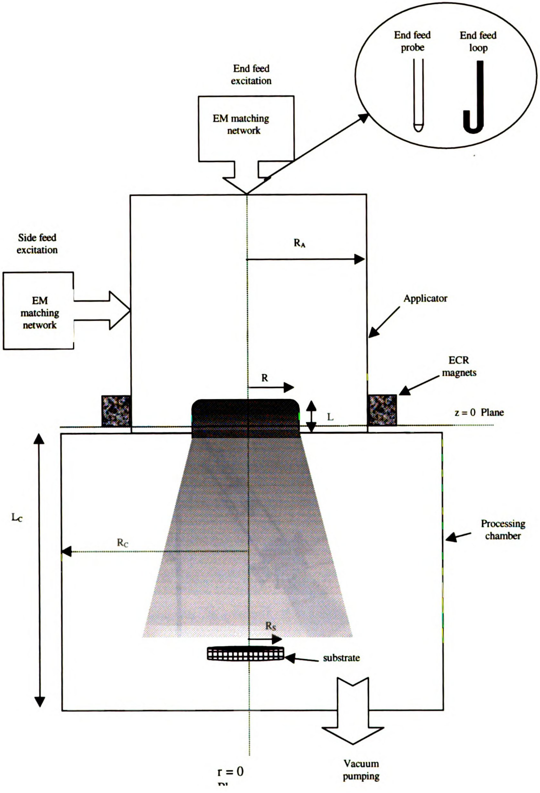

Figure 1.2 The generic ECR reactor

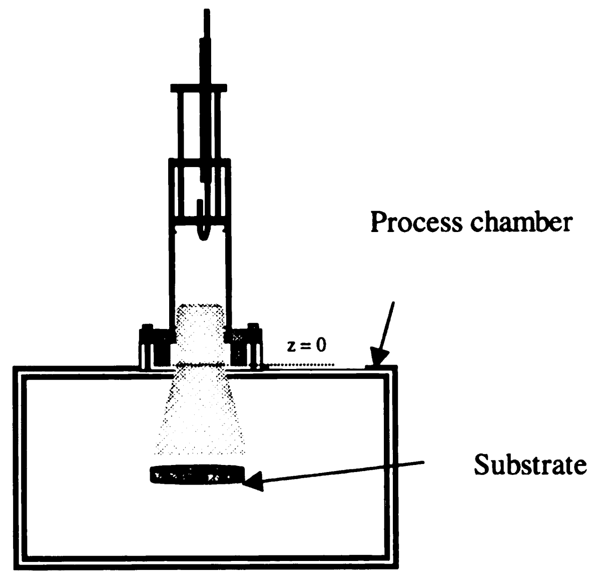

Figure 1.3a Plasma processing source

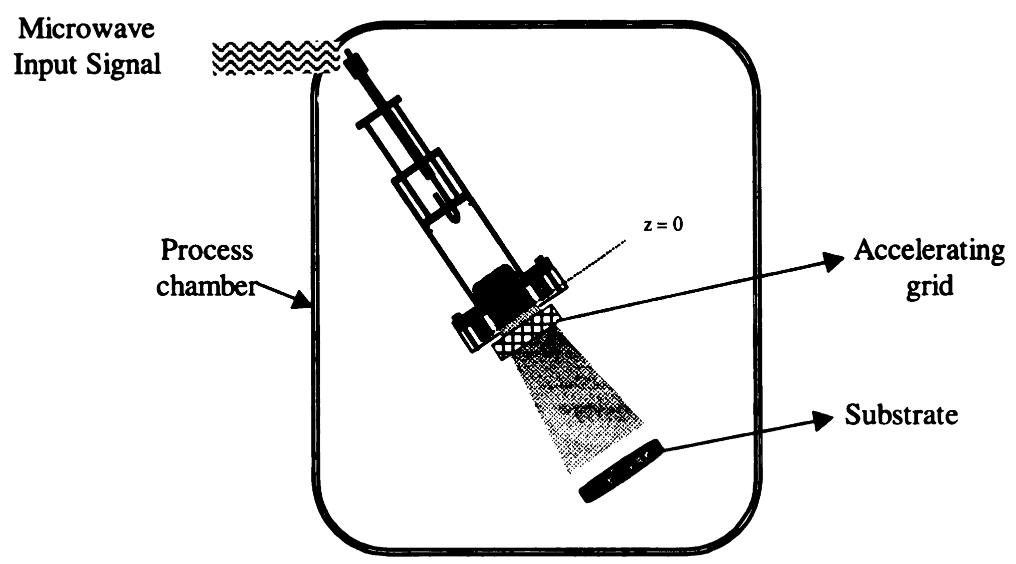

Figure 1.3b Ion beam source

Figure 1.3 - ECR plasma reactor applications

1.2.2 The multivariable plasma reactor

The plasma reactor is a highly nonlinear electronic device that is dependent on a number of experimental variables. The generic representation of these variables is illustrated in the Figure 1.4. It is seen that a host of variables have been grouped together to form a three variable vector space: 1) input variable vector (U), 2) internal variable vector (X) and 3) output variable vector (Y).

The input variable (U) is an independent controllable vector space, which is sub-divided in four vectors U_1, U_2, U_3 and U_4. The variables U_1 are comprised of macroscopic controllable input variables such as absorbed power (P_{abs}), operating chamber pressure, gas type, flow rate etc. The variables U_2 relate to the reactor geometry such as the applicator size, excitation geometry etc. The input variables U_3 consist of substrate processing procedures and include process control cycle, discharge initiation etc. The variables U_4 are related to substrate control and are comprised of substrate preparation, the bias and temperature of substrate holder, etc.

The internal plasma variables (X) are dependent upon the input variables (U). The internal variables (X) describe, in general, the variables associated with internal plasma dynamics. The internal variables (X) include plasma potential, charged species energy distribution functions, absorbed microwave power (P_{abs}), spatial electric field pattern, uniformity in the density profile etc.

The output variables (Y) can include all the parameters related to the desired reactor output. They are a function of both input and internal variables. They can be further sub-divided into reactor performance figures of merit (Y_1) and process output variables (Y_2). Reactor performance figures of merit (Y_1) include ion production cost, microwave coupling efficiency, stability, controllability etc. The process output variables (Y_2) consist of processing rate, substrate damage, surface morphology etc.

Researchers are still laboring hard to establish a theory governing the nonlinear relationships between the plasma source variables. A comprehensive understanding of these complex variables and their interdependence is essentially required for optimal machine design and process control.

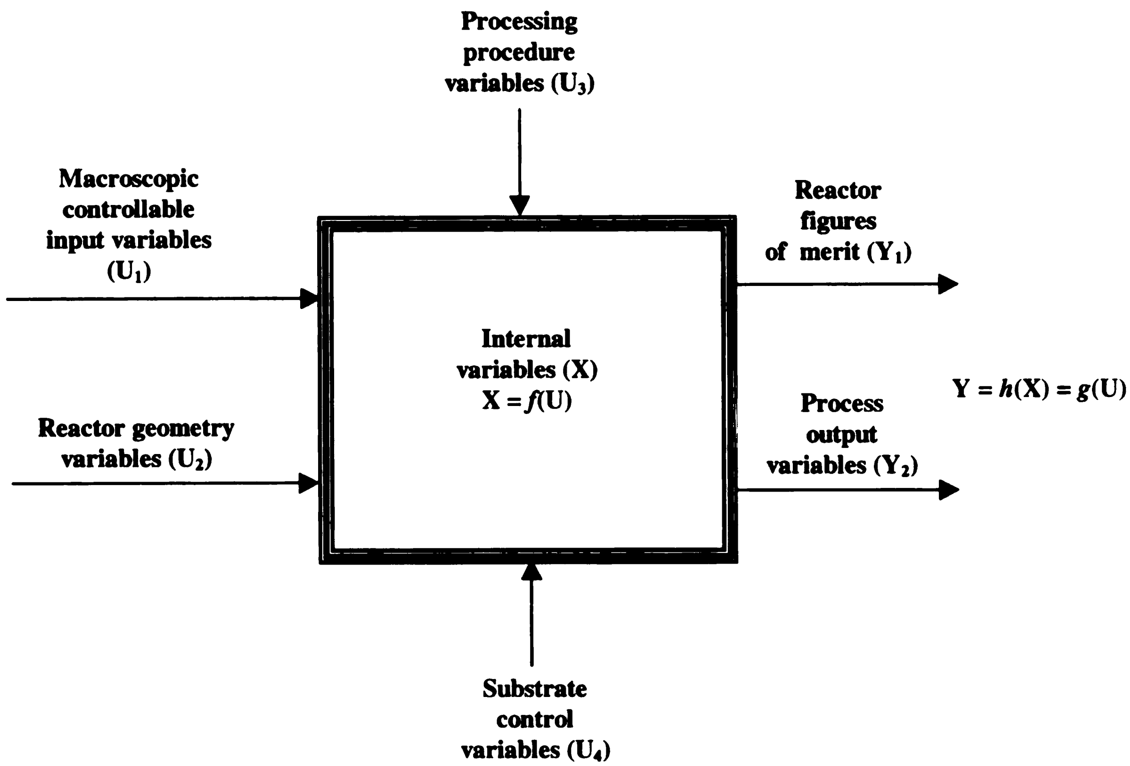

Figure 1.4 Generic plasma processing machine - System variables block diagram

1.3 Evolution of MPDR sources at MSU

The genesis of microwave plasma disc reactor (MPDR) took place at MSU in early 80's when J. Root and J. Asmussen [4] presented the idea of an electrodeless plasma source and introduced a first reactor of this kind in 1982. Since then this concept has been evaluated and optimized and researchers have developed plasma sources that are now being used in a number of commercial applications.

Figure 1.5 reviews the historical development of MPDR plasma sources at MSU. The first MPDR prototype was a brass cylindrical cavity employing a side feed microwave coupling configuration. Besides the stable sustenance of plasma through direct microwave coupling, this innovative plasma source demonstrated maximum coupling efficiency by employing an internal tuning mechanism. A few years later (1984), M. Dahimene [5, 6] demonstrated second prototype of plasma source, which used permanent magnets to overcome the difficulties of low-pressure (<1 torr) operation. This reactor was developed further [7] and is now known as the MPDR 9 plasma source, since the discharge diameter of the plasma source was approximately 9cm (to be precise 9.4cm). The experiments with MPDR 9 demonstrated that this source has a low ion beam current. L. Mahoney [8] in 1989 redesigned the base plate of MPDR 9, which accommodated a 5cm discharge. Thus without carrying out any major changes the MPDR 9 was transformed into MPDR 5 source. This source improved the ion production cost by a factor of two and was able to produce ion current densities of the order $10mA/cm^2$ [9]. The MPDR 5 used a cylindrical cavity shell of 17.8cm inner diameter. Later Mahoney reduced the applicator's shell diameter to 8.9cm and this source is now recognized as the MPDR 7 side feed plasma source. Additionally, an even smaller and more compact plasma source was developed in 1990. This source, which is now identified as the MPDR 610, was characterized by A. Srivastava [10]. A third transformation resulted in the MPDR 20. F. Sze [11, 12] in 1993 investigated this 20cm diameter ECR plasma source. He also characterized a larger 25cm diameter discharge called the MPDR 325 source [13]. This source has been commercialized by Wavemat Inc. MPDR 13 sources in both side and end feed configuration were studied by P. Mak in 1997 [14]. Recently the MPDR 7 End Feed Loop plasma source was characterized by M. Perrin in 1996 [15].

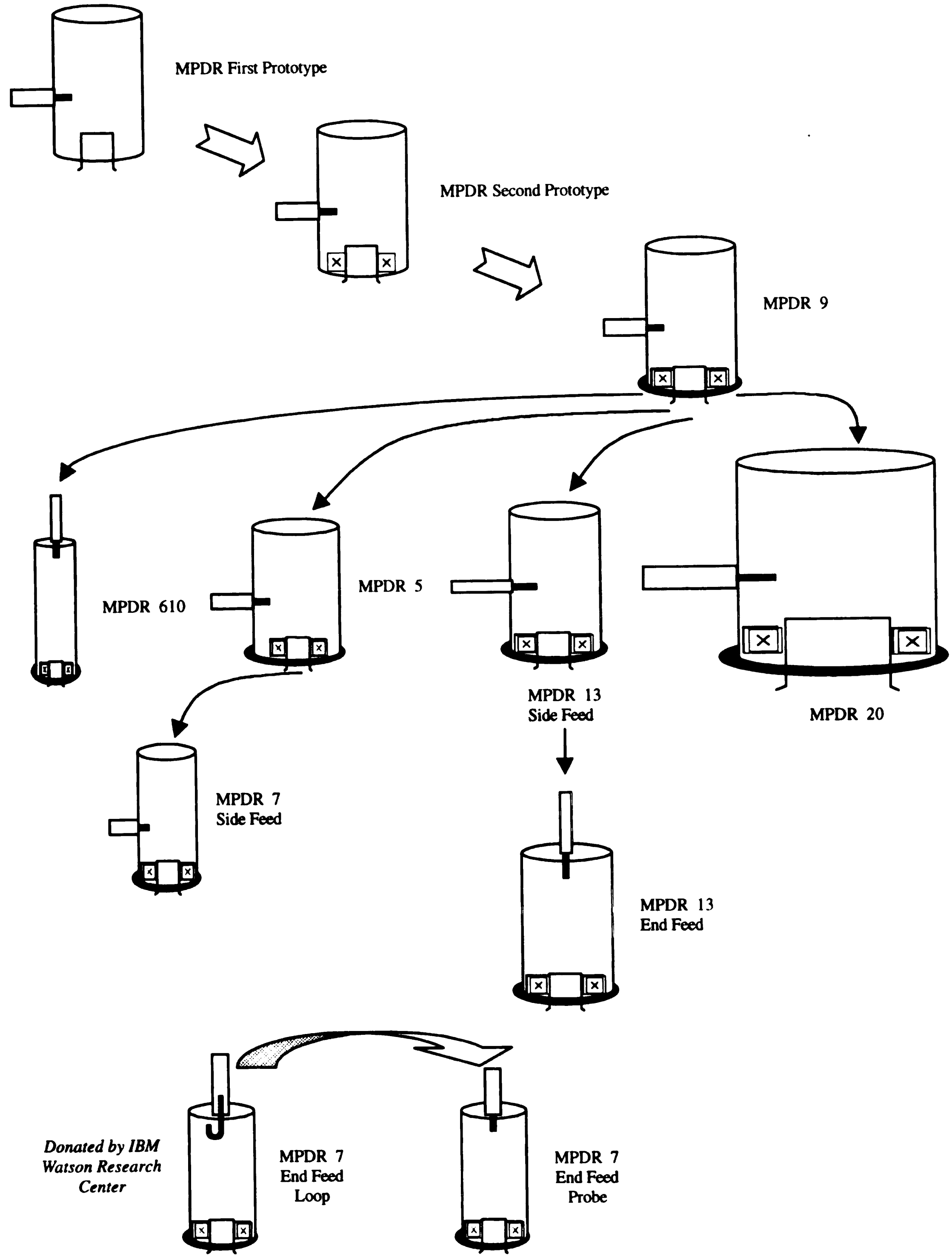

Figure 1.5 Evolution of MPDR sources at MSU

1.4 Brief description of the plasma sources investigated in this thesis

In order to draw a simple understanding of complex plasma systems, it would be first convenient to investigate small diameter MPDR sources. The research work described here spanned approximately one year and focussed on three compact MPDR sources, namely MPDR 7 – Side feed (SF), MPDR 7 – End Feed Probe (EFP), and MPDR 7 – End Feed Loop (EFL). Figures 1.6 – 1.8 give a schematic representation of these plasma sources. The applicator for all the three sources consists of a cylindrical cavity shell. For the side feed coupling configuration this shell is brass, and in the case of end excited sources it is stainless steel. The diameter of the end feed excitation geometry is slightly larger (9.8cm as compared to 8.9 cm) than the side feed source. The family of MPDR plasma sources is characterized by the user's control over the propagating mode in the microwave cavity applicator. Microwave power is coupled through the side feed or end feed excitation antennas. The sliding short end plates and the excitation antenna provide a two-dimensional internal tuning mechanism for discharge matching and electromagnetic mode selection.

The cavity applicator sits on a quartz discharge chamber where the plasma discharge is ignited using a noble gas. The electron cyclotron resonance (ECR) magnets, in an alternating pole configuration, surround the discharge chamber in a circular fashion. They serve to provide the necessary ECR region which is required to sustain a low-pressure discharge. The operation and physical description of these ion and plasma sources are discussed in much more detail at Chapter2.

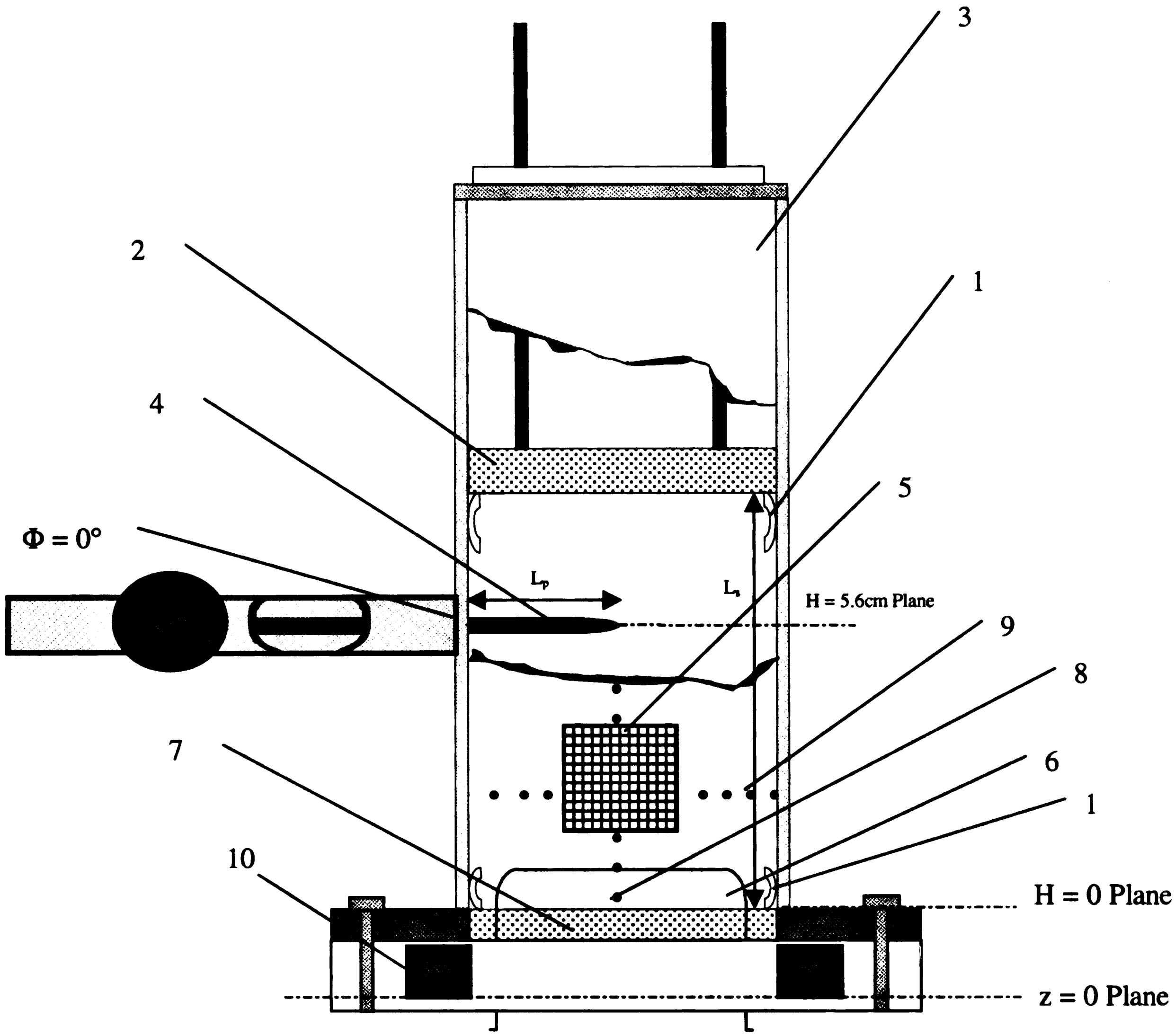

1) Finger stocks
2) Sliding short top plate
3) Brass shell
4) Excitation probe
5) Viewing window
6) Quartz bell jar
7) Bottom end plate
8) Horizontal electric field sampling pinholes
9) Vertical electric field sampling pinholes
10) ECR magnets

Figure 1.6 MPDR 7 - Side Feed (SF) plasma source

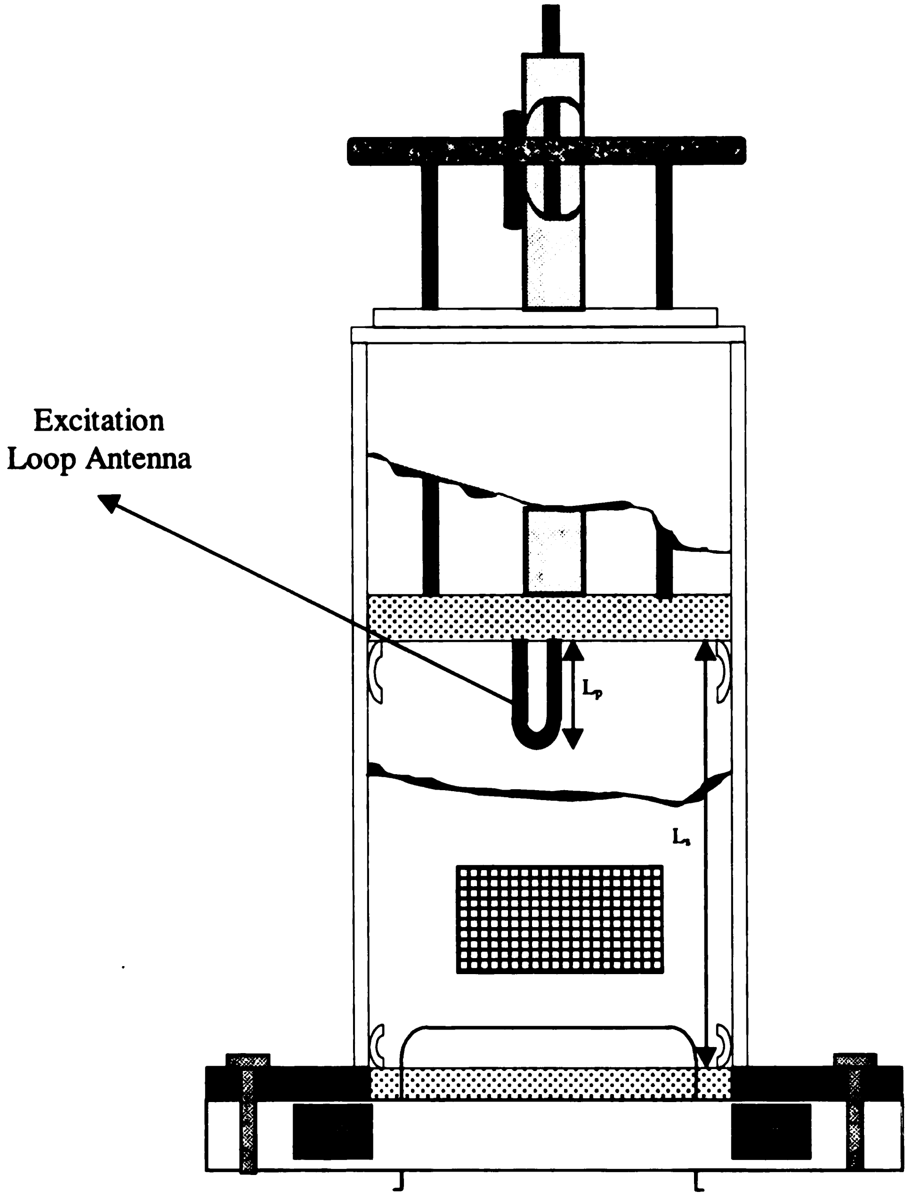

Figure 1.7 MPDR 7- End Feed Loop (EFL) plasma source

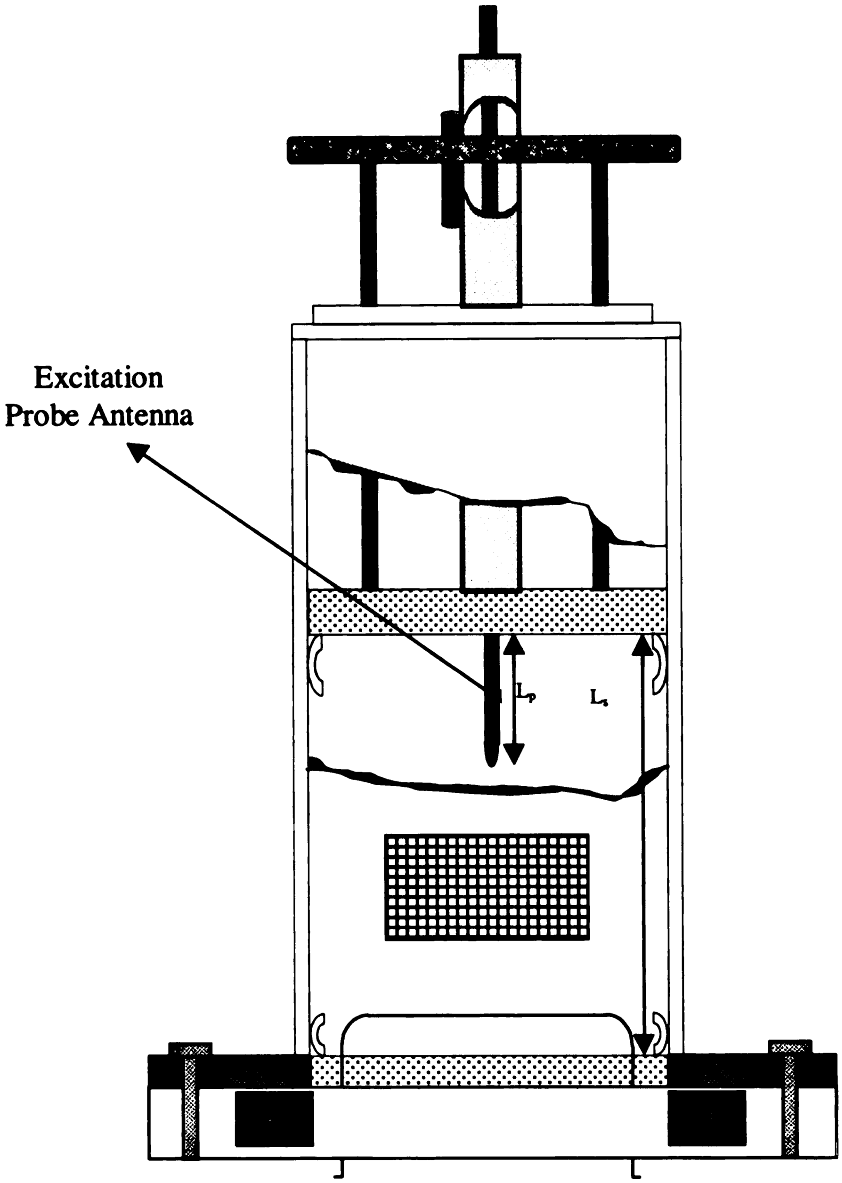

Figure 1.8 MPDR 7- End Feed Probe (EFP) plasma source

1.5 Research objectives

The overall aim of this investigation is 1) to establish the performance of small MPDR plasma sources, 2) to understand the physical phenomenon responsible for the input/output behavior of MPDR plasma sources and then based on this information 3) suggest ways and means to improve the design of existing MPDR plasma reactors. An improved understanding of the physical behavior of MPDR plasma sources will allow selective optimization of associated system variables and figures of merit.

1.5.1 Specific research objective

Even though a large number of MPDR plasma sources differing in geometrical configurations have been already extensively characterized at MSU, there still are a number of poorly understood aspects which directly relate to the operation of these plasma sources. The objective of this research is to investigate the influence of the method of cavity excitation on the performance of low-pressure microwave discharges. Specifically this research evaluates the influence of cavity excitation by experimentally evaluating three different excitation configurations: 1) side feed probe excitation, 2) end feed probe excitation and 3) end feed loop excitation.

1.5.2 Experimental plan

Plasma generation and processing is a very complex and a non-linear process, which is interdependent on a large number of what we call as procedural variables (discussed in Chapters One and Four). A detailed information on these experimental variables can be traced in the reference [14]. It has been very difficult to find the correlation of these variables in terms of their combined and individual influence on reactor's output variables vector (Y). A complex experimental problem solving technique isolates the variables and then investigates their independent control over the system efficiency. This eliminates the influence of other variables on process output. This unique methodology is employed in this thesis investigation by varying the microwave excitation configuration, a reactor geometry variable (U_2), and studying its influence on the reactor's performance. Therefore as described earlier, in this thesis, three MPDR 7 ion and plasma sources, which only differ in the method of excitation, i.e. side feed, end feed loop and probe excitation are evaluated (see Figure 1.9). The influence of excitation geometry on the source performance is investigated by adopting a strategy defined in the following section.

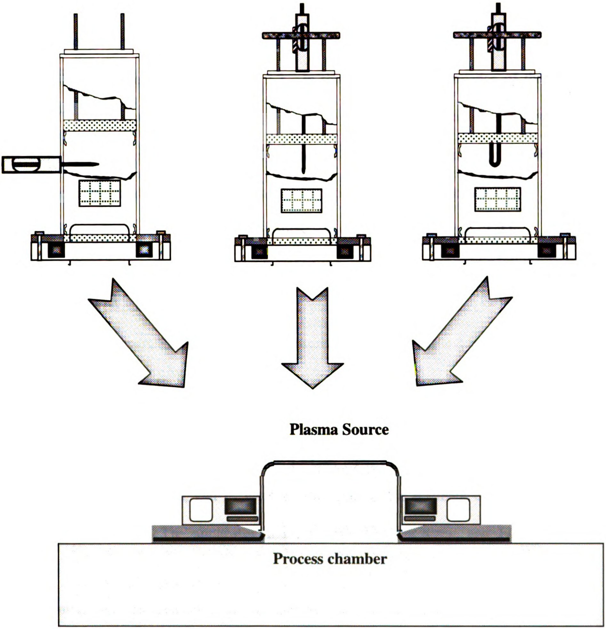

Figure 1.9 Experimental plan

1.5.3 Experimental evaluation procedure

The variables associated with plasma processing machines have earlier been discussed and defined in the Section 1.2.2. In this thesis the performance of the three MPDR 7 plasma sources, shown in Figures 1.6 – 1.8, was evaluated by measuring an exclusive group of internal variables (X) and output variables (Y) against the variations in macroscopic controllable input variables (U_1) and reactor geometry variables (U_2). Figure 1.10 displays, in general, the system variables investigated in this work. Tables 1.2, 1.3 and 1.4 describe, in particular, the variance of independently controlled input variables space (U) for the three MPDR 7 ion and plasma sources. Within the macroscopic controllable input variables space (U_1): 1) absorbed power (P_{abs}) and chamber pressure were varied for all the three configurations, 2) gas flow rate was varied for the side feed excitation only and it was fixed for the end feed sources, 3) operating frequency was kept constant at 2.45GHz, 4) argon gas was used as the input gas for all the experiments, and 5) the tuning parameters L_s and L_p were varied to attain the resonant conditions in the three plasma sources. The applicator and discharge chamber sizes, and ECR magnet configuration were kept fixed within the reactor geometry variables (U_2). Most importantly, three different methods of microwave excitation were employed in order to understand the influence of the method of excitation on the plasma reactor performance.

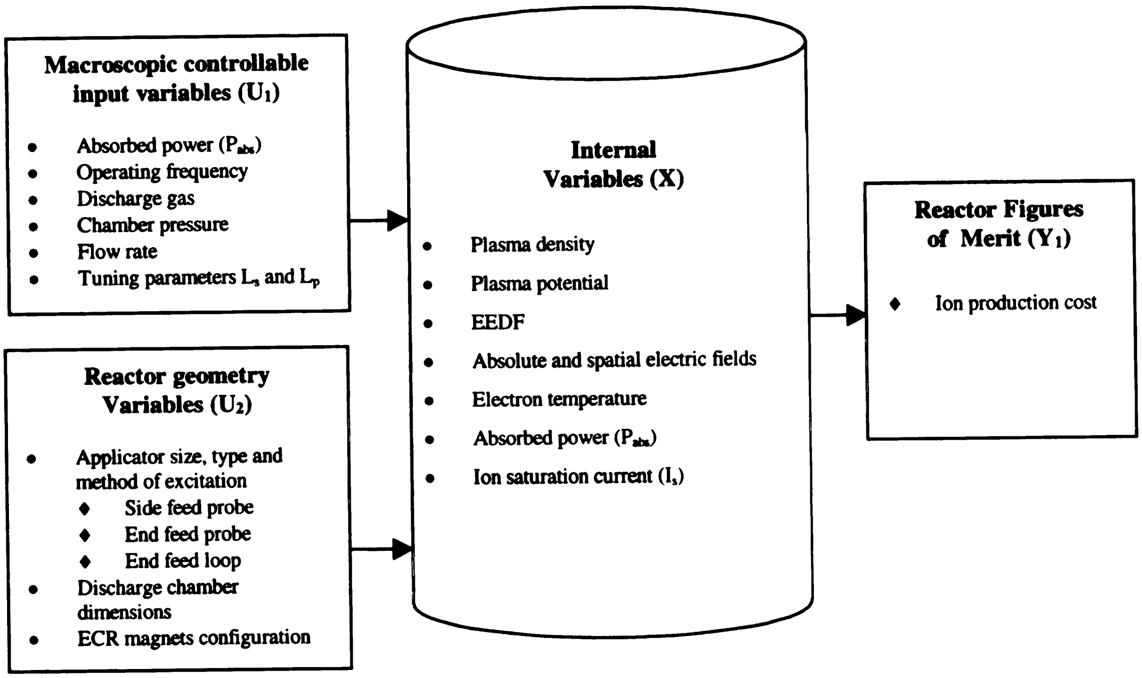

Figure 1.10 Experimental system variables

Input Variables (U)	**Description**	**Experimental Range**
Macroscopic controllable input variables U_1	Absorbed power P_{abs}	50-200 Watt
	Operating frequency	2.45GHz (CW)
	Discharge gas	99.99% Argon
	Chamber pressure	1-8 mTorr
	Flow rate	0.3 – 35sccm
	Cavity short length L_s	13.7 – 8.4cm
	Depth of excitation probe antenna L_p	1.2 – 1.9cm
Fixed reactor geometry variables U_2	Applicator size, type and the method of excitation	8.9cm diameter cylindrical brass cavity with side feed excitation
	Discharge chamber dimensions	Height 5.6cm, radius 3.5cm with a total discharge volume of 215.5cm^3
	ECR magnet configuration	8 Pole 8 Magnets (8P/8M)

Table 1.2 Input variables for MPDR 7 – Side Feed

Input Variables (U)	Description	Experimental Range
Macroscopic controllable input variables U_1	Absorbed power P_{abs}	100-150 Watt
	Operating frequency	2.45GHz (CW)
	Discharge gas	99.99% Argon
	Chamber pressure	1-8 mTorr
	Flow rate	Fixed at 20 sccm
	Cavity short length L_s	3.13 – 10.78cm
	Depth of excitation probe antenna L_p	0.97 – 3.82cm
Fixed reactor geometry variables U_2	Applicator size, type and the method of excitation	9.8cm diameter cylindrical stainless steel cavity with end feed probe excitation
	Discharge chamber dimensions	Height 5.6cm, radius 3.5cm with a total discharge volume of 215.5cm^3
	ECR magnet configuration	8 Pole 8 Magnets (8P/8M)

Table 1.3 Input variables for MPDR 7 – End Feed Probe (EFP)

Input Variables (U)	Description	Experimental Range
Macroscopic controllable input variables U_1	Absorbed power P_{abs}	100-150 Watt
	Operating frequency	2.45GHz (CW)
	Discharge gas	99.99% Argon
	Chamber pressure	1-8 mTorr
	Flow rate	Fixed at 20 sccm
	Cavity short length L_s	4.575 – 8.075cm
	Depth of excitation loop antenna L_p	1.95 – 3.2cm
Fixed reactor geometry variables U_2	Applicator size, type and the method of excitation	9.8cm diameter cylindrical stainless steel cavity with end feed loop excitation
	Discharge chamber dimensions	Height 5.6cm, radius 3.5cm with a total discharge volume of 215.5cm^3
	ECR magnet configuration	8 Pole 8 Magnets (8P/8M)

Table 1.4 Input variables for MPDR 7 – End Feed Loop (EFL)

1.6 Thesis outline

The work in this thesis is divided into five chapters. The Chapter two describes the plasma processing system. The Chapter three reviews experimental techniques employed in this research. Experimental results together with discussions are presented in the Chapter four. In past investigations the global plasma model has been an effective tool to understand and predict a plasma source behavior. Global model equations are described in Chapter four and plasma source performance comparison is drawn for MPDR sources in three different coupling configurations. Chapter five finally concludes this presentation by giving the summary of results and conclusion drawn out of them.

Chapter 2

Experimental systems

2.1 Introduction

As discussed in Chapter 1, three compact Microwave Plasma Disc Reactor (MPDR) ion and plasma sources are evaluated in this work. These sources are almost identical in size but employ three different microwave excitation techniques. Thus these three plasma sources are very useful in understanding the influence of microwave excitation on the plasma reactor performance.

This chapter describes the experimental systems used in this research work. In Section 2.2 microwave power supply, power-monitoring circuit, vacuum and gas flow systems are illustrated. The microwave reactor is described in detail at Section 2.3. This section also describes the design and operation of the three MPDR-7 ion and plasma sources, and the geometry of process and discharge chambers.

2.2 Experimental systems

Even though there are a number of variations in the design of ECR plasma processing machines, an ECR plasma processing system can still be described by a generalized system. Figure 2.1 displays a generic form of a typical plasma-processing machine.

It can be seen from the figure that the experimental system is divided into three major subsystems: 1) power supply and power monitoring circuit, 2) microwave reactor, and 3) vacuum and gas flow system. These subsystems are described in the following sections.

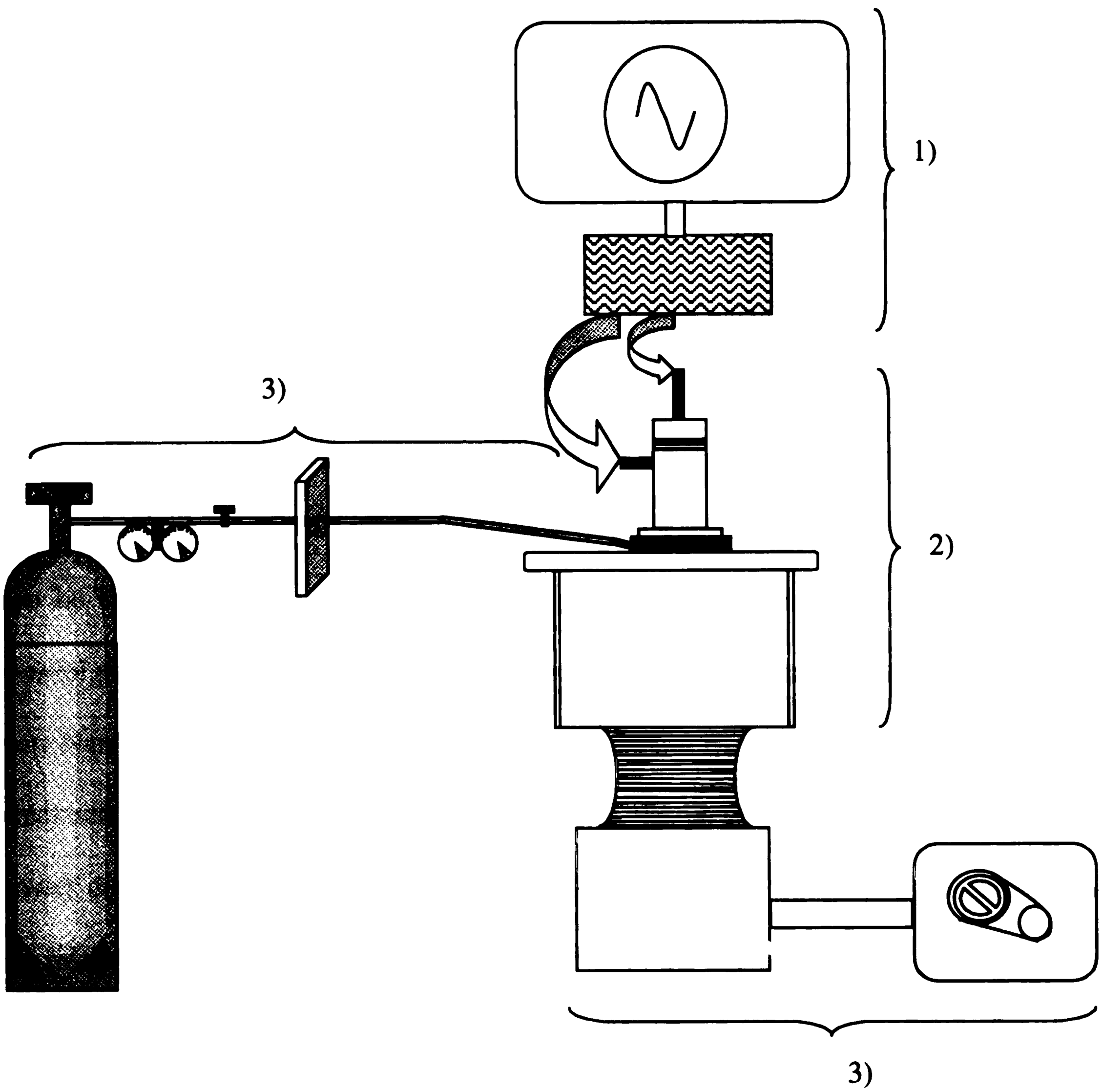

1) Power supply and power monitoring circuit

2) The microwave reactor

3) Vacuum and gas flow system

Figure 2.1 The generic plasma processing machine

2.2.1 Microwave power supply and power monitoring circuit

Figure 2.2 displays the microwave power supply and the power monitoring circuit used in the experiments. As per experimental parameter space (see Table1.2, Chapter one), a variable, 2.45GHz power supply (Micro-Now Inc.'s model 420B1) was used in the experiments. This power supply (1) which is specifically designed for research and industrial applications [16] uses a CW magnetron source and has an output of 50-500 Watt at 2.45 GHz ($\pm$10 MHz) with 50 Ohm output impedance. The desired output power can be obtained by slowly rotating the magnetron current control knob on the front control panel. The microwave power is fed directly through a barrel connector to a three port Narda coaxial circulator (4) which has a maximum power rating of 500 Watt. This unidirectional circulator performs: 1) isolation of the power supply from the reflected power due to sudden variations in the load impedance, and 2) connects power supply to the microwave cavity applicator. Output power from the microwave supply tends to drift whenever there is a change in the plasma load impedance. A user must be mindful to frequently monitor the output power readout and adjust its level to the desired value. Large reflected power might heat up the circulator and this may eventually burn it out. To prevent this from happening, a cooling fan is provided at its top. As an additional precautionary measure, it is advisable to keep the fan running regardless of the amount of input power. Microwave energy is fed into the port 1 which is then coupled to the port 2. This port is connected to a Narda 3003-30 (-30db) directional coupler (8), which then delivers power to the cavity applicator via semi rigid, high power 50 Ohm coaxial cable. A fraction of input power is sampled from the incident wave by directional coupler (8) and is fed into a HP-8481A power sensor (3) which is connected to HP-435A (2) power meter. To prevent any excess power into the power sensor, an attenuator (7) with 21.5db rating is placed in between the directional coupler and the power sensor.

In case of a mismatch, a portion of incident power is reflected back through port 2 to port 3 and is then absorbed via 50 ohm coaxial cable in a Bell 8201, 500 Watt and 50 Ohm oil cooled dummy load (9). Similarly, as described earlier, a fraction of reflected power is sampled via a directional coupler (6), a 19.5db attenuator (5), a power sensor (3) and a power meter (2).

2.2.2 Vacuum and gas flow system

The microwave reactor is initially evacuated from atmospheric pressure to 20mTorr (approximately) with the help of a $33m^3/hr$ mechanical pump. Once the chamber pressure is below 20mTorr, a diffusion pump shares the pumping. This is a NRC - R121 type water- cooled diffusion pump whose fluid charge capacity is 500cc with a rating of 2500 liter/sec and is filled with Krytox oil. Chamber pressure from atmospheric to 100mTorr was measured by a thermocouple pressure gauge. A baratron gauge measured the pressure from 100mTorr to 0.1mTorr, and an extremely sensitive ion gauge recorded pressure in the 1.0 - 0.001 mTorr range. Users should not forget to zero the baratron gauge before carrying out any experiments. Once the reactor is evacuated to a low pressure (in mTorr range), the baratron gauge is zeroed by shutting off the gas flow and pressing the zero touch key for a few seconds on MKS 651 pressure controller.

Through out this research work 99.99% pure argon gas has been used to ignite the plasma discharge. This noble gas discharge is far less complex than the other gases due to latter's intricate transport and collisional phenomenon. Argon gas is supplied to the processing chamber from a pressurized cylindrical gas tank through a 0.25" corrugated flexible steel tubing via MKS 1159 mass flow controller. This is a thermal type flow controller used for high flow applications with range of 0.1sccm to 30slm and has a full-scale accuracy of $\pm$ 1%. A digital four channel MKS - 247C mass flow controller readout is provided with the system. Flow rate set points can be adjusted either from the mass flow panel controls or remotely through the rear panel analogue interface. It also features a front panel selectable gas ratio control mode allowing the user to change (in multi-gas system) the total flow while holding some gases in a fixed ratio. Argon gas from the flow controller is then fed to the steel base plate, which has eight equally, spaced 1/64" diameter gas outlets.

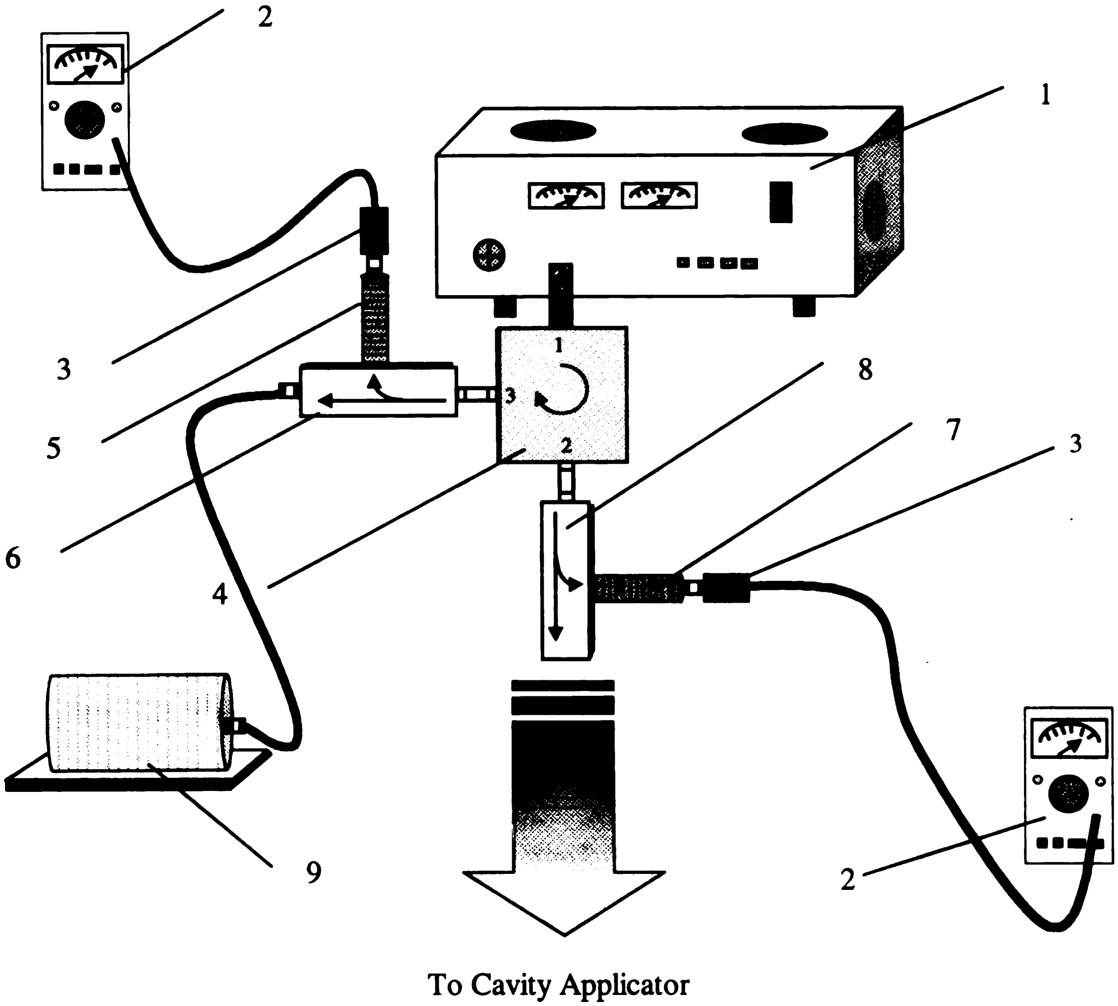

1) Microwave power supply
2) HP-435A power meter
3) HP-8481A power sensor
4) Coaxial circulator
5) 19.5db attenuator
6) 20db directional coupler
7) 21.5db attenuator
8) 30db directional coupler
9) 50 Ohm dummy load

Figure 2.2 Microwave power supply and power monitoring circuit.

2.3 The Microwave Reactor

The microwave reactor is defined by two assemblies: 1) plasma source and 2) process chamber. The excitation geometry, design and critical dimensions of these assemblies are determined by the process application.

2.3.1 The plasma source

The plasma source, as defined earlier in Chapter one, comprises of three sub-assemblies. Figure 2.3 describes, schematically, the application specific plasma sources used in this research work. These sources employing various designs in terms of applicator and discharge chamber sizes, ECR magnet configuration and input gas feed mechanism have been evaluated at MSU.

The stainless steel base plate (1) which sits on the top plate of process chamber (discussed later in Section 2.3.2): 1) hosts the input gas feed channels, and 2) provides a placement platform for the discharge chamber (2). Four 1/16'' studs (3) are also welded to the stainless steel base plate. These studs secure the brass ECR magnet keeper assembly (5) and the cavity applicator (11) to the stainless steel base plate (1). The brass magnet keeper assembly sits on the stainless steel base plate via guide post holes (6). This assembly is comprised of two sub-assemblies: 1) ECR magnets and soft iron magnet keeper ring (5b), and 2) ECR magnet container (5a). The ECR magnet container, which is made up of brass, accommodates air and water cooling systems (7 and 8) for the ECR magnets. The cylindrical ring of ECR magnets and soft iron magnet keeper rests in an annular grove cut in the ECR magnet container. The bottom end plate adapter (9) provides the electrical contact through the finger stock (10), to both physically and electrically connect the side and end feed cavity applicators to the base plate assembly (1) and (5). The plasma source is finally assembled by securing the cavity applicator shell (11) with the stainless steel base plate studs using the thumbscrews.

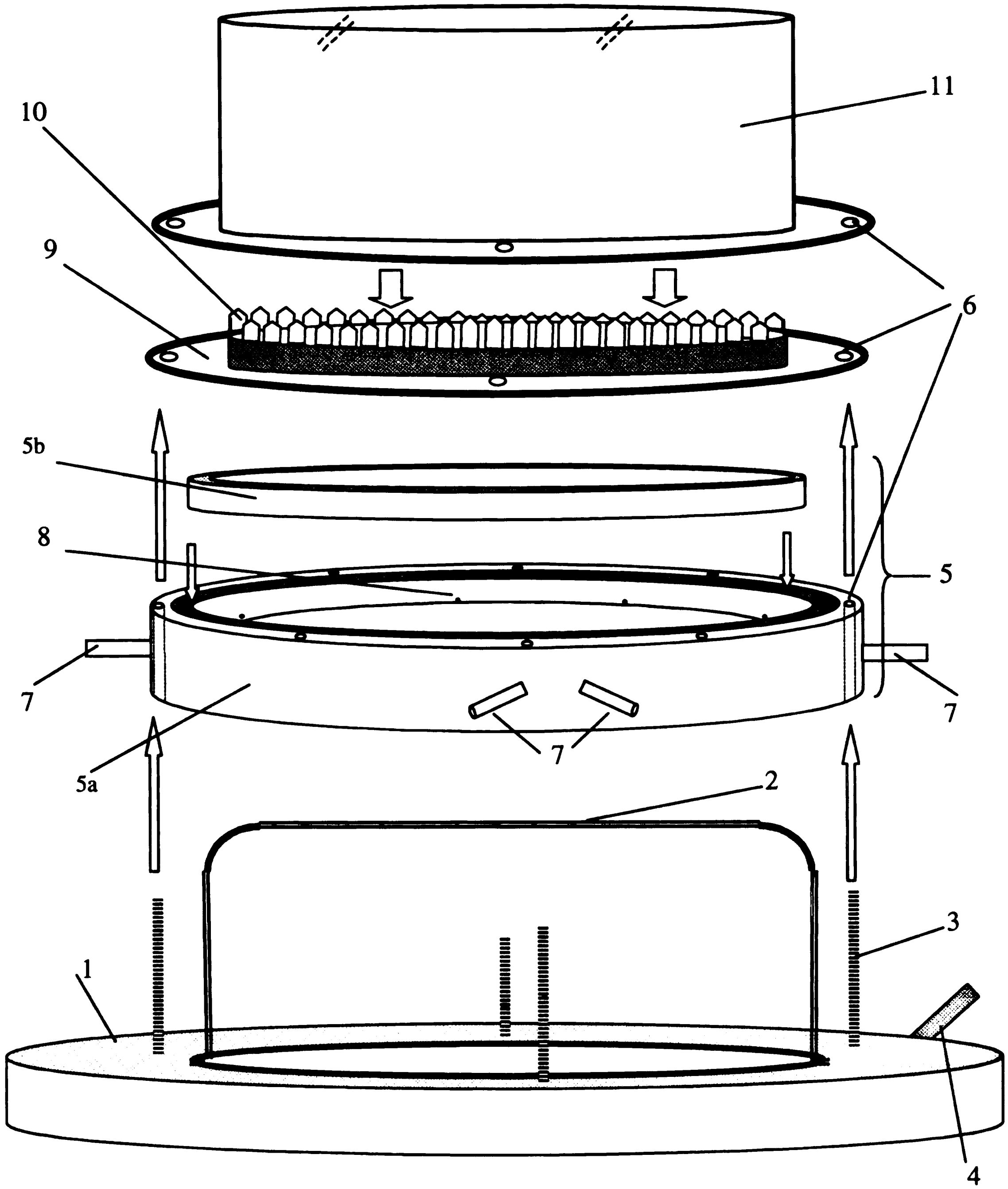

1) Stain less steel base plate
2) Quartz discharge chamber
3) 1/16" studs
4) Operating gas inlet pipe
5) Brass ECR magnet keeper assembly
   5a) ECR magnet container
   5b) ECR magnets and soft iron magnet keeper ring
6) Guide post holes
7) Air and water cooling inlets pipes
8) Air cooling inlet holes
9) Bottom end plate adapter
10) Finger stock
11) The cavity applicator shell

Figure 2.3 MPDR ion and plasma source – Exploded view

2.3.1.1 The cavity applicator and impedance matching network

The ECR ion and plasma sources in different designs employ either external or internal microwave impedance matching networks. The external tuning mechanism usually adopts single or multiple stub tuners, while an internally tuned MPDR has a self-contained impedance matching mechanism. The three MPDR sources investigated in this work are internally tuned. These MPDR ion and plasma sources are described in the following sub-sections.

2.3.1.1.1 MPDR 7- Side Feed (SF)

2.3.1.1.1.1 Brief History:

In sequel to the design improvements in ECR sources at MSU, M. Dahimene was able to extract an 30mA, 1000V, 3.2cm diameter, argon ion beam from a 9.4 cm diameter ECR ion source [17]. Low extraction current and high power costs of 8333 Watt/Beam Ampere were reported for this source. A reason for this was that only 10% of discharge area was utilized for ion beam extraction. Two approaches were available to L. Mahoney to reduce the power cost: 1) utilize the entire bottom of the plasma source to extract a broad ion beam, and 2) reduce the discharge diameter. Since his research was directed towards the design and characterization of compact ion sources [8], Mahoney adopted the latter approach to improve the source efficiency. His objectives were: 1) to determine if a 5cm diameter discharge can be maintained with modest amount of input power (around

200Watt), and 2) to design a compact, simple, reliable, and long life ion source. His first prototype MPDR ion and plasma source was a 17.8cm diameter brass cylindrical cavity with 4.9cm discharge. This source, which is now recognized as the MPDR 5, employed side feed microwave excitation mechanism. Using extraction grids, ion current densities exceeded $10mA/cm^2$ with less than 200Watt of input power. In his second prototype, certain aspects of preliminary design were further improved which made the cavity more reliable, less expensive and simple to operate. A second prototype of MPDR 5 had a reduced cavity diameter of 8.9cm which supported the propagation of a single TE_{111} electromagnetic mode. A modified MPDR 5 ion and plasma source has been used in this thesis research. The modification included the design and fabrication of a new brass bottom end plate that fits the cavity applicator to a 7cm diameter discharge chamber. Figure 2.4 displays the geometrical design of this adapter. In this thesis this source is now referred as MPDR 7 Side Feed (SF). Earlier M. Perrin used this 7cm diameter discharge chamber while evaluating MPDR 7 End Feed Loop (EFL) ion and plasma source [14].

2.3.1.1.1.2 Construction and operation

Referring to the Figure 1.6 (in Chapter one), the microwave applicator consists of a cylindrical brass shell (3), whose inner diameter is 8.9cm and outer diameter is 9.5cm, and a sliding short (2). The height of cavity, L_s, varies from 8.5 - 13.7cm as the sliding short top end plate (2) is adjusted. The lower limit is imposed by the presence of the input microwave excitation antenna, shown at $\Phi = 0°$ in Figure 1.6. The applicator adopts a side feed excitation configuration by coupling microwave energy from its side-wall through a probe antenna (4). This side feed mechanism is affixed at H = 5.6cm, where the reference plane H = 0 is the base of the cavity applicator. The excitation probe's junction with the cavity is taken as a $\Phi = 0°$ reference point for other circumferential orientations along the cylinder. The probe antenna depth, L_p, is made adjustable by using a gearing arrangement that can extend the probe a maximum of 1.9cm into the cavity. This internally tuned cavity matches the microwave power source to the unknown plasma load impedance by adjusting the positions of sliding short top end plate, L_s, and the excitation probe depth, L_p. On its base, the cylindrical cavity applicator sets on the bottom end plate (7) (modified version) and is secured to the brass magnet keeper plate (see (5) in Figure 2.3). Top and bottom end plates consist of finger stock (1) which tightly secures the bottom end plate assembly thereby preventing any microwave leaks. A 2.54cm by 2.36cm viewing window (5) at Φ = 90° is also provided for visual inspection of plasma discharge. The cavity shell is supplied with both vertical and horizontal arrays of electromagnetic field sampling probe holes. Three horizontal sampling probe hole arrays (9) run all along the circumference of the shell and are located at H = 4.6, 8.6 and 10.6cm. Each sampling probe hole is 0.95cm center to center apart and are located in 10° increments all the way upto 360°. Similar set of vertical probe arrays (8) are located at Φ = 180° and 270°. A total of ten sampling holes are provided with each vertical array. The first sampling probe hole is drilled at H = 1.12cm and the holes are separated by 0.95cm. The diameter of these sampling probe holes is 2.9mm. Since this diameter is very small as compared to the signal wavelength (12.25cm), microwave energy does not radiate from these holes.

Once the discharge is ignited, sliding short top plate and the excitation probe are adjusted to minimize the reflected power and tune the cavity to the resonant mode.

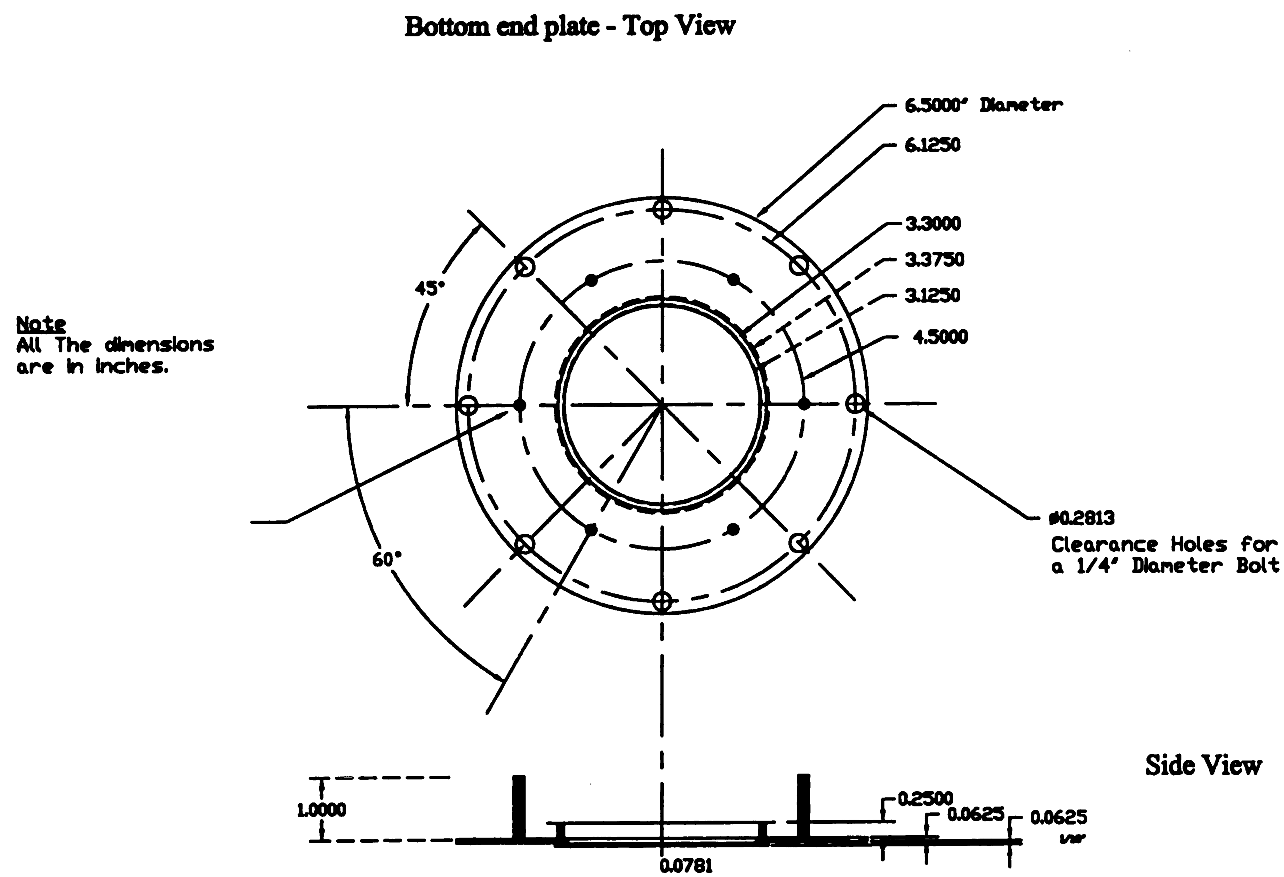

Figure 2.4 Design of bottom end plate adapter

2.3.1.1.2 MPDR 7 End Feed Loop (EFL)

2.3.1.1.2.1 Construction

Refer to Figure 1.7 in Chapter 1. This 9.8cm inner diameter cylindrical stainless steel microwave cavity was designed by L. Mahoney at IBM Watson Research Center and was later donated to MSU. Prior to this work, M. Perrin had evaluated the MPDR 7 - EFL for its electromagnetic coupling behavior [15].

M. Perrin demonstrated that this cavity by adjusting the internal matching network can be tuned to either a TE_{111} or a TM mode. Within the cavity applicator, the TM_{01} mode is excited for a low sliding short length (L_s) while the TE_{111} mode is excited for a large L_s value. The depth of the excitation loop antenna (L_p), which is made up of 0.48cm diameter copper rod, can be varied from 1.5cm to 5.5cm inside the cavity shell. This loop is secured at the sliding short top end plate by using two sets of finger stock. Horizontal and vertical sampling hole arrays are supplied to measure the electric fields in the cavity. This source can be operated over an input power range of 50-300Watt while maintaining a stable and uniform plasma discharge. Reference [15] provides additional detailed information on the cavity dimensions, construction and operation.

2.3.1.1.3 MPDR 7 End Feed Probe (EFP)

2.3.1.1.3.1 Construction

Referrring to Figure 2.5 and Figure 1.8 in Chapter One, the MPDR 7 –EFL applicator can be transformed into end feed probe configuration by replacing the sliding short top end plate assembly with a similar sliding short arrangement hosting an excitation antenna probe (Figure 2.5). This sliding short top end plate assembly was designed by M. Perrin and has been fabricated with technical perfection in Physics Department Workshop at MSU. Thus a 9.8cm stainless cylindrical shell can be operated with either an end feed loop or probe excitation configuration. The excitation probe antenna is made up of a .48cm diameter copper rod which can extend 5.7 cm inside the cavity.

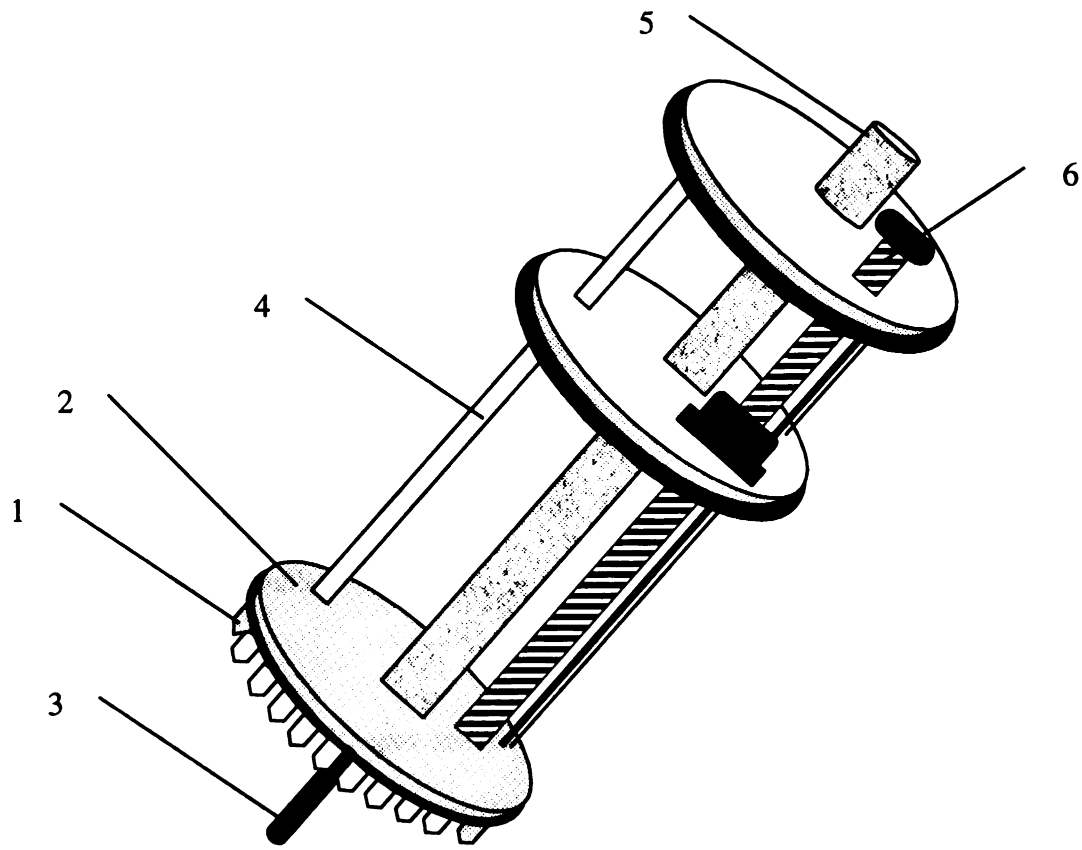

1) Finger stocks
2) Sliding short top plate
3) Excitation probe
4) Support rods
5) Brass probe holder
6) Sliding short top plate adjustment screw

Figure 2.5 End feed probe assembly

2.3.1.2 Quartz discharge chamber

Refer to Figures 2.3 and 2.6. The excitation or the discharge region is bounded by the quartz discharge chamber. A 3.5cm in diameter and 5.6 cm high quartz (2) discharge chamber (bell jar) contains the plasma discharge. This dome shaped bell jar sits on the steel base plate (1) and is sealed by a flat, circular, ring shaped vinyl gasket and a Viton 'O' ring. The plasma after been ignited in the bell jar diffuses out from its opening toward the process chamber (16). The ECR magnet ring (12), that surrounds the bell jar, prevents ion loss to the quartz's walls.

2.3.1.3 Brass ECR magnet keeper assembly

The brass ECR magnet keeper assembly is shown as 5 in Figure 2.3. A more detailed sketch is given in Figure 2.7. The brass ECR magnet keeper assembly (5) which functions: 1) to house eight alternating pole ECR permanent arc magnets (12), and 2) to prevent heating up of magnets by providing air and water-cooling channels (see 7 and 14 in Figures 2.3 and 2.6 respectively). This 3.17cm high, ring shaped brass ECR magnet keeper assembly has a 16.5cm outer diameter and 7.6cm inner diameter as shown in Figure 2.7. This assembly surrounds the 7cm quartz discharge chamber.

The rare-earth magnets employed for electron cyclotron resonance cavity are sensitive to high temperature and thus require protection from heat exposure. This is achieved through air and water cooling of the brass magnet keeper assembly. Compressed air is fed to the magnet keeper through two brass tubes (22) attached to the either sides of the keeper. The air runs across the annular channels within the keeper and is let out to cool off the outer surface of quartz bell jar through eight small pinholes (8) (see Figure 2.3).

Due to the presence of magnetic fields from the ECR magnets, charged particles oscillate around the magnetic field lines at the cyclotron frequency. Once the cyclotron frequency reaches the applied microwave frequency, the phenomenon of electron cyclotron resonance takes place. This results in the maximum transfer of microwave energy to the discharge. For the 2.45 GHz input microwave frequency 875 Gauss of magnetic field is required to produce electron cyclotron resonance. This is governed by the relation:

$$B = m_e \omega / e$$

where B is the magnitude of magnetic field, m_e is the mass of electron, e is the magnitude of charge and ω represents the angular frequency.

As shown in Figure 2.7, eight arc shaped 3.7 x 0.8 x 2cm alternating pole neodymium-iron-boron magnets (12) are contained in the soft iron magnet keeper and they produce an ECR zone (23) lying approximately 1cm from the magnet face. Magnetic field intensity of the ring magnets decreases from maximum at the pole face to zero at the center axis (at r = 0). These magnets are glued together to form a ring around the bell jar. This magnet ring is enclosed in a soft iron magnet keeper (13) that serves to confine the magnetic fields. The soft iron magnet keeper prevents downstream leakage of the magnetic fields into the process chamber.

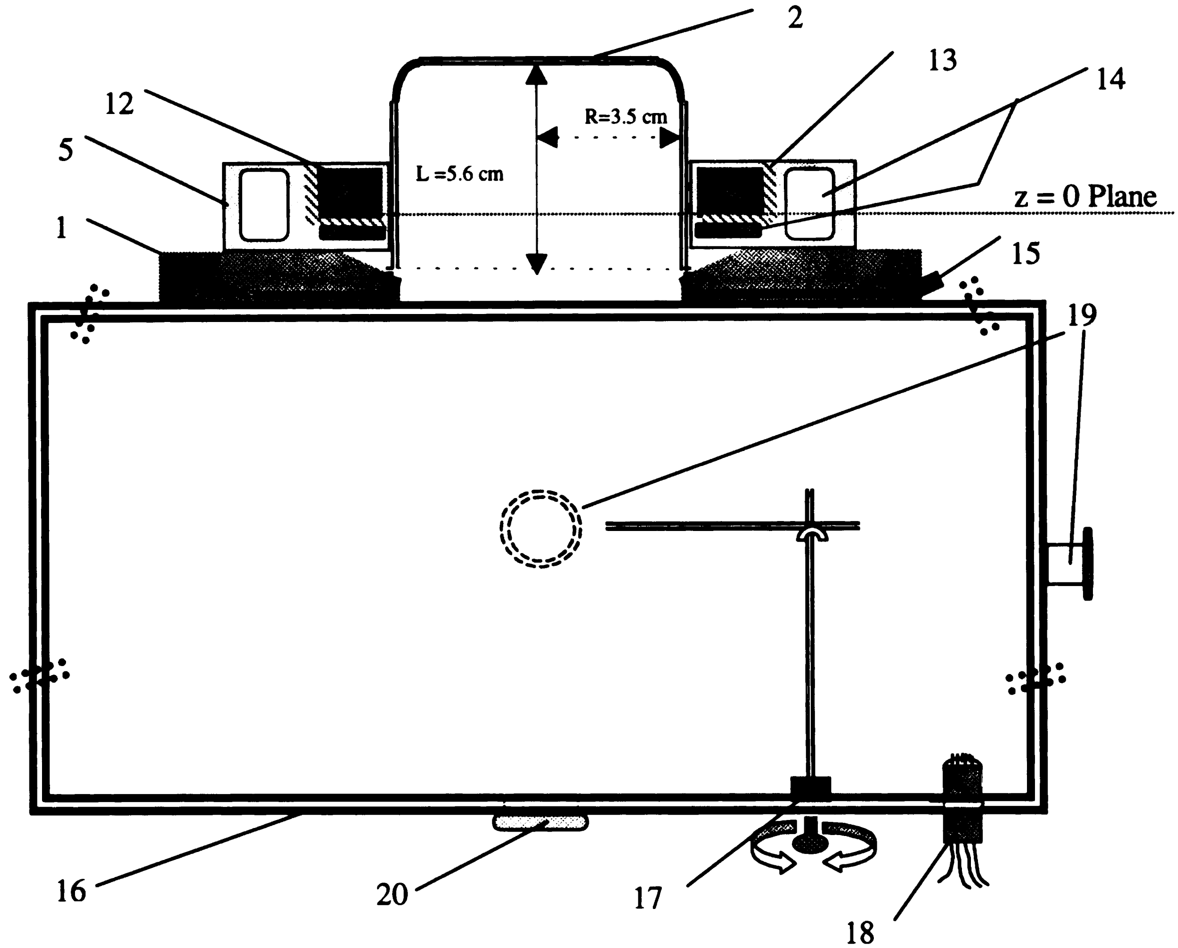

12) 8 Alternating pole ECR arc magnets
13) Soft iron magnet keeper
14) Air and water cooling channels
15) Argon gas flow channel
16) Process chamber
17) Probe holder assembly
18) Vacuum feed through connector
19) Optical windows
20) Viewing port

Figure 2.6 Process and discharge chamber

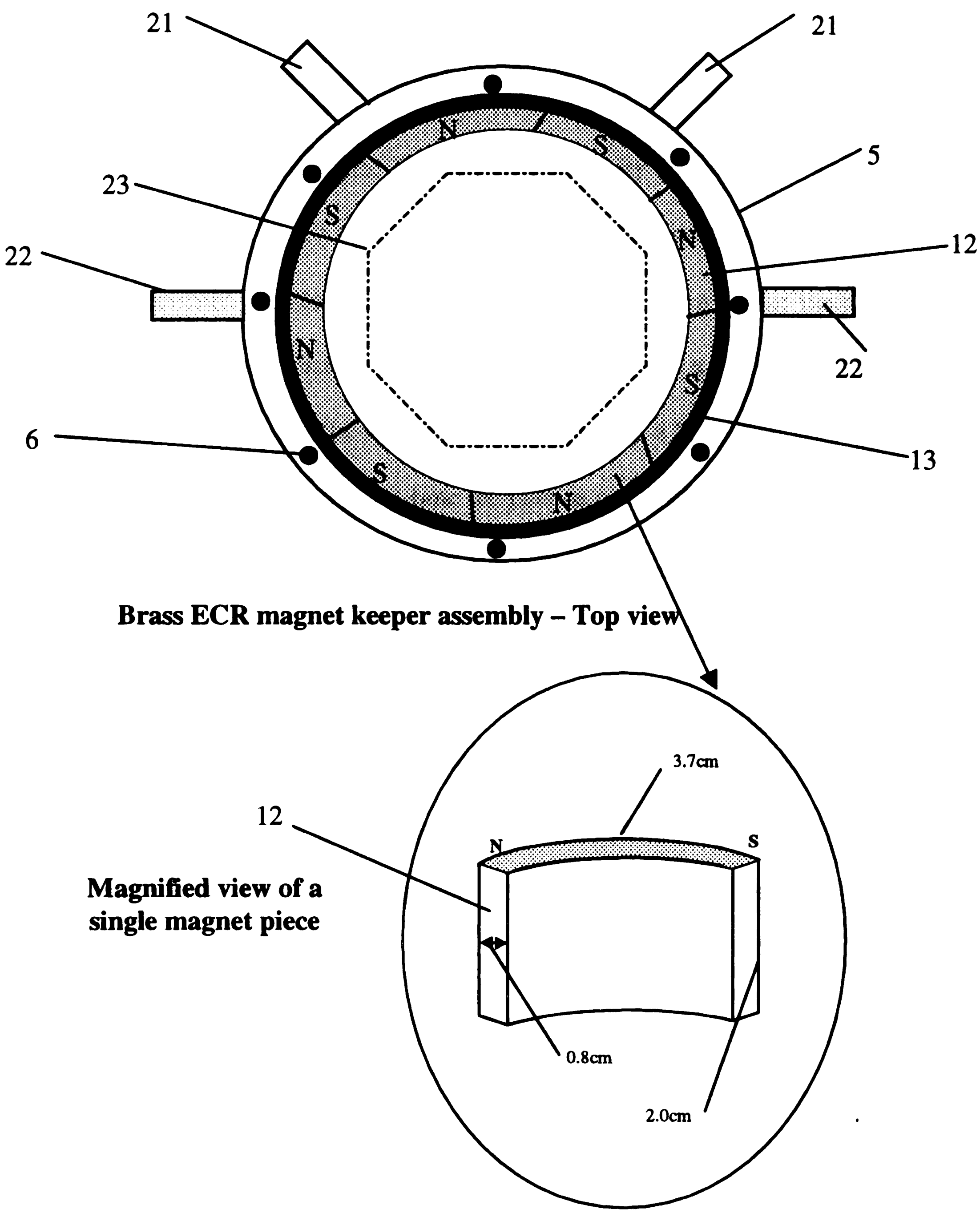

21) Inlet for water-cooling.
22) Inlet for air cooling
23) 875 Gauss ECR zone

Figure 2.7 Brass ECR magnet keeper assembly

2.3.2 Process chamber

As shown in Figure 2.6, the 100 liter capacity processing chamber (16) is a stainless steel cylinder with 1.6cm thick walls. Height and diameter of cylinder are 26 and 41.8cm respectively. The top of the chamber is covered by a 1.7cm thick, and 50.5cm diameter steel plate (top plate). The center of this plate has a 12.32cm diameter annular aperture. The chamber and the top plate are sealed with a 0.66cm thick Viton 'O' ring. This ring needs to be greased every time the plate is removed from chamber using a Dow Corning high vacuum silicone grease. At the annular aperture of chamber top plate sits a stainless steel base plate (1) that houses the input gas inlets. A Viton 'O' ring which rests in a grove cut at the bottom of stainless steel base plate serves to seal the base plate (5) and the chamber top plate. A steel plate with the dimensions similar to the process chamber top plate is placed at the bottom of the vacuum chamber (bottom plate). This plate houses: 1) a vacuum feed through (18), that provides electrical contacts for the plasma diagnostic equipment, 2) a Langmuir probe holder (17), which can be moved in radial direction across the opening face of quartz bell jar (2), and 3) a 6.3cm diameter annular aperture, in its centre, which is used as a viewing port (20). Two optical windows (19) both of them 90° apart and 5.9cm in diameter are located on the process chamber side-walls which can be utilized in the plasma spectroscopic investigations.

Chapter 3

Experimental techniques

3.1 Introduction

One of the basic problem in the plasma physics and the plasma based engineering applications is the determination of plasma parameters. These plasma parameters, for example include electron temperature and electron density, plasma uniformity, energy distribution functions of species etc. The goal is to gain quantitative information about the desired plasma parameters by putting together the available analytical techniques. These plasma diagnostic techniques, for example comprise microwave and X-ray diagnosis, photometry, magnetic and electric field measuring probes, mass spectrometry and spectroscopy etc.

In order to extract useful intelligence, the diagnostic methods should not interfere with the plasma itself which should remain unperturbed. This is the guiding principle in the plasma investigations. Before adopting a certain approach, the experimenter should ascertain that the principle is not violated. The plasma diagnostic techniques used in this research work are: 1) single and double Langmuir probe based investigations, which are described in the Section 3.2, and 2) The impressed electric field measurement technique using E-field probes, which is explained in the Section 3.3.

3.2 Langmuir probes

3.2.1 Introduction

Langmuir and his coworkers first used this probe technique in early 1920's [18] and since then it has become a one of the most useful plasma diagnostic technique. These probes being simple in construction and operation are now being widely used to study laboratory-generated plasmas and space plasma investigations.

In this research, electron density, an estimate of electron temperature and ion saturation current were measured using double Langmuir probes for the MPDR 7 – Side Feed (SF), MPDR 7 – End Feed Loop (EFL) and MPDR 7 – End Feed Probe (EFP) ion and plasma sources. Using the single Langmuir probes, the electron energy distribution functions (EEDF) including Maxwellian and Druyvesteyn distribution functions, plasma potential and electron temperature were recorded for the MPDR 7 – Side Feed (SF) plasma source. These measurements were made under different input conditions.

3.2.2 Double Langmuir probes

3.2.2.1 Probe design

Figure 3.1 displays the design of the double Langmuir probe used in this research work. These probes were fabricated in the glass working shop of the chemistry department at MSU.

The probe collecting material should obviate: 1) chemical reactions with the plasma, 2) sputtering, 3) heating up and 4) secondary emission caused by the impact ionization [19]. Tungsten fulfills the above criterion and is widely used in the probe construction material. The double Langmuir probe arrangement comprises of two tungsten rods (1), 0.094cm in diameter, which are sealed inside a glass tube (2). A portion of the rods, which is 0.56cm in length, is exposed to the plasma from one end of the glass tube. Within the tube, the other end of the tungsten rod is connected to the copper connecting wires (4). These copper connectors are then crimped (5) to the electrical wires (6) which make an electrical contact with the external measuring circuit via vacuum feed through (18). The glass tube, in order to electrically isolate the electrodes from the highly reactive plasma species, is sealed at its base using a shrink-wrap. In addition, this shrink-wrap mechanically secures the floating structure at the base of the glass tube. Within the glass tube, the tungsten electrodes are provided additional isolation by enclosing them in the glass capillary tube (3). Extreme care should be taken once the tungsten rods are being sealed in the glass tube. Unequal exposure areas of the electrodes give off-centered I-V characteristic curves causing incorrect interpretation of plasma parameters.

Maintaining a minimum tolerable spacing between the two electrodes is yet another important consideration in the probe design. This spacing is primarily determined by calculating the electron Debye length in the discharge. A detailed treatment on the subject is given in the reference [19]. Electron Debye length is given by the relation:

$$\lambda_D = 69\ (T_e/n_e)^{1/2},$$

where T_e and n_e are the electron temperature in degree Kelvin and electron density per m^3 respectively. For an argon gas discharge, assuming electron temperature and electron density to be 6eV and $1 \times 10^{11}/\ cm^3$ respectively, the Debye length is 50μm. The sheaths surrounding the two electrodes will overlap if the electrode spacing is less than three or four Debye lengths. As a rule of thumb, for any plasma diagnostic setup, the adjacent probes should be kept four Debye lengths apart to avoid any false readings. These electrodes, in our case, are separated by a distance of 0.22cm and thus fulfill the criterion of being several Debye lengths away.

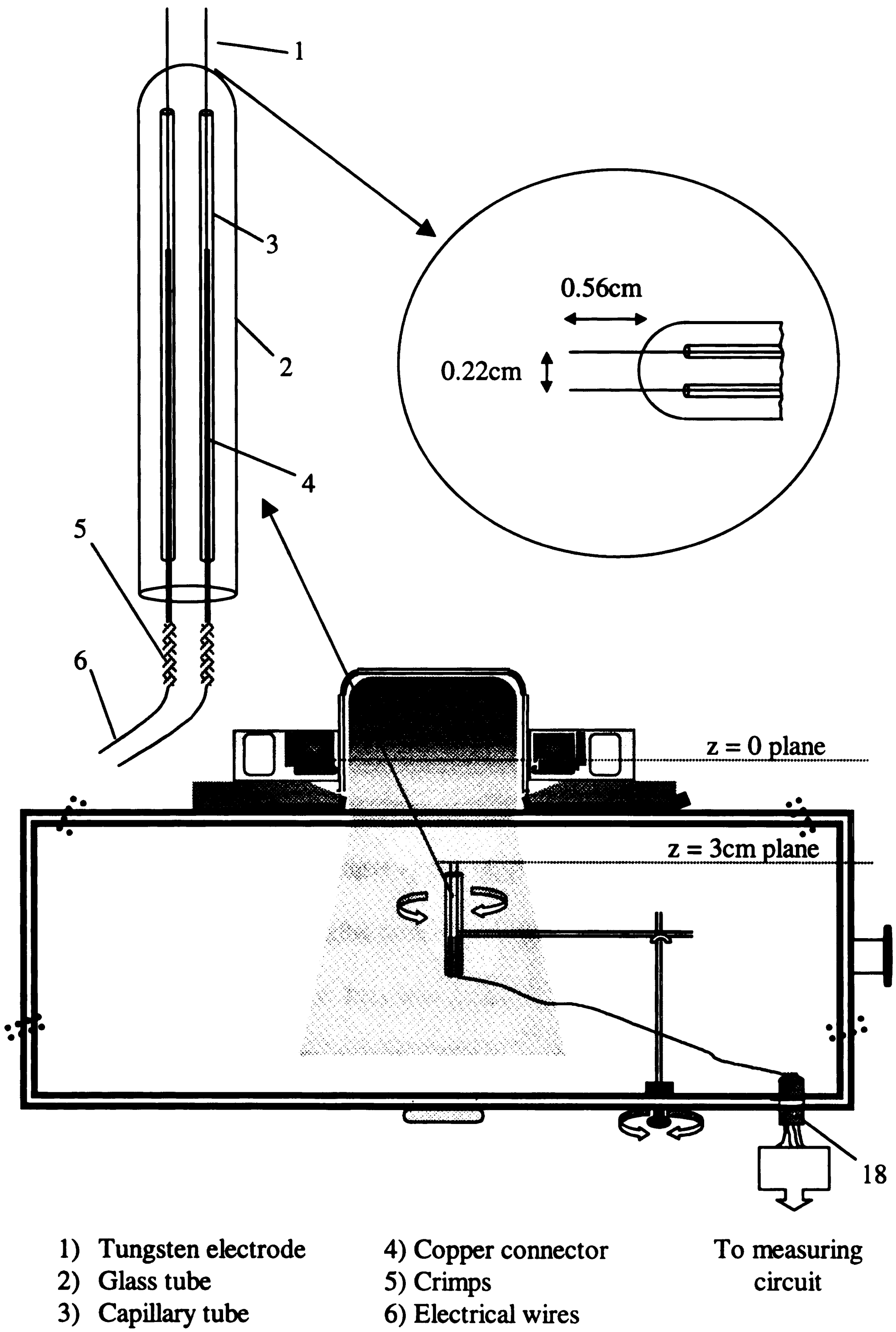

Figure 3.1 Double Langmuir probe experimental setup

3.2.2.2 Principle of operation

The double Langmuir probe technique was first used by E. Johnson and L. Malter [20] in 1949. This technique employs a very simple method and permits the investigation of those plasma's where a reference grounded electrode is missing. The Langmuir probe electrodes are connected across a variable voltage supply and current through them is measured as a function of applied voltage. Figure 3.2 shows the measuring circuit diagram. The d.c. bias across the two probe electrodes (1) was varied from -50 to +50 Volt using a programmable HP 6634A d.c. power supply (4). The output from the variable voltage source can be obtained either locally from the front panel or remotely over the HP IB (which is interfaced with a PC). Voltage difference (V_d) across the two probes is taken as:

$$V_d = V_{p1} - V_{p2},$$

where V_{p1} and V_{p2} are the voltages appearing at the probes 1 and 2. The probe current was recorded on a HP 3478A digital multi-meter that can also be programmed remotely over the HP IB. As the probe d.c. bias was varied from -50 to +50 Volt (starting at –50 Volt and incrementing in 1Volt steps through to +50 Volt), the average probe current was sampled 20 times and the reading was recorded in the computer. This was executed by using a computer program written in Q-Basic. A typical I-V trace is shown in Figure 3.3, detailed explanation of this characteristic curve can be found in the reference [14].

Using the Kirchoff's current law, which states that the current flowing into a node point equals the current flowing out of it, we get:

$$i_{i1} - i_{e1} = i_{e2} - i_{i2} = I_p \qquad (3.1)$$

Where the subscripts "i" and "e" represents ion and electron currents collected by the probes 1 and 2, and I_p is the total probe current. Assuming the Maxwellian distribution, the current collected by both the probes is given by:

$$i_{e1} = I_{eo1} \exp(-eV_{p1} / k_b T_e) \qquad (3.2)$$

and

$$i_{e2} = I_{eo2} \exp(-eV_{p2} / k_b T_e) \qquad (3.3)$$

Where I_{eo1} and I_{eo2} are the electron currents once voltages across both the probes are zero i.e. V_{probe1} and $V_{probe2} = 0$.

By dividing the equation (3.2) with equation (3.3) we get:

$$i_{e1} / i_{e2} = I_{eo1} / I_{eo2} \exp-\{(V_{p2} - V_{p1}) e / k_b T_e\} \qquad (3.4)$$

or

$$i_{e1} / i_{e2} = I_{eo1} / I_{eo2} \exp (-eV_d / k_b T_e) \qquad (3.5)$$

The equation (3.1) $\Rightarrow$

$$i_{e1} / i_{e2} = I_p / i_{e2} - 1$$

Using the equation (3.5) we get:-

$$I_p / i_{e2} - 1 = I_{eo1} / I_{eo2} \exp (-eV_d / k_b T_e) \qquad (3.6)$$

By taking natural logarithm of equation (3.6) we have:-

$$\ln (I_p / i_{e2} - 1) = \ln (I_{eo1} / I_{eo2}) - eV_d / k_b T_e \qquad (3.7)$$

The electron temperature, T_e, can be obtained from the equation (3.7) which is proportional to the slope of $\ln (I_p / i_{e2} - 1)$ vs. V_d

From Bohm sheath criterion [21], ion saturation current is given by:

$$I_i = 0.606\, A_p e\, n_i\, (kT_e/M_i)^{1/2},$$

where e is the electron charge in coulombs, n_i is the ion density in cm^{-3}, M_i is the mass of the argon ion = 40 x mass of proton = 40 x 1.67×10^{-27} kg. Ap is the probe area and is given by:-

$$A_p = 2\pi r \;\; (\text{probe height} + \pi r^2),$$

where the probe height, in our case, is 0.56cm with a radius of 0.047cm giving a total probe area of 0.1723cm^2. Finally the ion current collected by the two probes was averaged to give the ion saturation current (I_i).

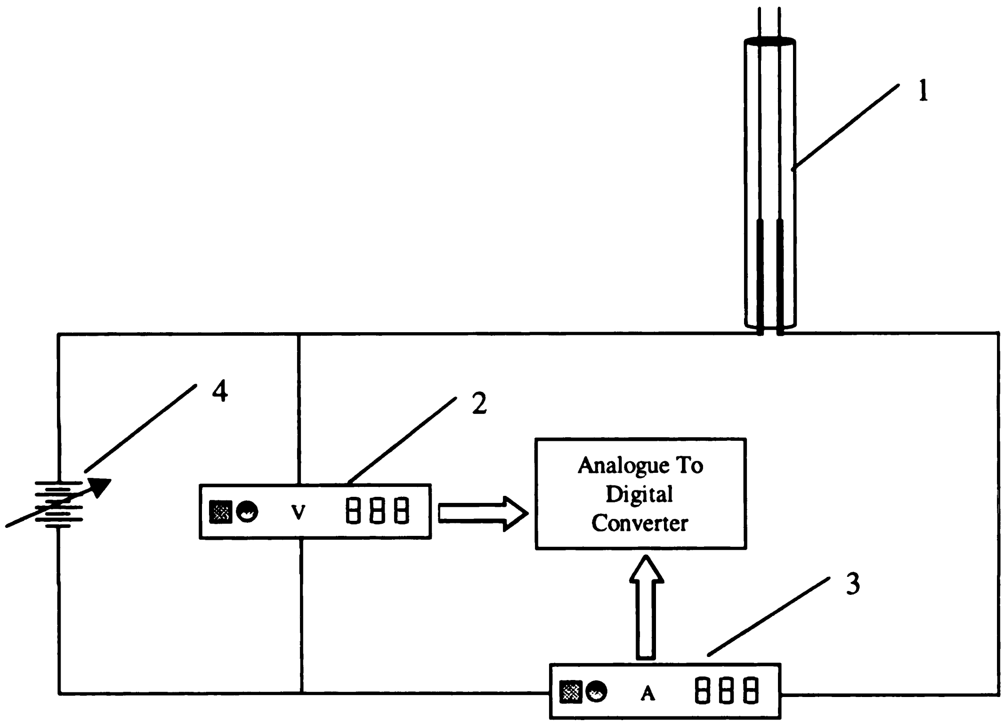

1) Double Langmuir probe

2) HP 3478A Digital voltmeter

3) HP 3478A Digital ammeter

4) HP 6634A d.c. power supply

Figure 3.2 Schematic of double Langmuir probe measuring circuit

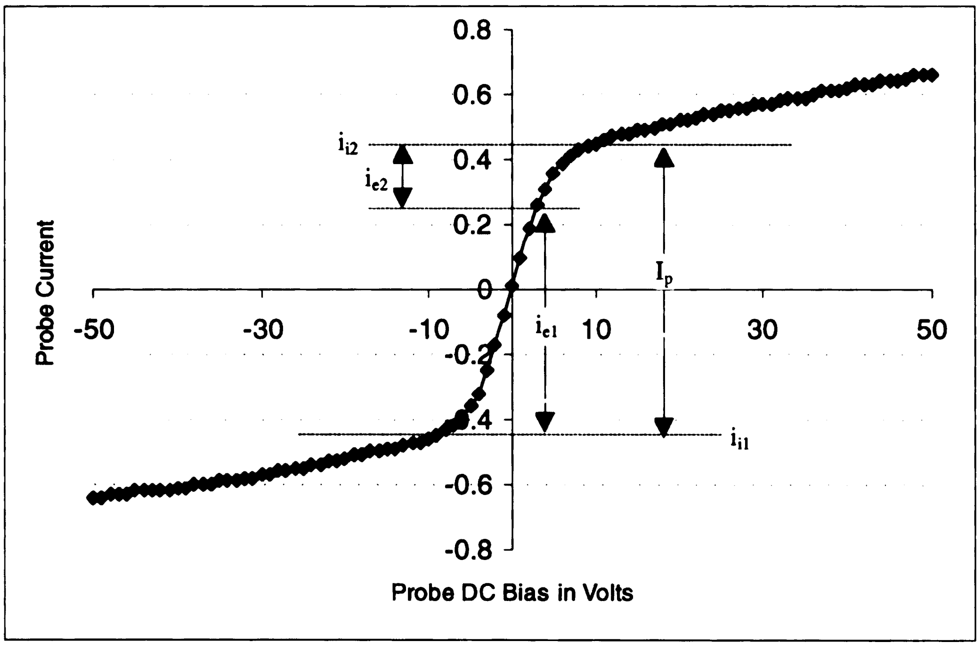

Figure 3.3 A typical double Langmuir probe I –V characteristic curve

Incident power 150Watt
Chamber pressure 2mTorr

Reflected power 2Watt
Flow rate 20sccm

3.2.3 Single Langmuir probe

3.2.3.1 Probe design

The probe design is similar to that of a double probe arrangement and the only difference being the use of a single electrode. The length of probe exposed to plasma in this case was 0.56cm with a diameter of 0.051cm.

3.2.3.2 Principle of operation

Druyvesteyn [22] in 1930 reported that the electron energy distribution function (EEDF), f(E), is directly proportional to the second derivative of the Langmuir probe I-V characteristic curve, i.e.

$$f(E) = (V_s - V)^{1/2}\, d^2I_e / dV^2$$

where V_s is the plasma potential, V is the voltage applied to the probe and I_e is the current drawn by the probe. It should be noted that the above relation is not restricted to the Maxwellian distribution of charges.

Normalizing this distribution function to unity we get:-

$$\int_0^\infty f(E)dE = 1$$

Once electron energy distribution function f(E) is known, average electron energies can be determined by:-

$$< E >= \int_0^{\infty} E \ f(E)dE = 1$$

The second derivative of the probe current, d^2I_e / dV^2, can be determined by superimposing a small modulating voltage on the single Langmuir probe and then measuring the second harmonic of the probe current.

The circuit diagram for the single probe diagnostic set up is shown in Figure 3.4. The amplitude of 1 kHz applied a.c. signal obtained from a HP 651B test oscillator is kept at 0.35Volts rms which is then superimposed on the d.c. voltage. A 128A EG&E amplifier locks on twice the frequency of the sine wave since the second derivative d^2I_e / dV^2 is proportional to the amplitude of the current with a frequency 2ω. The variable HP 6634A d.c. voltage supply was used to vary the bias from -20 to 50Volt.

The probe current is represented by the relation:-

$$I = I(V + v\sin\omega t)$$

This shows that the current collected by probe is a function of both applied d.c. and a.c. voltages. Where V is the d.c. input and v is the amplitude of a.c. signal with a frequency ω.

Using Taylor series expansion we have:-

$$I = I(V) + v \sin\omega t \, dI / dV + \{(v \sin\omega t)^2 / 2! \} d^2I / dV^2 + \{(v \sin\omega t)^3 / 3! \} d^3I / dV^3$$

$$+ \{(v \sin\omega t)^4 / 4! \} d^4I / dV^4 + \{(v \sin\omega t)^5 / 5! \} d^5I / dV^5 + \{(v \sin\omega t)^6 / 6! \} d^6I / dV^6 + \text{-----------}$$

Simplifying the above relation

$$I = I(V) + v \sin\omega t \, dI / dV + v^2/2\{(1- \cos 2\omega t) / 2 \} d^2I / dV^2$$

$$+ v^3/6\{(3/4 \sin\omega t - \sin 3\omega t/4)\} d^3I / dV^3 + \text{-----------}$$

after rearranging

$$I = I(V) + v \sin\omega t \, dI / dV + (v^2/4 - v^2/4 \cos 2\omega t) \, d^2I / dV^2$$

$$+ (v^3/8 \sin\omega t - v^3/24 \sin 3\omega t) \, d^3I / dV^3 + \text{-----------}$$

and finally we get:-

$$I = I(V) + (v^2/4 \, d^2I / dV^2 + \text{-----}) + (v \, dI / dV + v^3/8 \, d^3I / dV^3 + \text{----}) \sin\omega t$$

$$+ (v^2/4 \, d^2I / dV^2 + \text{----})(-\cos 2\omega t) + (v^3/24 \, d^3I / dV^3 + \text{------})(-\sin 3\omega t) + \text{-------}$$

As the amplitude of the applied a.c. signal is kept small we can neglect higher order terms in the above equation.

Unless otherwise stated, the probe was positioned vertically and its electrode tip was located at z = 3cm plane, see Figure 3.1. Over the years, the process chamber of the plasma processing machine used in these experiments became contaminated with a thin insulating layer. This insulating film might have formed due to the suction of diffusion pump oil in the process chamber under the low-pressure conditions. Consequently the chamber walls turned out to be a bad ground. This uncertainty was overcome by using the processing chamber top plate, which is in the close proximity of the plasma discharge as a reference ground potential. Figure 3.5 displays a typical single Langmuir probe I-V characteristic curve. It is noted that the saturation current appears to be missing. This may be attributed to a large current drawn by the probe which disturbs the discharge uniformity [23]. Figure 3.6 shows a d^2I_e / dV^2 plot, here the maximum value of d^2I_e / dV^2 corresponds to the plasma potential.

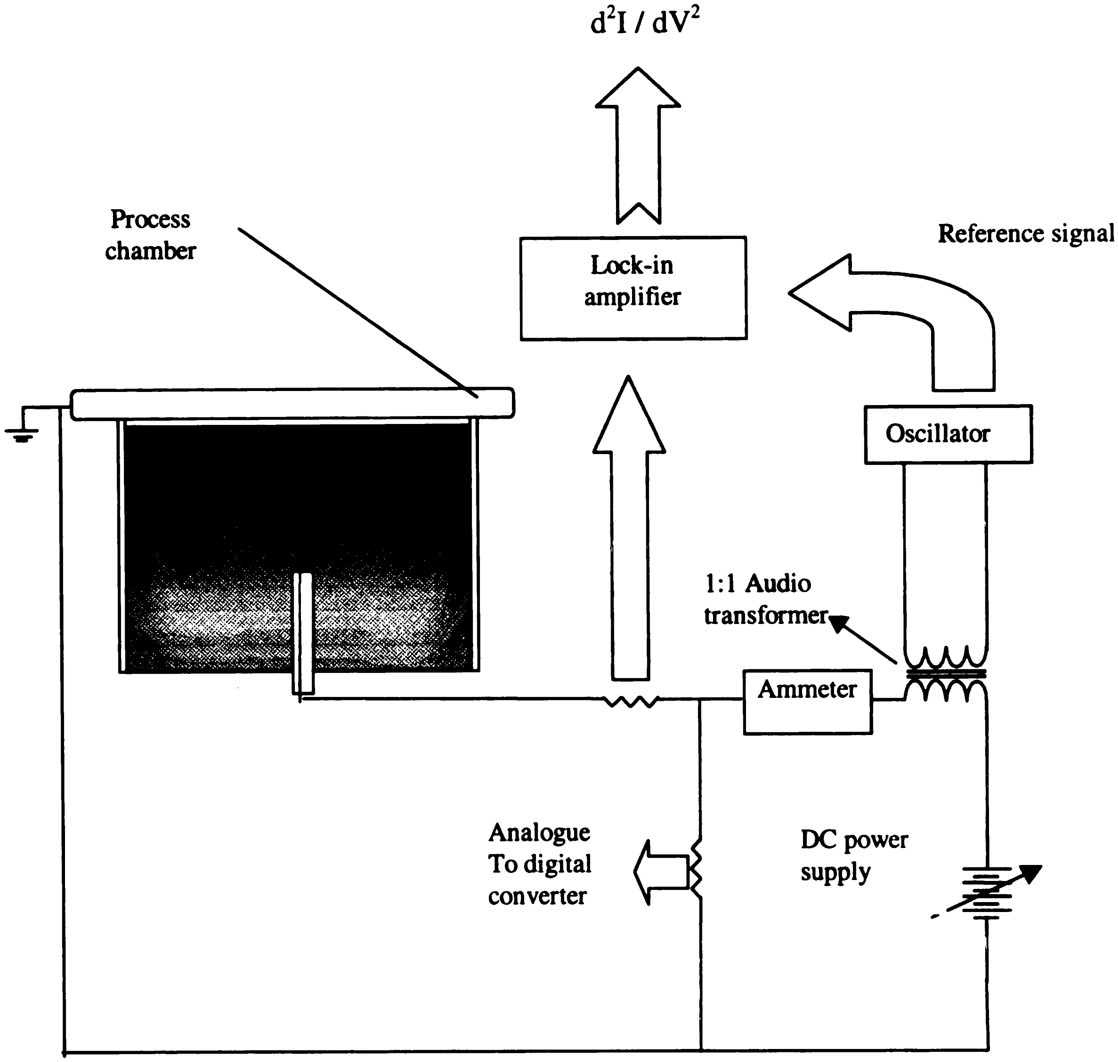

Figure 3.4 Schematic circuit diagram of single Langmuir probe measurement technique

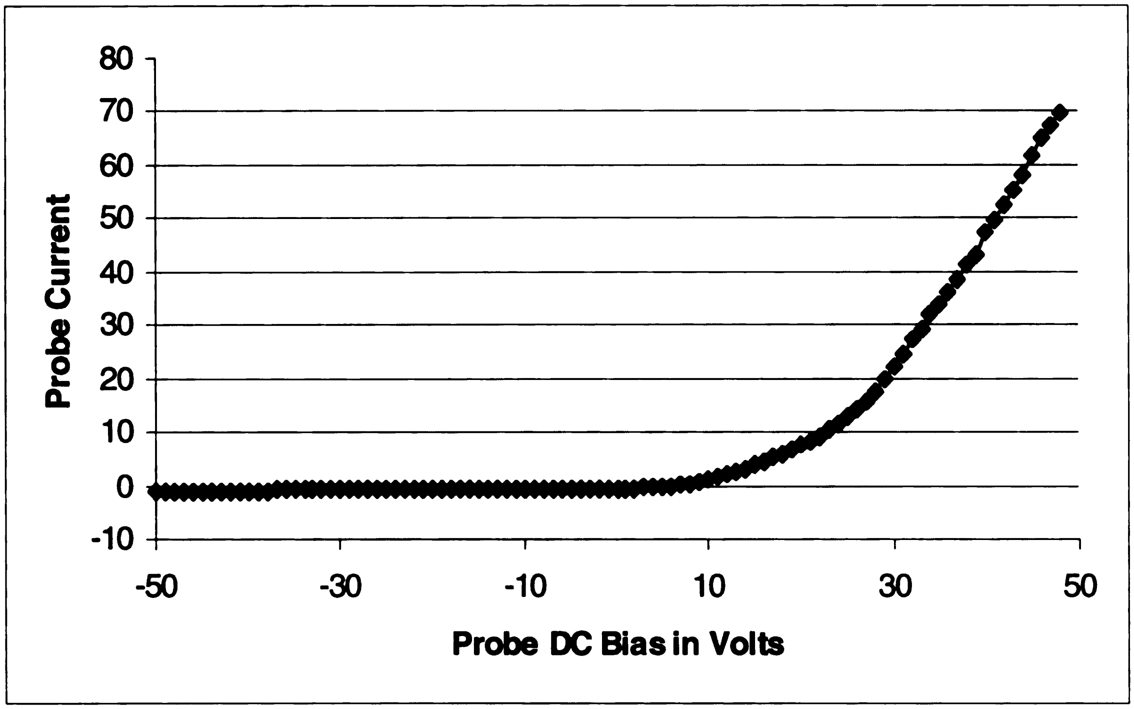

Figure 3.5 A typical single Langmuir probe I –V curve

Incident power 150Watt
Reflected power 2Watt
Chamber pressure 2mTorr
Flow rate 20sccm

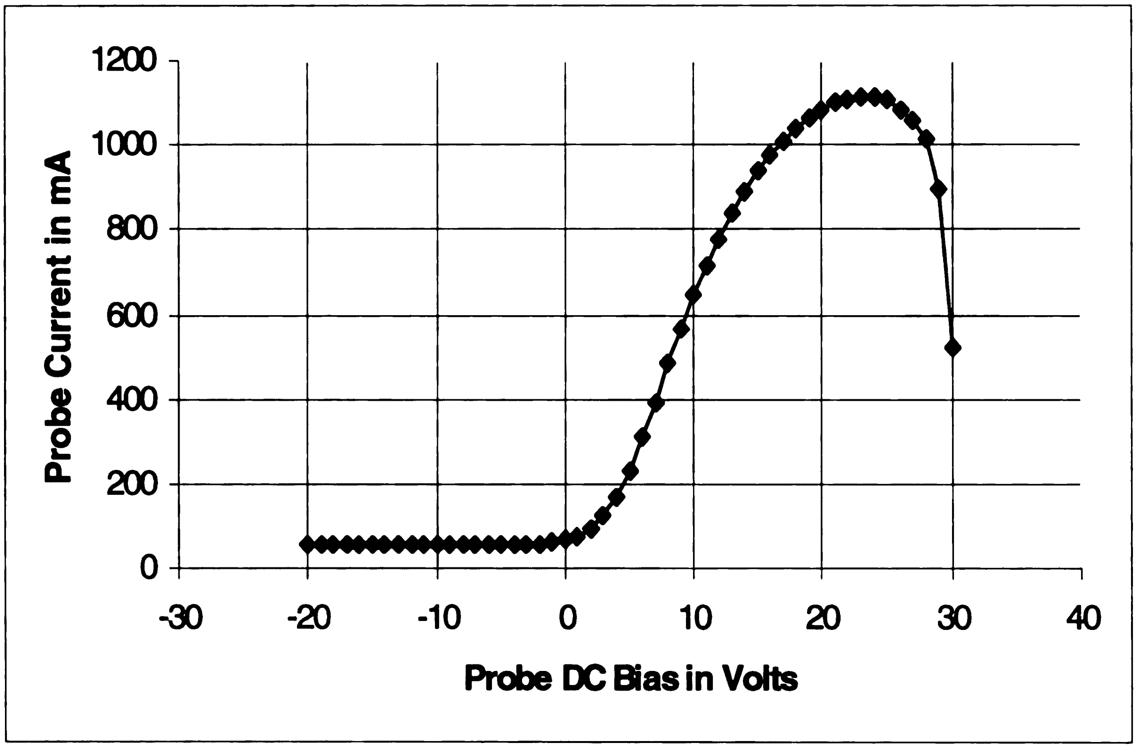

Figure 3.6 A typical single Langmuir probe second derivative curve

Incident power 150Watt
Reflected power 2Watt
Chamber pressure 2mTorr
Flow rate 20sccm

3.3 Electric field measurements

3.3.1 Introduction

Measurement of electric fields inside the microwave cavity applicator is an important aspect once the ion and plasma sources are characterized. Determination of the fields inside a plasma-loaded cavity explains certain significant parameters such as microwave coupling efficiency, and identification and verification of the propagating electromagnetic modes. These measurements were performed only for the MPDR 7 - SF ion and plasma source.

The critical dimensions of the side feed cavity applicator makes it possible to support the propagation of a single electromagnetic mode, which has been identified by Mahoney [9] as the TE_{111} mode. The impressed electric field measurement technique employed here is similar to the one used by the earlier researchers at MSU. The normal component of the electric field, which is incident on the cavity walls, is measured with a coaxial probe commonly known as the E-field probe. The construction and the principle of operation for these probes is described in the following sub-sections.

3.3.2 E – field probe design

Figure 3.7 displays the E-field probe design and the experimental set-up. A semi-rigid copper coaxial conductor (1) was used in the probe fabrication. The diameters of the outer (2) and inner conductors (3) were 0.216cm and 0.0254cm respectively. Three probes were fabricated, each using a 4cm length of the copper coaxial conductor (1). The coaxial conductor was soldered to a SMA connector (5) on one end, and its other end was kept exposed. The E-field probes made for the experiments performed in this research work are named as flush, 0.5mm and 1mm probes. These names reflect the depth of the center conductor, once the field probe is inserted in the cavity applicator (9) through the E- field sampling holes (10 and 11), with respect to the applicator's inner wall. For example, the inner conductor in the flush probe has a zero extension in the cavity whereas 0.5mm probe extends 0.5mm. In order to obtain the desired length of the inner conductor during the fabrication process, the exposed end was very carefully sliced to avoid any burrs and rough edges around the rim. The limited extension of the center conductor within the cavity and its diameter itself evades any chances of perturbing the fields. During the course of experimentation the sampled power never exceeded 0.006% of the input power thus satisfying the need of maintaining unperturbed fields. A brass collar (6) is attached to the probe which: 1) helps inserting the probe in the sampling holes and 2) maintains the desired extension of center conductor in the cavity. The outer conductor (2), when inserted inside the sampling hole, provides the electrical contact with the cavity walls. The sampling pinholes often get oxidized thereby deteriorating the electrical contact. It is therefore advisable to scrub them, ideally by a wire brush. The E-field probe is connected to a HP 8481A thermistor (7) whose maximum power rating is 300mWatts. Finally the power is sampled using a HP 435A power meter (8). The microwave cavity applicator tends to heat up by absorbing the incident microwave power. This factor would result in erroneous readings if the power sensor, which is temperature sensitive, is used in the close proximity of the cavity applicator. The user should therefore keep the thermistor at a distance to prevent any measurement errors.

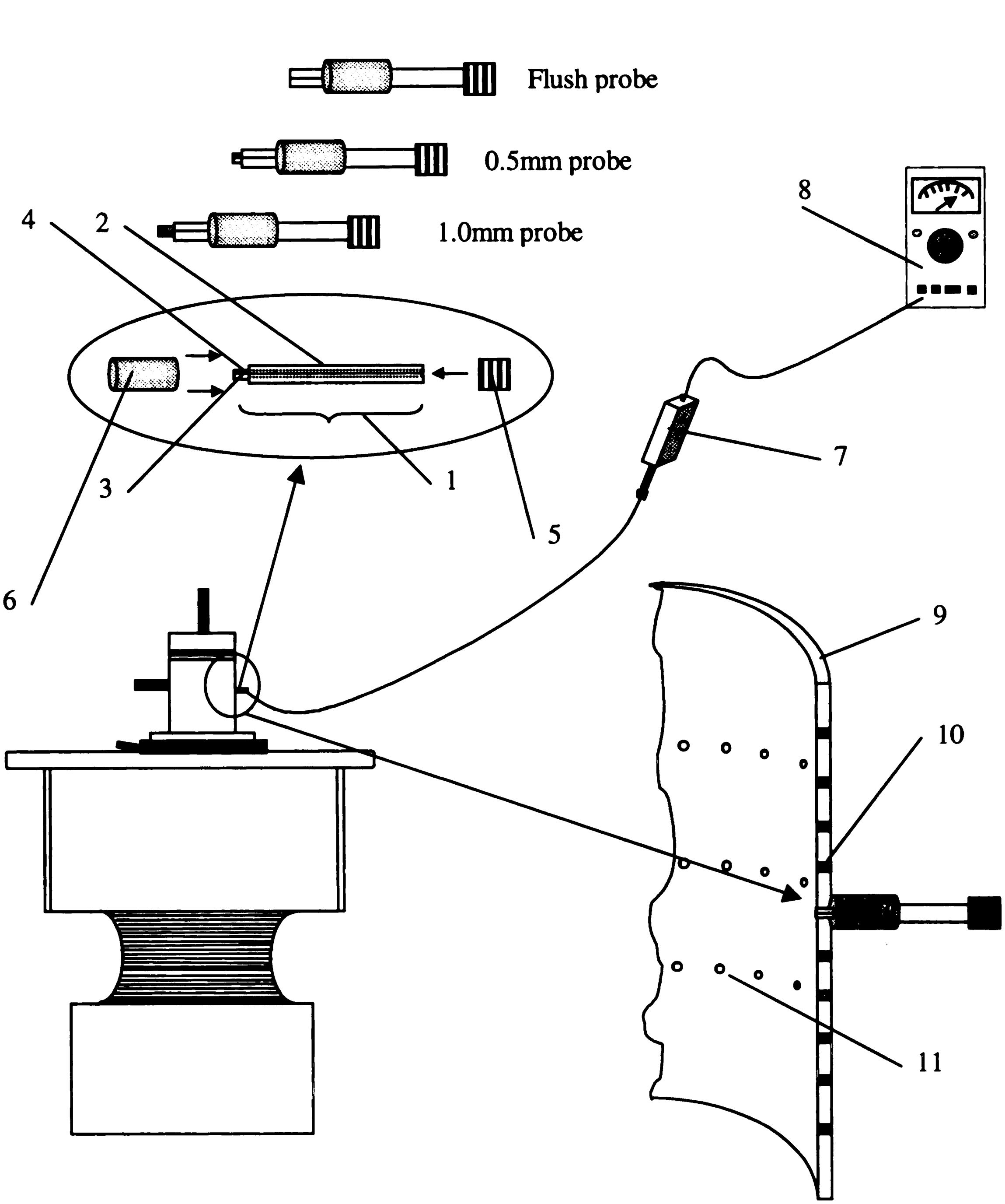

Figure 3.7 E-field probe design and electric field measurement setup

1) Rigid copper coaxial cable
2) Outer conductor
3) Inner conductor
4) Dielectric
5) SMA connector
6) Brass collar
7) HP 8481A thermistor
8) HP 435A power meter
9) Cavity applicator shell
10) Vertical sampling holes
11) Horizontal sampling holes

3.3.3 Principles of operation – Burkhart's method

S. Burkhart in 1985 developed a technique by using an open ended coaxial probe (E-field probe) for the measurements of high power microwaves [24]. The probe insertion no more than flush with the cavity inner walls has an advantage of presenting no discontinuity to the incident microwaves. The field measurements were carried out once the cavity was operating under fully matched conditions i.e. with minimum reflected power (always less than 5% of the P_{inc}). The normal electric field component on the E - field probe inner conductor and is given by [24]:-

$$E_r = [2P/ Z_O]^{1/2} \text{ x } [K_r \pi a^2 \varepsilon_o \omega]^{-1} \quad (V/m),$$

where P is the power sampled with the E-field probe, Z_O is the characteristic impedance of the cable, which in our case is 50Ω, "a" is the center conductor radius (0.0254cm), ε_o is the permitivity of free space, and ω is the frequency of the oscillating fields (2.45GHz). The area multiplier K_r for a flush probe is equal to 3.846. By substituting the values of all the constants the above relation reduces to:

$$E_r = (1.88 \text{ x } 10^6)\, P^{1/2} \quad (V/m)$$

This relationship was employed in this thesis research to measure the electric field strength in the microwave cavity shell.

Chapter 4

Experimental Results

4.1 Introduction

As mentioned earlier three MPDR plasma sources are characterized in this thesis. In this chapter the MPDR 7 - Side Feed (SF) is extensively evaluated against a number of input variables and then MPDR 7 - End Feed Probe (EFP) and MPDR 7 - End Feed Loop (EFL) plasma source output performances are compared to the performance of the MPDR 7 - Side Feed (SF) plasma source. Finally, the experimental results are compared with the global plasma model. Thus in a broad sense this chapter is divided into two parts. The first part describes the experimental results of the measured internal variables (X) for the SF plasma source. Then part two compares: 1) the output performance of the three MPDR plasma sources and 2) the experimental results with the predictions from global plasma model.

The input variables parameter space (U) for the three plasma sources has already been given in Tables1.2 – 1.4 in Section 1.5.3 of Chapter One. A selected group of internal and the output variables were measured versus changes in the input variables U_1. Tables 4.1 – 4.3 display the internal variables (X) and the output variables (Y) measured for the MPDR plasma sources investigated in this study.

As seen from Table 4.1 the internal variables measured for the MPDR 7 – SF plasma source were the power absorbed (P_{abs}), absolute and spatial electric fields, plasma density, plasma potential, electron energy distribution functions (EEDF), electron temperature and ion saturation current. The output variable (Y) that was measured for this source was ion production cost.

For the end feed sources, both loop and probe excitation, the measured internal variables were the power absorbed (P_{abs}), plasma density and the ion saturation current. Again the measured output variable was ion production cost.

From Tables 4.1 – 4.3 it can be seen that the macroscopic controllable input variables space (U_1) is almost identical for all of the three plasma sources. The difference is in the input regimes of argon gas flow rate and absorbed power. Except for the method of excitation the reactor geometry variables space (U_2) for the three plasma sources are the same. The side and end feed sources differ slightly in applicator diameter and the method of coupling. The cavity applicator shell diameter of the end feed MPDR plasma sources is 0.9cm larger than that of the side feed source. This larger diameter allows the excitation of an additional propagating mode in the end feed sources. The cavity applicator shell of the side and the end feed plasma sources is made of brass and stainless steel respectively. For the three MPDR plasma sources it can be noted from the Tables 4.1 – 4.3 that the entire input variable space (U) is approximately constant except the method of microwave excitation. Thus for a given input condition, keeping the reactor geometry variables space (U_2) fixed, the influence of the method of excitation on the internal and output variables can be evaluated from the experiments presented in this thesis.

Input Variables (U)	Description	Experimental Range
Macroscopic controllable input variables U_1	Absorbed power P_{abs}	50-200 Watt
	Operating frequency	2.45GHz (CW)
	Discharge gas	99.99% Argon
	Chamber pressure	1-8 mTorr
	Flow rate	0.3 – 35sccm
	Cavity short length L_s	13.7 – 8.4cm
	Depth of excitation probe antenna L_p	1.2 – 1.9cm
Fixed reactor geometry variables U_2	Applicator size, type and the method of excitation	8.9cm diameter cylindrical brass cavity with side feed excitation
	Discharge chamber dimensions	Height 5.6cm, radius 3.5cm with a total discharge volume of $215.5cm^3$
	ECR magnet configuration	8 Pole 8 Magnets (8P/8M)

Internal variables (X)

- Power absorbed (P_{abs})
- Absolute and spatial electric fields
- Plasma density
- Plasma potential
- EEDF
- Electron temperature
- Ion saturation current

Output variables (Y)

- Reactor performance figures of merit
  - Ion production cost

Table 4.1 Internal and output variables measured for MPDR 7 – SF

Input Variables (U)	Description	Experimental Range
Macroscopic controllable input variables U_1	Absorbed power P_{abs}	100-150 Watt
	Operating frequency	2.45GHz (CW)
	Discharge gas	99.99% Argon
	Chamber pressure	1-8 mTorr
	Flow rate	Fixed at 20 sccm
	Cavity short length L_s	3.13 – 10.78cm
	Depth of excitation probe antenna L_p	0.97 – 3.82cm
Fixed reactor geometry variables U_2	Applicator size, type and the method of excitation	9.8cm diameter cylindrical stainless steel cavity with end feed excitation
	Discharge chamber dimensions	Height 5.6cm, radius 3.5cm with a total discharge volume of 215.5cm^3
	ECR magnet configuration	8 Pole 8 Magnets (8P/8M)

Internal variables (X)

- Power absorbed (P_{abs})
- Plasma density
- Ion saturation current

Output variables (Y)

- Reactor performance figures of merit
  - Ion production cost

Table 4.2 Internal and output variables measured for MPDR 7 – EFP

Input Variables (U)	Description	Experimental Range
Macroscopic controllable input variables U_1	Absorbed power P_{abs}	100-150 Watt
	Operating frequency	2.45GHz (CW)
	Discharge gas	99.99% Argon
	Chamber pressure	1-8 mTorr
	Flow rate	Fixed at 20 sccm
	Cavity short length L_s	4.575 – 8.075cm
	Depth of excitation loop antenna L_p	1.95 – 3.2cm
Fixed reactor geometry variables U_2	Applicator size, type and the method of excitation	9.8cm diameter cylindrical stainless steel cavity with end feed loop excitation
	Discharge chamber dimensions	Height 5.6cm, radius 3.5cm with a total discharge volume of 215.5cm^3
	ECR magnet configuration	8 Pole 8 Magnets (8P/8M)

Internal variables (X)

- Power absorbed (P_{abs})
- Plasma density
- Ion saturation current

Output variables (Y)

- Reactor performance figures of merit
  - Ion production cost

Table 4.3 Internal and output variables measured for MPDR 7 – EFL

Part I

4.2 Electric field measurements and identification of EM excitation modes in the MPDR 7 – SF plasma source

Measurement of the electric field radial component (E_r) impressed on the cavity walls is presented in this section. These measurements were made by sampling power using an E-field probe. The sampled power was then used to calculate the electric field strength by employing Burkart's method [24]. This technique was discussed in Section 3.3 of Chapter 3. For all input conditions the measurements were made once the discharge loaded cavity was tuned to the best possible match and the sampled data obtained from the E- field probes was then plotted to identify the excitation modes.

Figures 4.1a and 4.1b display the measured strength of the radial electric field at the cavity inner-conducting walls in the SF plasma source. This plot represents the field strength for an absorbed power of 200Watt, with a chamber pressure of 4mTorr, and 20sccm of argon gas flow rate. The electric field strength which was measured at two circumferential sampling probe hole arrays, at H = 4.3cm (low ring) and at H = 7.3cm (high ring), is shown in the Figure 4.1a. It is seen that the mode pattern verifies the presence of a TE_{111} mode. The field strength is found out to be maximum at $\phi = 0°$, 180° and 350°. The sampling holes at $\phi = 0°$ and 350° are next to the location where the excitation probe antenna is located (at H=5.6cm plane), and the sampling hole at $\phi = 180°$ is located directly across from the antenna probe.

Figure 4.1b displays the variation of electric field strength versus the z - direction. The data presented here is obtained from the vertical sampling holes located at $\phi = 180°$

(see Figure 4.2). The maximum electric field strength was recorded at the sampling hole located at H = 5.3cm. This sampling hole is located directly across from the excitation antenna probe. The radial component of the electric field is reduced as one moves axially from H = 5.6cm plane (this plane defines the junction of the excitation antenna probe and the cavity applicator shell) towards the sliding short top plate or towards the discharge. This demonstrates the existence of a standing electromagnetic field inside the cavity applicator. The electric field strength was very low and thus unrecordable along the entire vertical sampling hole array located at $\phi = 270°$ (see Figure 4.1a). This was found out to be true for all the input conditions.

Figure 4.2 displays the measured and the theoretical profiles of the electric field in the plasma source. Figures 4.3 and 4.4 display the electric field strength recorded at a chamber pressure of 8mTorr with two levels of absorbed power i.e. 200 and 150Watt. It is noted from the Figures 4.1, 4.3 and 4.4 that the circumferential variations in the electric field strength are the same for both low and high sampling rings. However in all the cases, at $\phi = 180°$, the field strength at the low sampling ring slightly exceeds that of the high ring.

The increase in the absorbed power accounts for an increase in the electric field strength in the cavity. This can be seen from the Figures 4.1, 4.3 and 4.4. Figure 4.5 summarizes this observation for the field strength at a fixed pressure of 8mTorr and three different power levels. Figure 4.6 shows the pressure dependence of the impressed electric field strength. Higher field intensities are recorded as the operating pressure is reduced.

The observations made from the electric field measurements are:-

1) A single mode is excited in the cavity and the spatial distribution of the electric field indicates that the TE_{111} mode is impressed on the discharge.

2) The excitation antenna probe does influence the measured electric field patterns i.e. as seen from the Figures 4.1, 4.3 and 4.4 the impressed E-field is higher at the probe plane, H = 5.6cm, and is also higher at the " probe side" of the cavity. This is probably caused by the evanescent probe "*near fields*".

3) The loaded quality factor "Q_L" of the cavity is mathematically expressed as:-

$$Q_L \propto E^2/P_{abs},$$

where P_{abs} is the power absorbed in the cavity and E is the impressed electric field. From the Figure 4.6 it is seen that for a constant input power, P_{abs}, the impressed electric field strength in the cavity decreases as the chamber pressure is increased. Thus the loaded quality factor "Q_L" of the cavity increases with decreasing pressure. On the other hand Figures 4.5 and 4.7 show that for a constant pressure, the electric field strength increases with the increasing absorbed power. The quality factor in this case increases slightly with increase in the input power. These results are summarized in the Table 4.4 by calculating the impressed electric field and finding out the ratio of E^2/P_{abs} at a fixed location in the cavity applicator, $\phi = 170°$, under various input conditions. It should be noted here that the Burkart's method is valid only for the flush probe. The 1mm probe was thus calibrated with the flush probe impressed electric fields at $\phi = 170°$.

Based on this limited data following conclusions are drawn:

(a) Holding the chamber pressure constant and increasing the absorbed power, increases the Q slightly.

(b) Holding absorbed power constant and decreasing the chamber pressure, increases the Q.

These results require further investigations by measuring the quality factor under a broader range of input conditions.

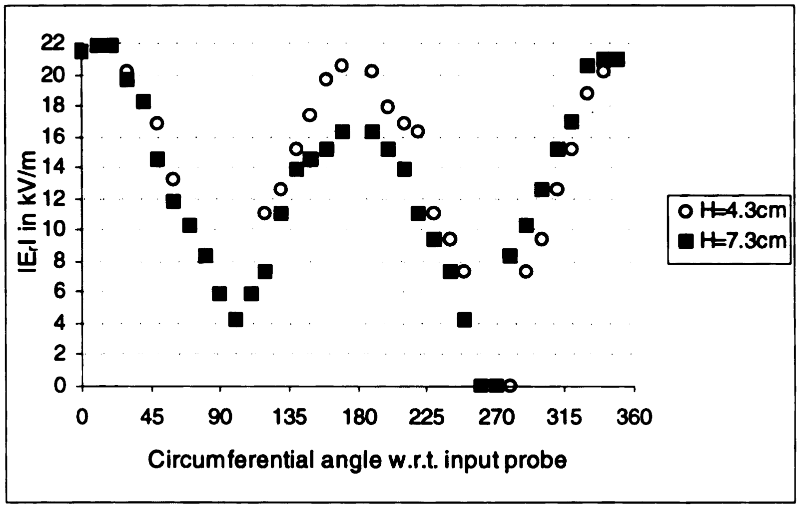

Figure 4.1a Circumferential variance of electric field strength in MPDR 7 – SF

Input power 200Watt, Pressure 4mTorr, and flow rate 20sccm

Data is obtained using flush probe

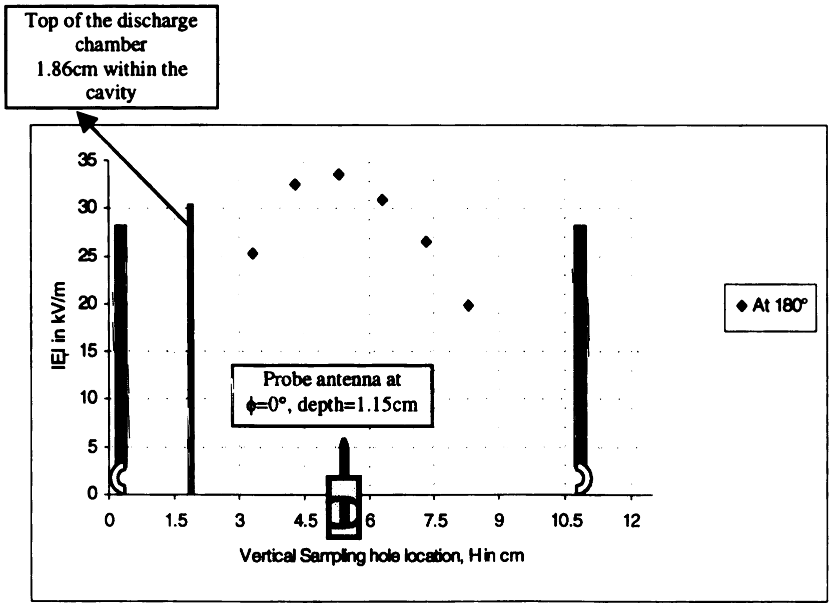

Figure 4.1b Longitudinal variance of electric field strength in MPDR 7 – SF

For vertical sampling hole array located at $\Phi = 180°$

Input power 200Watt, Pressure 4mTorr, and flow rate 20sccm

Data is obtained using flush probe

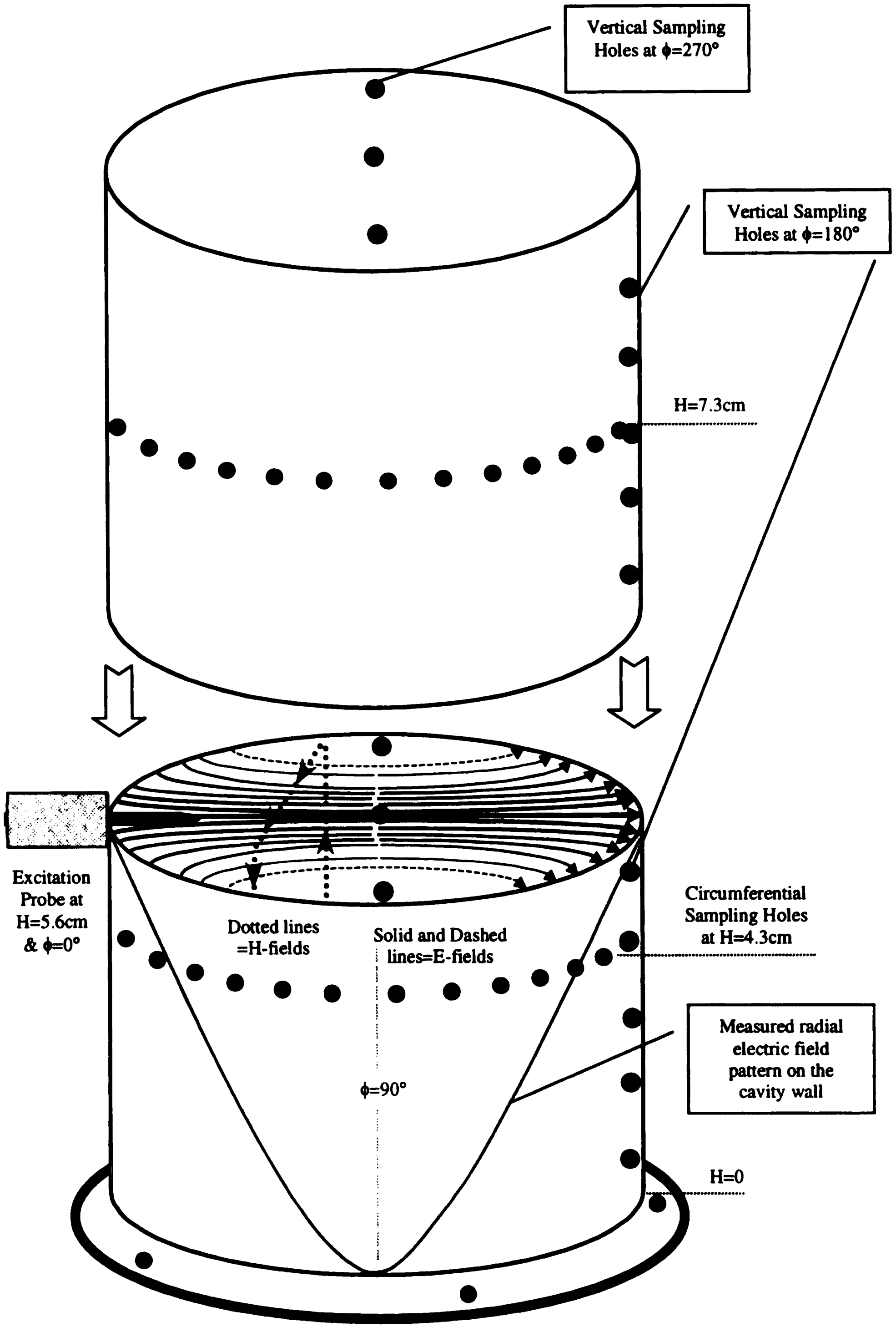

Figure 4.2 Electric field theoretical and measured profile within the MPDR 7 – SF ion source

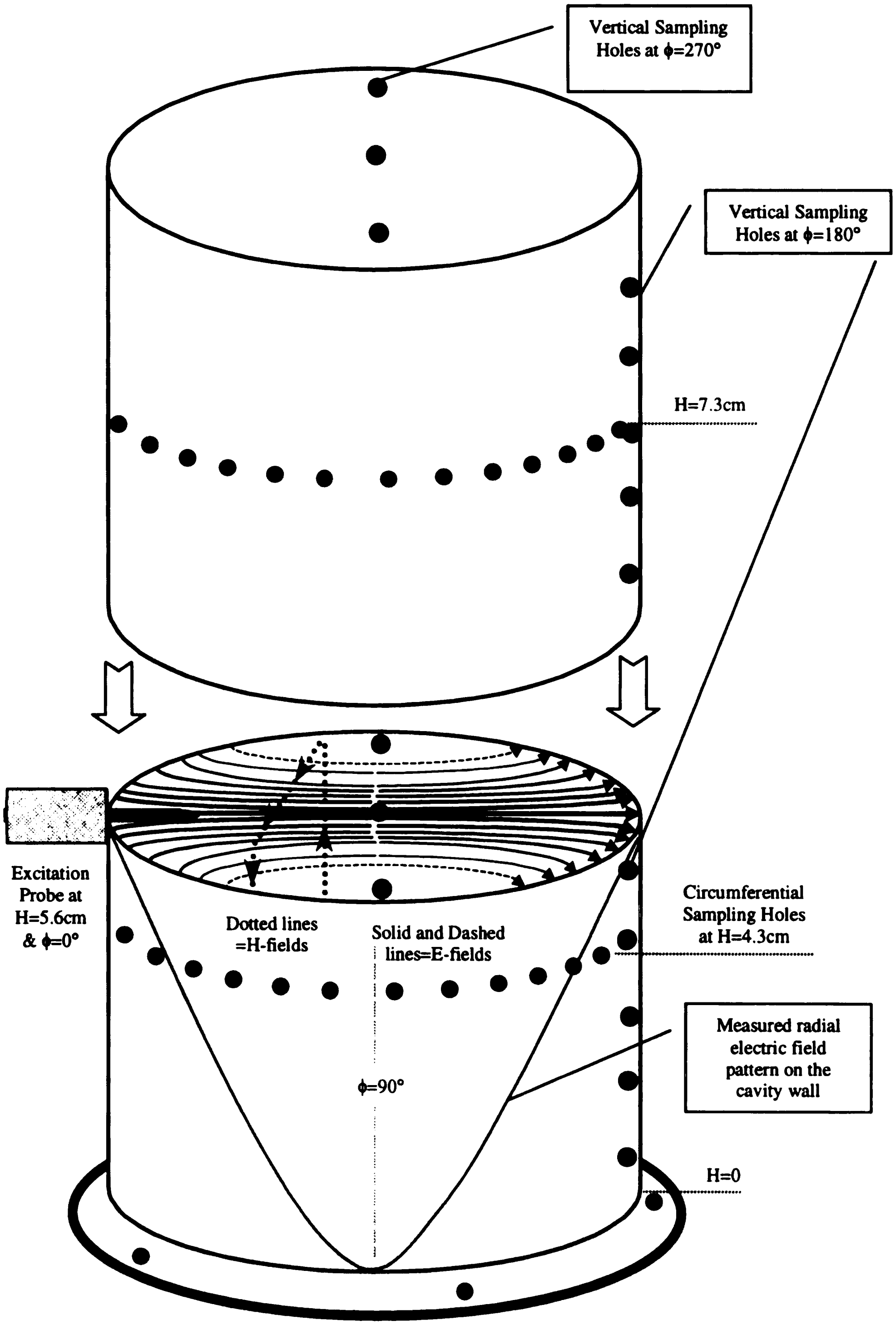

Figure 4.2 Electric field theoretical and measured profile within the MPDR 7 – SF ion source

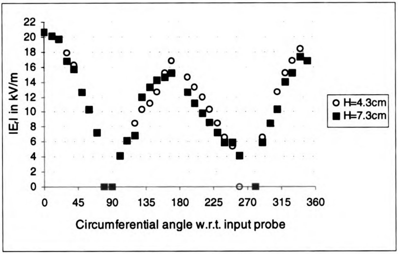

Figure 4.3a Circumferential variance of electric field strength in MPDR 7 – SF

Input power 200Watt, Pressure 8mTorr, and flow rate 20sccm

Data is obtained using flush probe

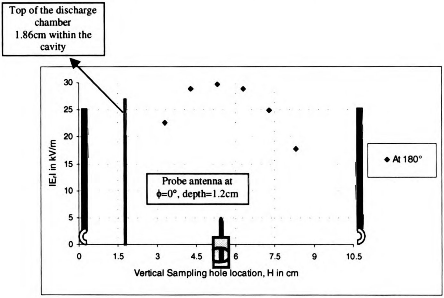

Figure 4.3b Longitudinal variance of electric field strength in MPDR 7 – SF

For vertical sampling hole array located at $\Phi = 180°$

Input power 200Watt, Pressure 8mTorr, and flow rate 20sccm

Data is obtained using flush probe

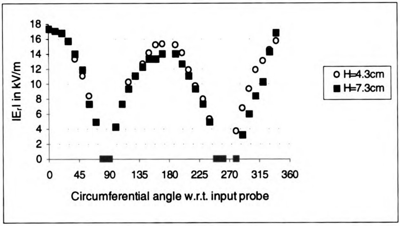

Figure 4.4a Circumferential variance of electric field strength in MPDR 7 – SF

Input power 150Watt, Pressure 8mTorr, and flow rate 20sccm

Data is obtained using flush probe

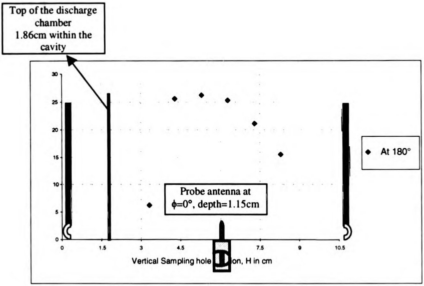

Figure 4.4b Longitudinal variance of electric field strength in MPDR 7 – SF

For vertical sampling hole array located at Φ = 180°

Input power 150Watt, Pressure 8mTorr, and flow rate 20sccm

Data is obtained using flush probe

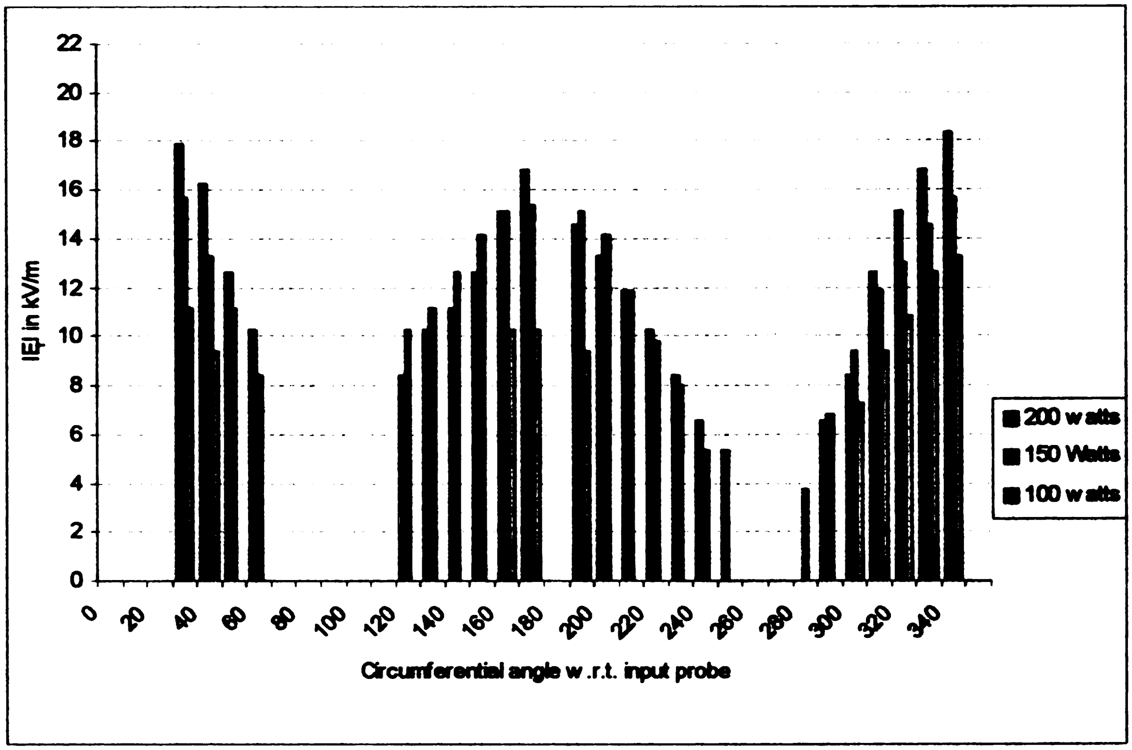

Figure 4.5 Circumferential variance of electric field strength in MPDR 7 – SF versus input power at H = 4.3cm plane

Input power 200,150&100Watt, Pressure 8mTorr, and flow rate 20sccm

Data is obtained using flush probe

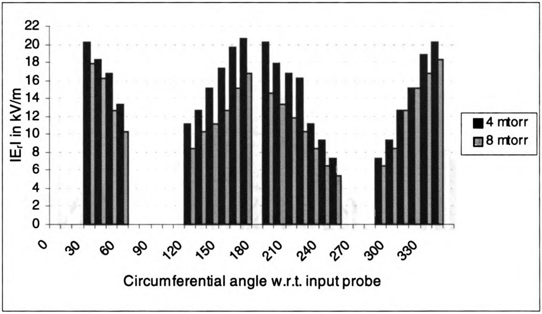

Figure 4.6 Circumferential variance of electric field strength vs. pressure in MPDR 7 – SF at H = 4.3cm plane

Input power 200Watt, Pressure 8 & 4mTorr, and flow rate 20sccm
Data is obtained using flush probe

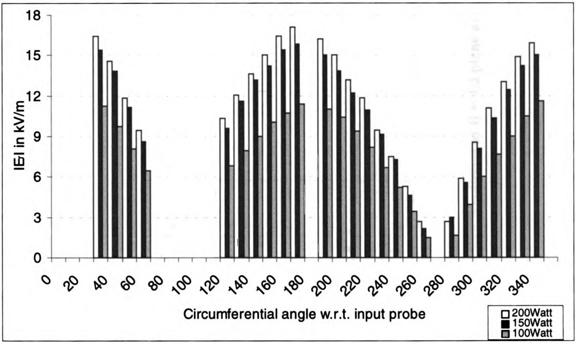

Figure 4.7 Circumferential variance of the electric field strength versus input power in MPDR 7 – SF at H = 4.3cm plane
The data is obtained using 1.0mm E-field sampling probe.
The probe is calibrated by flush probe.

P_{abs} (Watt)	Pressure (mTorr)	Flush probe data		1mm Probe data (calibrated)	
		E_r(kV/m)	E_r^2 / P_{abs}	E_r (kV/m)	E_r^2 / P_{abs}
200	8	16.8	1.41	17.1	1.46
150		15.4	1.58	15.81	1.6
100		10.3	1.06	11.41	1.3
200	8	16.8	1.413	17.1	1.46
	4	20.59	2.12	20.23	2.05

Table 4.4 E_r^2 / P_{abs} ratio for different input conditions at H = 4.3 plane and ϕ = 170°

4.3 Electron density in the MPDR 7 - SF plasma source

In the plasma based engineering applications, the need for process time estimation is very vital during the design optimization of a plasma-processing machine. Determination of this output parameter directly relates to the efficiency and the process economy. Within the plasma discharge, the higher the reactive species concentrations are, the faster the process rate and correspondingly the shorter procedural time. This section gives the results of the electron density measurements carried out for the MPDR 7 - SF ion and plasma source. The objectives of this section are: 1) to ascertain if the MPDR 7 –SF plasma source can be characterized as a high density plasma (HDP) source (the electron densities in excess of $1\text{x}10^{11}/\text{cm}^3$ is considered to be high density), and 2) to verify the sustainability of high density discharge at low pressure using ECR magnets.

Double Langmuir probes were used to extract the information about the electron densities in the argon gas plasma discharge which was ignited under different operating conditions. The Langmuir probe techniques employed are discussed in detail in Section 3.2 of Chapter 3. The diagnostic probe was positioned in the processing chamber at $z = 3\text{cm}$ and $r = 0\text{cm}$ as shown in the Figure 3.1 of Chapter 3. The equations of the global plasma model, which is discussed later in the Section 4.6, are based on the charge density at the source opening i.e. at $z = 0\text{cm}$ plane. Since the Langmuir probe was positioned at $z = 3\text{cm}$ plane, all the charge density measurements are multiplied by a factor of two. This factor is determined from the density measurements of P. Mak [14].

The cavity applicator was aligned so that its probe excitation antenna projection was located directly in between the two ECR magnets. See Figure 4.8. Throughout the entire experimentation process, the alignment of the coupling probe antenna with respect to the ECR magnets was kept identical.

Figure 4.9 displays the electron density data obtained as the source was operated with three absorbed power levels of 100, 150 and 200 Watt. The chamber pressure ranged from 1 - 8 mTorr while the gas flow rate was kept constant at 20 sccm. The measured data is plotted as symbols. The solid lines are the results from global model and are plotted here for reference. The experimental results demonstrate that the electron density increases with increase in the absorbed power and the operating pressure. The lowest electron density was $1.74 \times 10^{11}/\ cm^3$ which as recorded at a pressure of 1 mTorr for 100 Watt of absorbed power. The presence of ECR zones aided in the low-pressure operation of the MPDR source. The diffusion losses to the quartz discharge chamber walls may also be reduced due to the presence of ECR confining zones and thus high densities were recorded for this source. The ion source produced a maximum density of $4.08 \times 10^{11}/cm^3$ for 8 mTorr at 200 Watt.

It would be worth mentioning here that once the Langmuir probe was placed at z = 1cm (1cm below the ECR magnets), it produced erroneous results. This was due to the static magnetic fields from ECR magnets which interacted with the Langmuir probe electrodes. It is therefore advisable to keep the Langmuir probe electrodes away from the influence of the magnetic fields. Figure 4.10 displays the electron density vs. pressure curves for 100, 150 and 200 Watt at a fixed gas flow rate of 20 sccm. It may again be noted that at 1 mTorr, for all absorbed power values, the rate of increase in electron density is quite low as compared to the 8-mTorr data point.

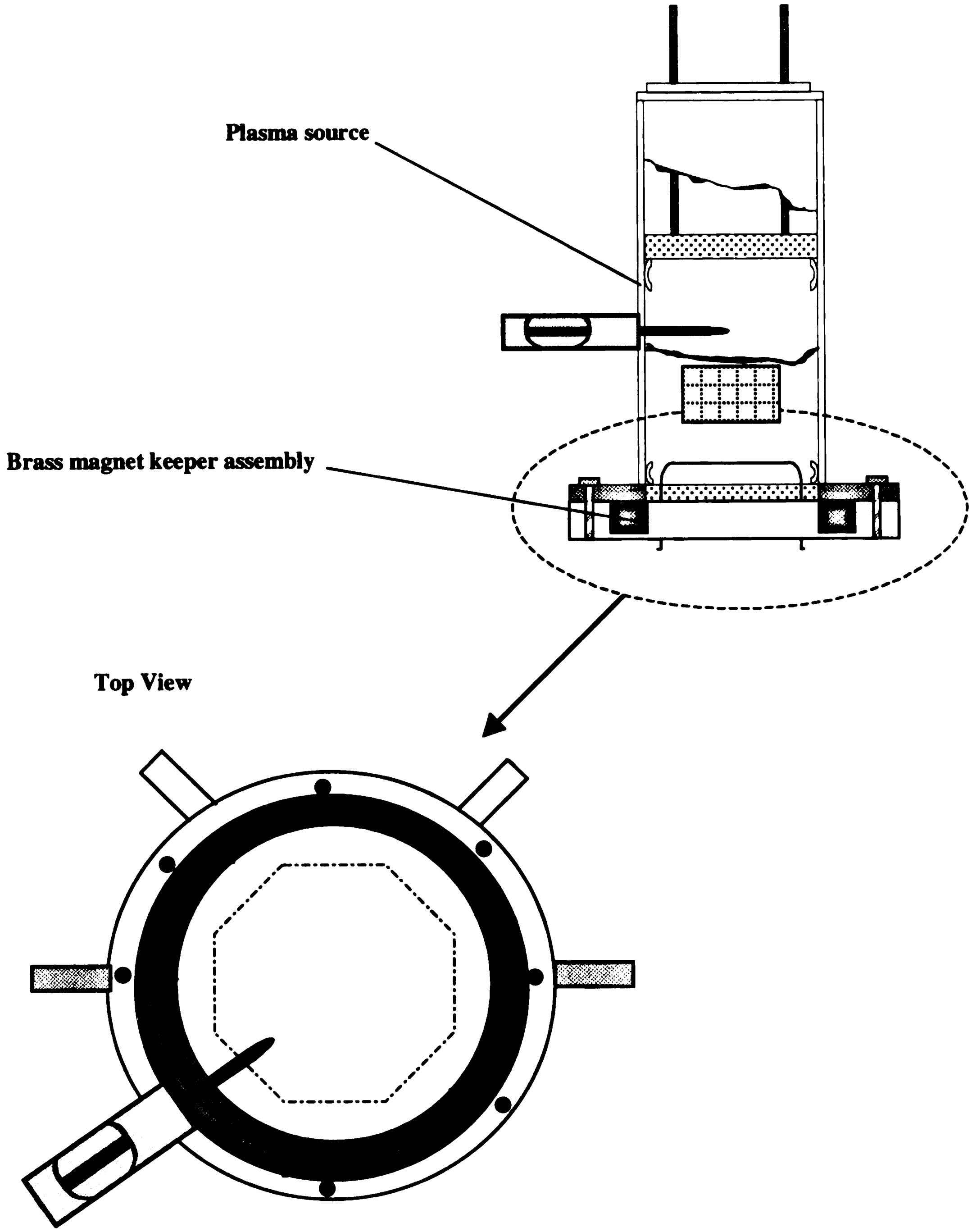

Figure 4.8 Top View projection of coupling antenna probe over the pole faces of ECR magnets

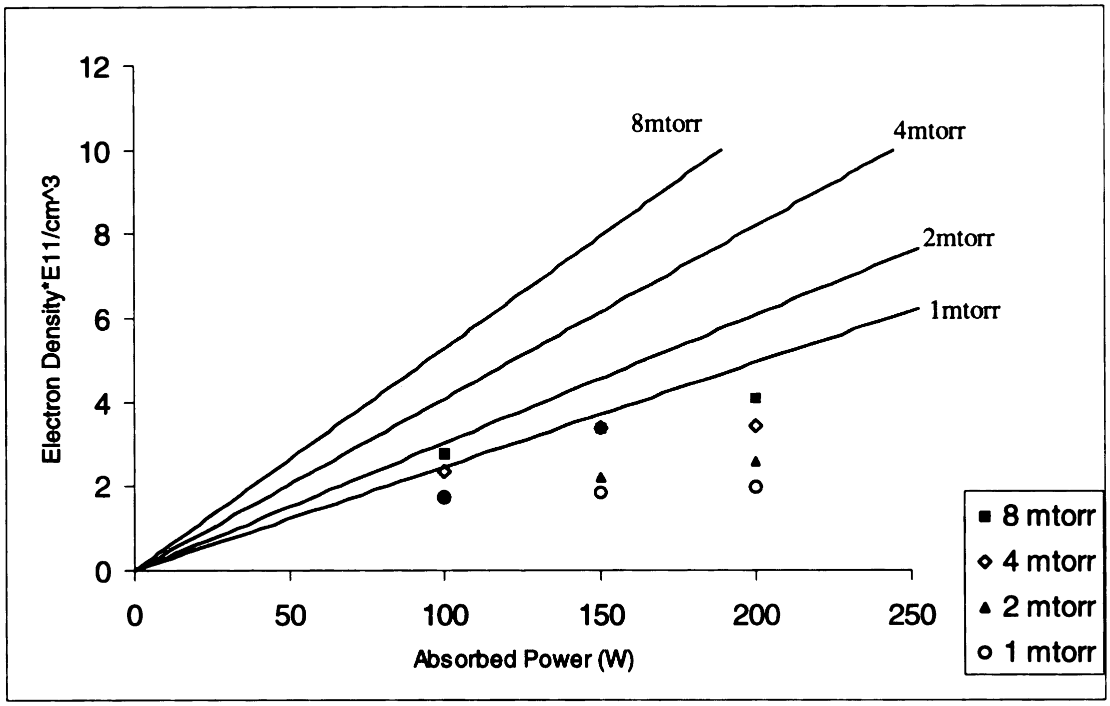

Figure 4.9 Electron density of MPDR 7 – SF plasma source as a function of absorbed power

Solid lines indicate Global model predictions

Pressure range 1 – 8mTorr at a fixed flow rate of 20sccm

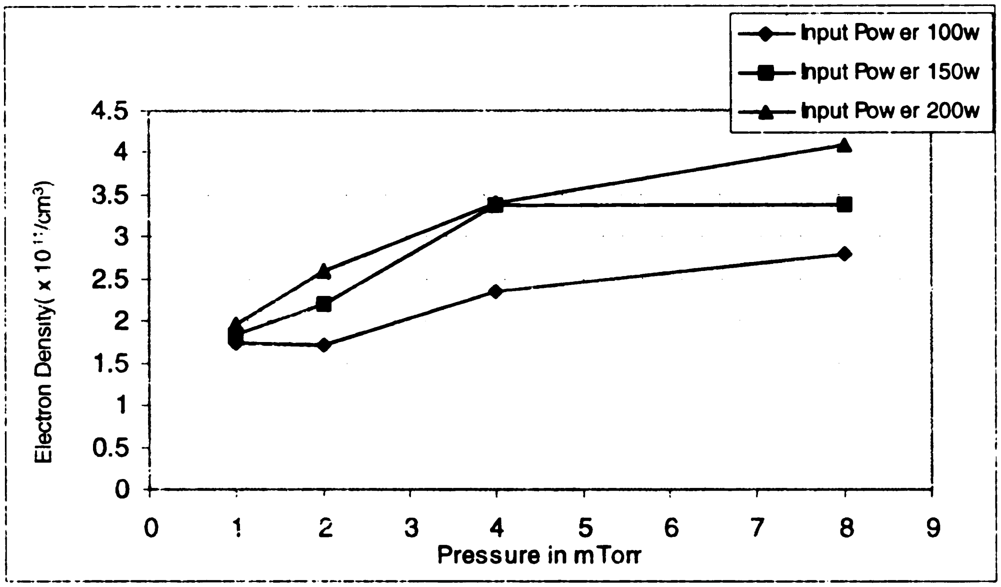

Figure 4.10 Electron density in MPDR 7 – SF as a function of chamber pressure at a fixed flow rate of 20sccm

4.4 Plasma potential and electron temperature

Plasma potential (V_p) and the electron temperature (T_e) were calculated from the data obtained from single Langmuir probe. The single Langmuir probe technique is discussed at Section 3.2.3 of Chapter 3. The probe was located at r = 0cm and the z = 3cm plane. The measurements were made for 100 and 150 Watt of absorbed power at a fixed flow rate of 20sccm and the chamber pressure range was 1 - 8mTorr.

Figures 4.11 and 4.12 show the experimental pressure dependency of both electron temperature and plasma potential. It is seen that both plasma potential and electron temperature decrease as the pressure increases. However the downward slope levels off as the pressure exceeds 4mTorr. This trend was also observed during the experimental evaluation of MPDR 9 and MPDR 13 plasma sources (both of them adopting the side feed coupling) where V_p and T_e exhibited a negligible pressure dependency for higher pressure (>3mTorr) [14, 25]. It is also observed from the Figures 4.11 and 4.12 that the plasma potential and electron temperature are relatively insensitive to the absorbed power.

4.5 Electron energy distribution function (EEDF)

Process control in plasma based applications requires an understanding of the transport properties of plasma constituents. The transport mechanism in a plasma discharge depends upon the kinetics and energy distribution of the reactive species. Plasma based processes are susceptible to the damage inflicted by the high-energy electrons impinging on the processed surface. Thus electron energy distribution function

(EEDF) becomes an important internal variable. This is the motivation for measuring the electron energy distribution (EEDF).

In a discharge, the electrons after gaining energy from the input microwave power may either collide or diffuse out of the source opening. Thus they are not mono-energetic rather they maintain an energy distribution within a discharge. Figures 4.13 – 4.16 show the typical normalized EEDF for the MPDR 7 – SF plasma source. The measurements were made using single Langmuir probe technique that is discussed in Section 3.2.3 of Chapter3. These plots represent the experimental results for the chamber pressure range of 1 - 8mTorr with a flow rate of 20sccm and 100 Watt of absorbed power. It is found out that the measured EEDFs more closely follow the Druyvesteyn distribution rather then the Maxwellian distribution. This is in agreement with the results presented by the earlier researchers [12, 14]. It is noted from the Figures 4.13 – 4.16 that the measured electron energies are even slightly lower than the Druyvesteyn distribution. Thus absence of high-energy electrons in the processing region is attributed to elastic and inelastic collisions as they diffuse downstream into the measurement region.

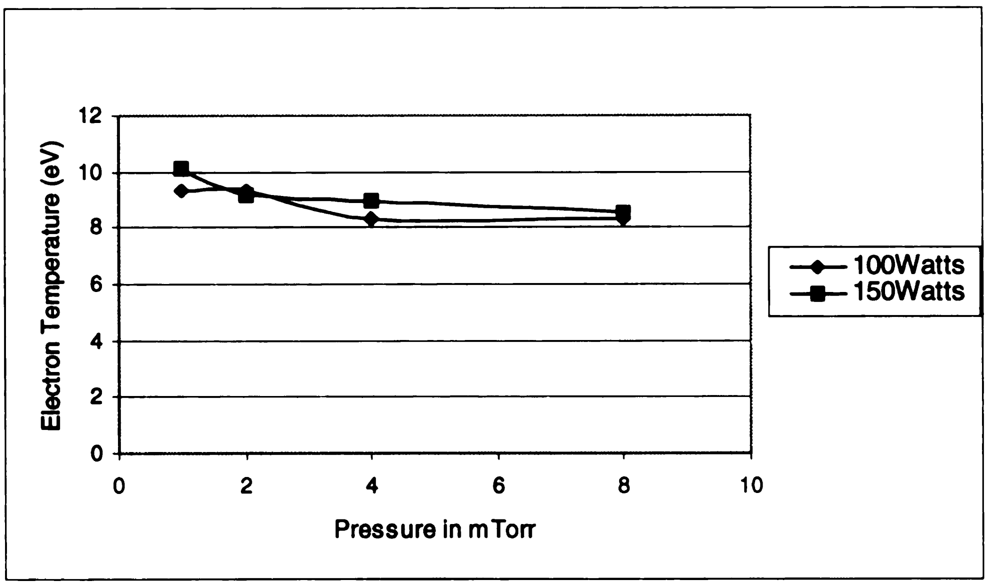

Figure 4.11 Electron temperature vs. chamber pressure in MPDR 7 – SF for 100 and 150 Watt of input power at 20sccm

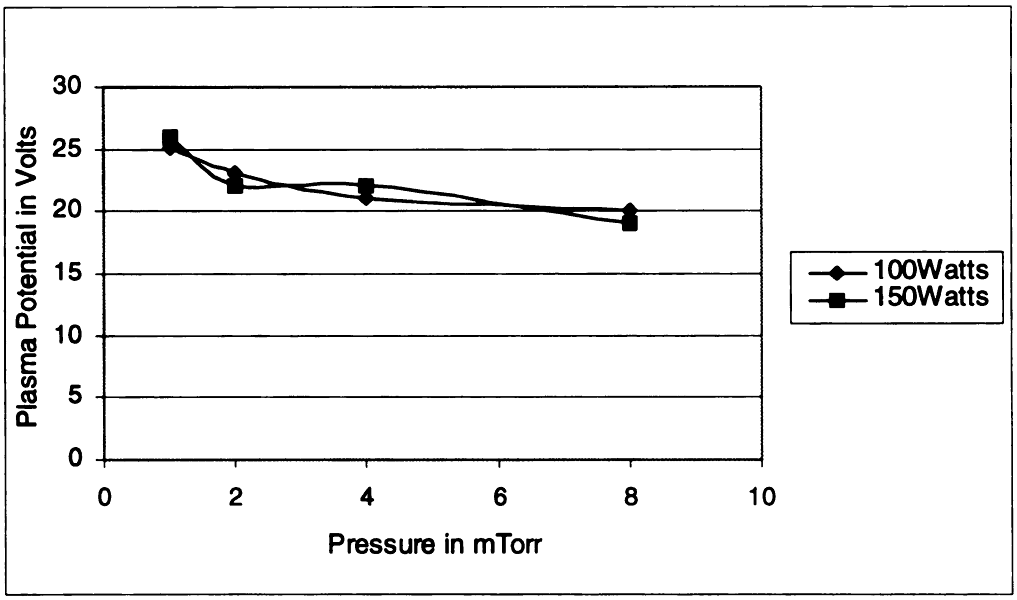

Figure 4.12 Plasma potential vs. chamber pressure in MPDR 7 – SF for 100 and 150 Watt of input power at 20sccm

"□" Represents Maxwellian Distribution
"o" Represents the Measured Distribution
"Solid line" Represents Druyvesteyn Distribution

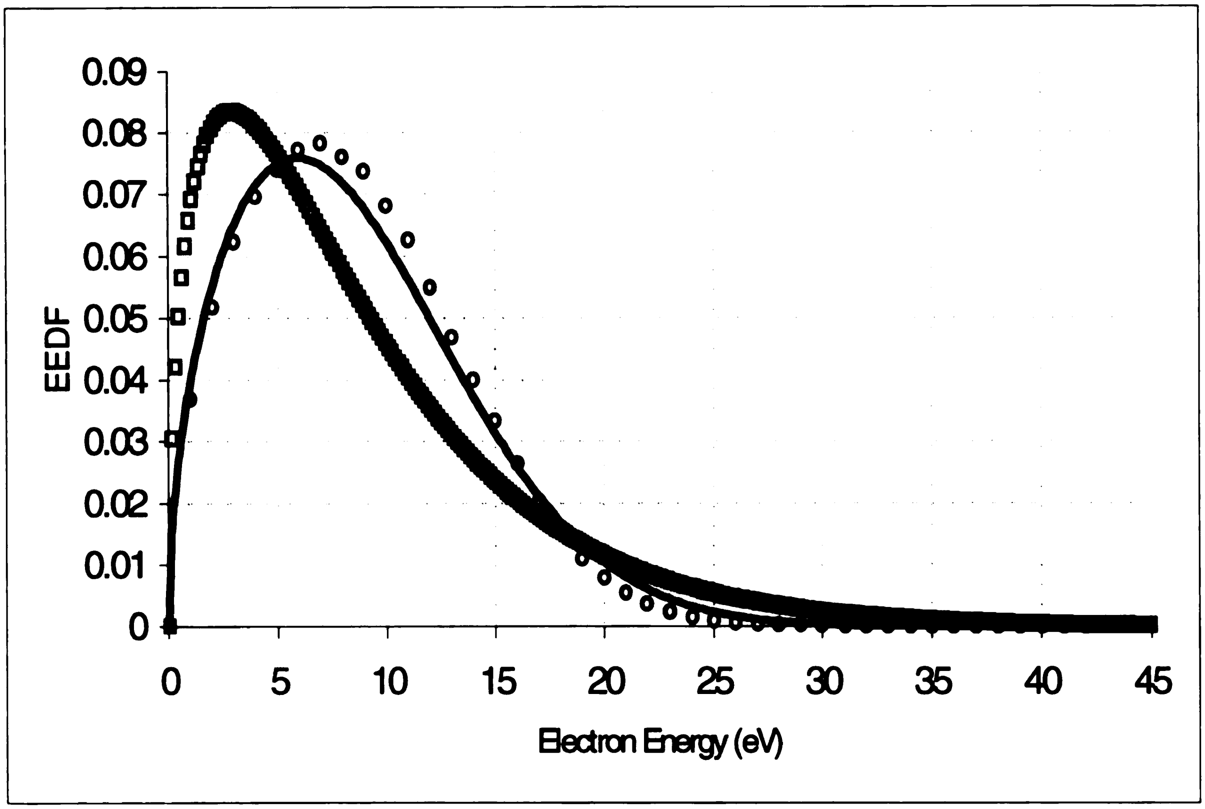

Figure 4.13 Electron Energy Distribution Function (EEDF) at z = 3cm downstream

Input Power 100 Watt, Pressure 1mtorr, Argon gas flow rate 20sccm

"□" Represents Maxwellian Distribution

"o" Represents the Measured Distribution
"Solid line" Represents Druyvesteyn Distribution

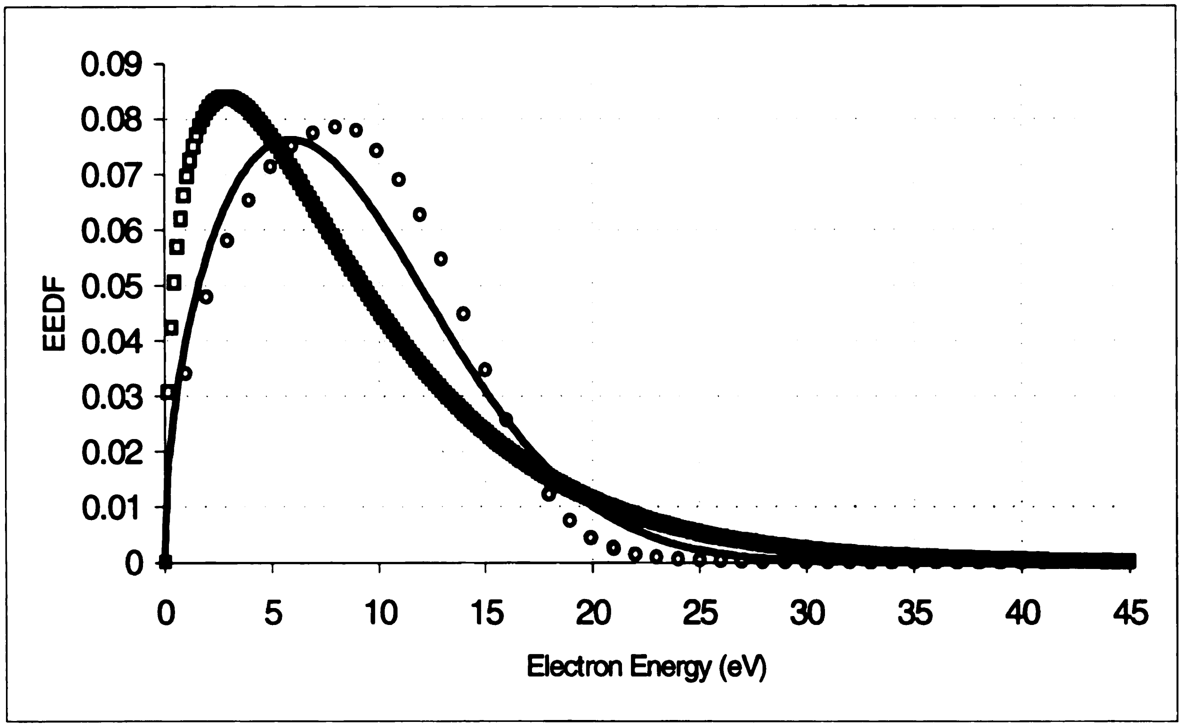

Figure 4.14 Electron Energy Distribution Function (EEDF) at z = 3cm downstream
Input Power 100 Watt, Pressure 2mtorr, Argon gas flow rate 20sccm

"□" Represents Maxwellian Distribution
"o" Represents The Measured Distribution
"Solid line" Represents Druyvesteyn Distribution

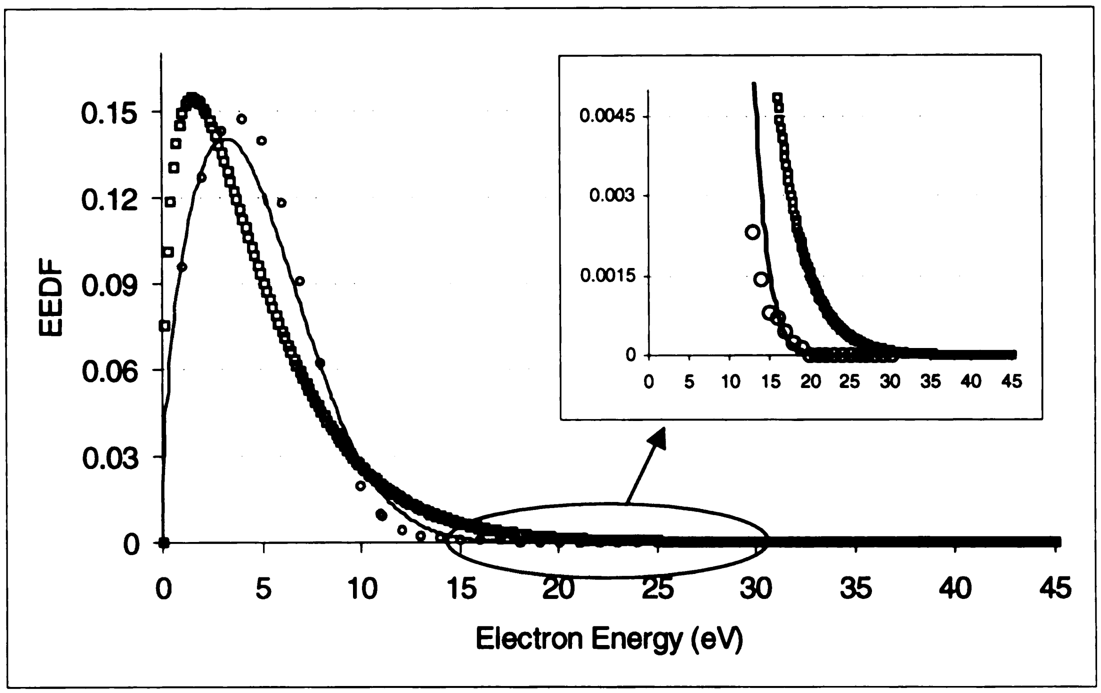

Figure 4.15 Electron Energy Distribution Function (EEDF) at z = 3cm downstream

Input Power 100 Watt, Pressure 4 mtorr, Argon gas flow rate 20sccm

"□" Represents Maxwellian Distribution
"o" Represents The Measured Distribution
"Solid line" Represents Druyvesteyn Distribution

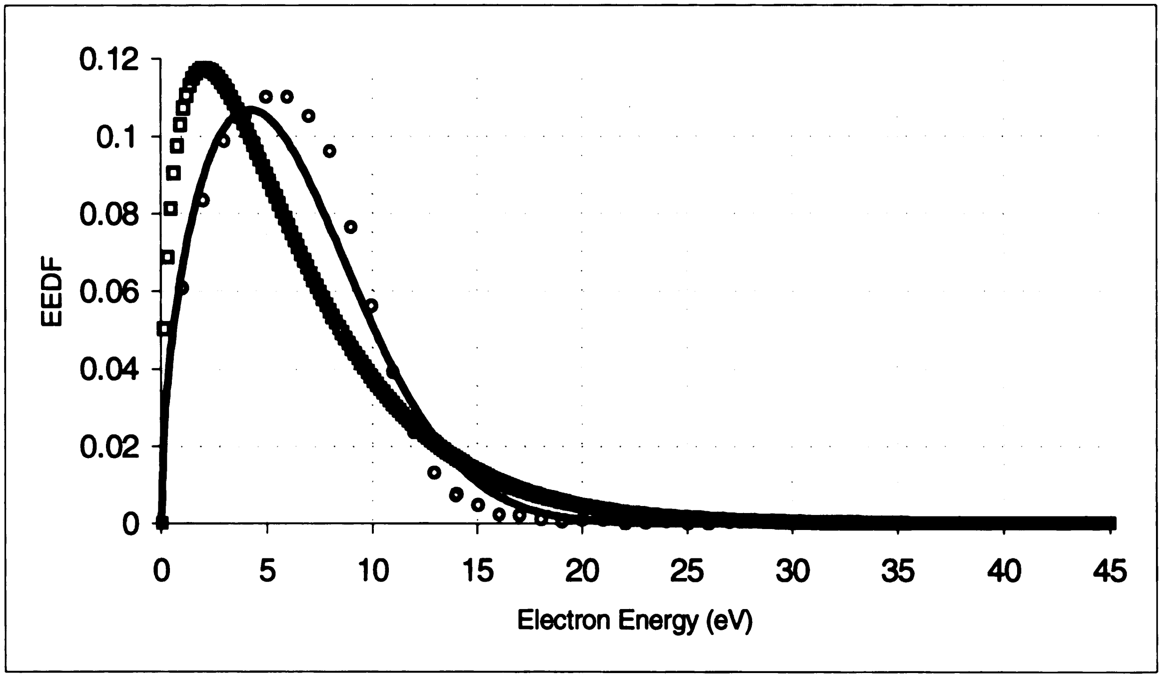

Figure 4.16 Electron Energy Distribution Function (EEDF) at z = 3cm downstream

Input Power 100 Watt, Pressure 8mtorr, Argon gas flow rate 20sccm

Part II

4.6 Global plasma model

The global plasma model, which is based on simple particle balance and power balance equations, has proved to be a useful model that can lend understanding to the behavior of the low-pressure argon gas discharges. A brief description of this model is presented here. A detailed description of global plasma model can be found in reference [26].

This model is based on the assumptions that:

1) electron energy follows a Maxwellian distribution.

2) electron-ion recombination occurs only on the chamber walls and is absent within the discharge itself.

3) at high pressures, electron and ion diffusion is governed by Schottky ambipolar diffusion and at low-pressures free fall ambipolar diffusion is dominant.

Based on the above assumptions, two equations were developed to describe the low-pressure discharge behavior. These equations are: 1) ion conservation, i.e., ion creation equals ion lost in every differential volume throughout the discharge, and 2) power balance, i.e., power absorbed (P_{abs}) in the plasma discharge equals the power lost by the electron gas by electron-neutral elastic and inelastic collision processes, and by the transfer of electron and ion kinetic energy to the walls.

4.6.1 Ion conservation relation

The low-pressure discharge is characterized by both collisional and collisionless diffusion of electrons and ions. The first is explained by the Schottky diffusion model where diffusion of charged species are governed by the ion and electron collision frequencies for momentum transfer. The later is based on an assumption that the ion mean free path, λ_i, is greater than the discharge dimensions. The ion mean free path for an argon gas is given by the following relation [27].

$$\lambda_i = 1/n_g\sigma_i \text{ cm} \cong 1/(330\,P) \text{ cm}, \tag{4.1}$$

where σ_i is the collisional cross section of argon ion ($10^{-14}cm^2$), and P is the pressure in Torr. The neutral gas density, n_g, is given by

$$n_g = P/KT_g \text{ m}^{-3}, \tag{4.2}$$

where P is the chamber pressure in Pascels, K is the Boltzmann constant and T_g is the gas temperature. Equation (4.1) has been derived assuming that T_g is 293°K. In this thesis the gas temperature T_g is assumed to be 600°K for the entire experimental pressure range of 1 – 8mTorr. Thus when using T_g = 600°K, equation (4.1) becomes $\lambda_i \cong 1/(161\ P)$ cm. The calculated λ_i for the operating pressures of 1, 2, 4, and 8mTorr are 6.2cm, 3.1cm, 1.55cm and 0.77cm respectively. Except near the walls (sheath region), the free fall diffusion model in the discharge assumes a quasi-neutral state i.e. ion and electron densities are equal, $n_i = n_e$. With a larger mean free path (λ_i), the charge species after being ionized diffuse from the discharge chamber onto the walls without experiencing any collisions. Thus the discharge is fairly uniform. A low-pressure discharge does not have any volume recombination processes, and thus every ion or electron created is lost at the walls. The plasma densities near the sheath in the axial and radial directions are represented by h_L and h_R respectively and are given by:

$$h_L = 0.86 / (3.0 + L/2\lambda_i)^{1/2} \tag{4.3}$$

$$h_R = 0.8 / (4.0 + R/\lambda_i)^{1/2} \tag{4.4}$$

The discharge chamber's (quartz dome) height, L, is 5.6cm and R the discharge radius is 3.5 cm. The experimental pressure regime in this thesis is 1 – 8mTorr. Within this range, the pressures of 1 and 2mTorr fall in the low-pressure regime thus h_L and h_R are approximated as 0.4 [26]. For 4 and 8mTorr, h_L and h_R are calculated using equations 4.3 and 4.4.

The ion conservation in the discharge is governed by the particle balance equation [26]:

$$K_{iz} / u_B = 1/ (n_g\, d_{eff}), \tag{4.5}$$

where K_{iz} is the electron ionization rate constant. Here u_B, the Bohm sheath criterion or the Bohm velocity is given by:

$$u_B = (eT_e/M)^{1/2}, \tag{4.6a}$$

where M is the mass of argon ion.

Thus

$$u_B = 1547.5(T_e)^{1/2}. \tag{4.6b}$$

In the equation (4.5), $d_{eff.}$ is the characteristic discharge length which is represented by:

$$d_{eff} = 0.5RL / (Rh_L + Lh_R) \tag{4.7}$$

Since both K_{iz} and u_B are functions of electron temperature, T_e, equation (4.5) demonstrates that the discharge electron temperature is a function of both neutral gas density n_g and characteristic diffusion length d_{eff}. For the experiments described in this thesis the calculated $d_{eff\ 1}$ and $d_{eff\ 2}$ are 2.69cm, $d_{eff\ 4}$ and $d_{eff\ 8}$ are 3.1cm and 3.62cm respectively, where the subscripts 1 – 8 correspond to the chamber pressure.

4.6.2 Power balance relation

The second global plasma model equation is the power balance equation which is given by [26]:

$$P_a = n_o e u_B A_{eff} E_T, \tag{4.8}$$

where n_o represents the electron or ion density at the center of the discharge. A_{eff} is the effective discharge area, which is equal to $2\pi R\,(Rh_L + Lh_R)$. The calculated values for each experimental pressure are $A_{eff\,1}$ and $A_{eff\,2} = 80.044\text{cm}^2$, $A_{eff\,4}$ and $A_{eff\,8}$ are 69.6cm^2 and $59.535\ \text{cm}^2$ respectively. In the equation (4.8) E_T is the total energy lost per ion-electron pair lost from the discharge. Mathematically it can be expressed as:

$$E_T = E_c + E_e + E_i \tag{4.9a}$$

The right hand side of the above equation represents collisional energy loss in creation of an electron-ion pair E_c, loss of kinetic energy as an electron collides with the walls E_e, and finally the loss of ion's kinetic energy across the sheath E_i. For Maxwellian electrons E_e is $2T_e$ and for argon ions the ion-bombarding energy, E_i, is $5.2T_e$. Thus the equation 4.9a can be rewritten as,

$$E_T = E_c + 7.2T_e. \tag{4.9b}$$

In the above equation T_e is the electron temperature which can be obtained either from a direct experimental measurement or by solving the conservation equation (4.5) for an uniform argon gas discharge. E_c is read from the E_c versus T_e curve plotted for argon, i.e. Figure 3.17, in the reference [26]. The values for E_T are $E_{T1} = 77.4\text{eV}$, $E_{T2} = 70.32\text{eV}$, $E_{T4} = 67.68\text{eV}$ and $E_{T8} = 66.64\text{eV}$, where the subscripts 1, 2, 4 and 8 denote the pressure in mTorr.

Equation 4.8 is also known as plasma load line equation and this relation can also be expressed in terms of average discharge power density $\langle P_a \rangle$ as:

$$\langle P_a \rangle = (n_o\, e\, u_B\, E_T) / d_{eff} \quad = P_a / (\pi R^2 L) \tag{4.10}$$

4.7 Excitation modes in the three MPDR plasma sources.

Out of the three plasma sources compared in this section, only the MPDR 7 - SF plasma source excites a single TE_{111} mode. The MPDR 7 - EFL and MPDR 7 - EFP plasma sources both excite two electromagnetic modes. These two modes by virtue of their location in the cavity applicator are identified in the discussion to follow as either a low or a high mode. For clarity, compare the matched tuning positions in the Table 4.5 for both low and high modes.

M. Perrin [15] demonstrated that the MPDR 7 - EFL plasma source can be tuned to either a TE_{111} mode (high mode) or a TM_{01}/TEM mode (low mode). In the preliminary investigations of the MPDR 7 - EFP plasma source, M. Perrin found out the existence of the TEM/TM_{01} (low mode) and TM_{01} modes (high mode). In case of the end feed MPDR plasma sources, the excitation antenna probe/ or loop in the low mode is close to the discharge chamber and thus the electromagnetic energy is coupled to the plasma discharge through electromagnetic fields that are the sum of the mode and the probe near fields. The five excitation modes and their matched tuning positions are tabulated in the Table 4.5.

Source Type	Description of the measured field pattern	EM mode	Matched tuning positions L_s and L_p in cm								Relative mode location in the cavity applicator
			100W-1mtorr		150W-1mtorr		100W-8mtorr		150W-8mtorr		
			L_s	L_p	L_s	L_p	L_s	L_p	L_s	L_p	
Side Feed (SF)	Dipole	TE_{111}	9.85	1.35	9.8	1.2	10.7	1.2	10.7	1.15	Single mode
End Feed Loop (EFL)	Φ Symmetric	TM_{01} or TEM	4.575	2.35	5.025	2.3	6.505	1.97	6.475	1.95	Low
	Dipole	TE_{111}	7.175	3.2	7.425	2.4	7.975	2.9	8.075	2.45	High
End Feed Probe (EFP)	Φ Symmetric	TEM or TM_{01}	5.07	3.17	5.39	3.52	6.22	3.82	5.92	3.57	Low
	Φ Symmetric	TM_{01}	11.97	1.1	12.67	0.97	10.07	1.89	12.72	1.37	High

Table 4.5 Excitation modes and their matched tuning positions for the three MPDR plasma sources

4.8 Performance comparison between global plasma model predictions and the experimental measurements of the three different coupling geometries.

The global plasma model discussed previously in the Section 4.6 provides an estimate of plasma source behavior by relating the variables (charge density and electron energy) with the input variables (chamber pressure, operating power and the discharge geometry). The objectives of this section are two fold:- 1) to compare the measured performance of the three MPDR ion and plasma sources with the predictions from the global plasma model, and 2) to ascertain the validity of the global plasma model for low pressure, high density, compact MPDR ion and plasma sources.

The solution to the particle balance equation 4.5 yields the curves, which have been reproduced here in the Figure 4.17. The dashed curve represents solutions from equation (4.5), i.e., the free fall diffusion solutions, and the solid curve symbolizes solutions from the Schottky diffusion model. The data points in the figure were recorded for the MPDR 7 – SF plasma source. These measurements were made for 100 and 150 Watt of absorbed power, chamber pressure of 1, 2, 4 and 8mTorr and the gas flow rate was fixed at 20sccm. It is seen that the experimental data points deviate considerably from the predicted free-fall diffusion model for the argon gas. They lie between the Schottky and free fall diffusion curves. The measured values continue to follow a downward trend, but as compared to the theory the slope is off by a large factor.

Using the power balance relation (discussed in the Section 4.6.2) a family of power loss load lines are shown in the Figure 4.9 of Section 4.3. The solid lines in the Figure 4.9 have been plotted using the equation 4.8. The data points in Figure 4.9

representing lower plasma density also correspond to lower input power. It is seen that the measured discharge density vs. P_{abs} follows the trend predicted by the global model but the experimental data points are offset by a certain factor for the entire pressure range. It can be observed from the figure that once the source is operated at higher input power the divergence between the measured and the predicted value increases. For example at 100 Watt the experimental data points are off by a factor of 1.4 – 1.8 while for 200 Watt it increases to 2.6 - 2.8.

Using the global model equations 4.5 and 4.10, the power density load lines are plotted in the Figures 4.18, 4.19, and 4.20. These figures compare the theoretical power density vs. plasma density with the measured experimental data. The solid lines in these figures show the discharge behavior as predicted by the global model for the chamber pressures of 1, 2, 4, and 8 mTorr. The data points display the experimental results for the pressure regime of 1 - 8mTorr and the input power of 100, 150 and 200 Watt for the side feed excitation configuration, 100 and 150 Watt for the end excited sources. As explained earlier, those data points in the Figures 4.18 - 4.20 which represent lower plasma density also correspond to lower input power levels.

The following general conclusions are drawn from the Figures 4.18 - 4.20:-

(1) It is seen that the end feed coupling geometry, in general, follows the global curves more closely than the side feed excitation. When the three excitations are compared, the MPDR 7 – EFP plasma source follows the theory more closely than the other two plasma sources.

(2) The power density in the MPDR 7 – SF plasma source is higher by a factor of 1.7 - 2.6 from the predicted value once the source operates at high powers

(150 – 200Watt). For the low power operation (100Watt) it deviates by a factor of 1.4 – 2.0.

(3) When the three MPDR plasma sources are operated at higher power (150 - 200 Watt for the side excited and 150 Watt for the end excited sources) the measured power density is higher from the predicted value by a factor of 1.2 – 2.6. While for the low power this factor varies between 1.5 below and 2.0 above the predicted value.

4.8.1 Comparison of the three plasma sources with the global model predictions using experimentally measured electron temperatures

The Figures 4.18 – 4.20 were plotted using the theoretical electron temperature, T_e, given by the global model equations. The Table 4.6 compares the theoretical and the experimentally measured T_e for the MPDR 7 – SF plasma source.

Pressure mTorr	Theoretical T_e eV	Experimentally measured T_e eV	
		100Watt	150Watt
1	7.0	9.36	10.1
2	5.6	9.31	9.205
4	4.4	8.3	8.96
8	3.7	8.312	8.529

Table 4.6 Experimental and theoretical electron temperatures (T_e) for the MPDR 7 – SF plasma source

It is seen from the Table 4.6 that the theory predicts low electron temperatures as compared to the temperatures measured experimentally. Thus it is worthwhile to use experimental T_e in the global model equations and compare the results with the measured data. The Figures 4.21 – 4.24 compare the theoretical and the experimental power load line curves when the measured T_e is inserted into the global model power balance equation (4.8) for two input power levels of 100 and 150Watt. Figures 4.21 and 4.22 show that at low input power (100 Watt), the experimental results agree fairly well with the theory, whereas the data in the Figure 4.9 displayed the differences of a factor of 1.4 – 1.8. It is also noted that as the operating power increases to 200Watt, the experimental data deviates from the theory by a factor of 1.2 – 1.7. Using the same power levels, the experimental results and the theory deviated by a factor of 2.6 – 2.8, as noted from the Figure 4.9. These new load lines curves suggest that it is possible that the discharge electron temperatures are higher than the temperature predicted by the global model equation. The agreement between the experimental and the theoretical load lines improves when the higher electron temperatures are used. This suggests that the higher experimentally measured electron temperatures may be valid and the theoretical electron temperatures predicted by the equation (4.5) are low. The power load lines shown in the Figures 4.23 and 4.24 use the experimental electron temperatures. Again the agreement between the theory and experiments is improved when experimental temperatures are used.

The difference between the measured electron temperatures and the electron temperatures predicted by the global model should be investigated further, first by checking the measured values and then by re-evaluating equation (4.5). If the measured electron temperatures are higher than the predictions by the global model then the ion conservation equation must be modified to include the correct physical phenomenon that results in higher electron temperatures.

The possible sources of error between the measured data and the theory are:-

1) The plasma density is measured at the edge of the discharge volume. The actual discharge density might still be higher than the measured density, even though the charge densities have been compensated by incorporating a correction factor of two.

2) The applicator conducting wall losses may possibly be larger (> 10% of the absorbed power) than has been assumed.

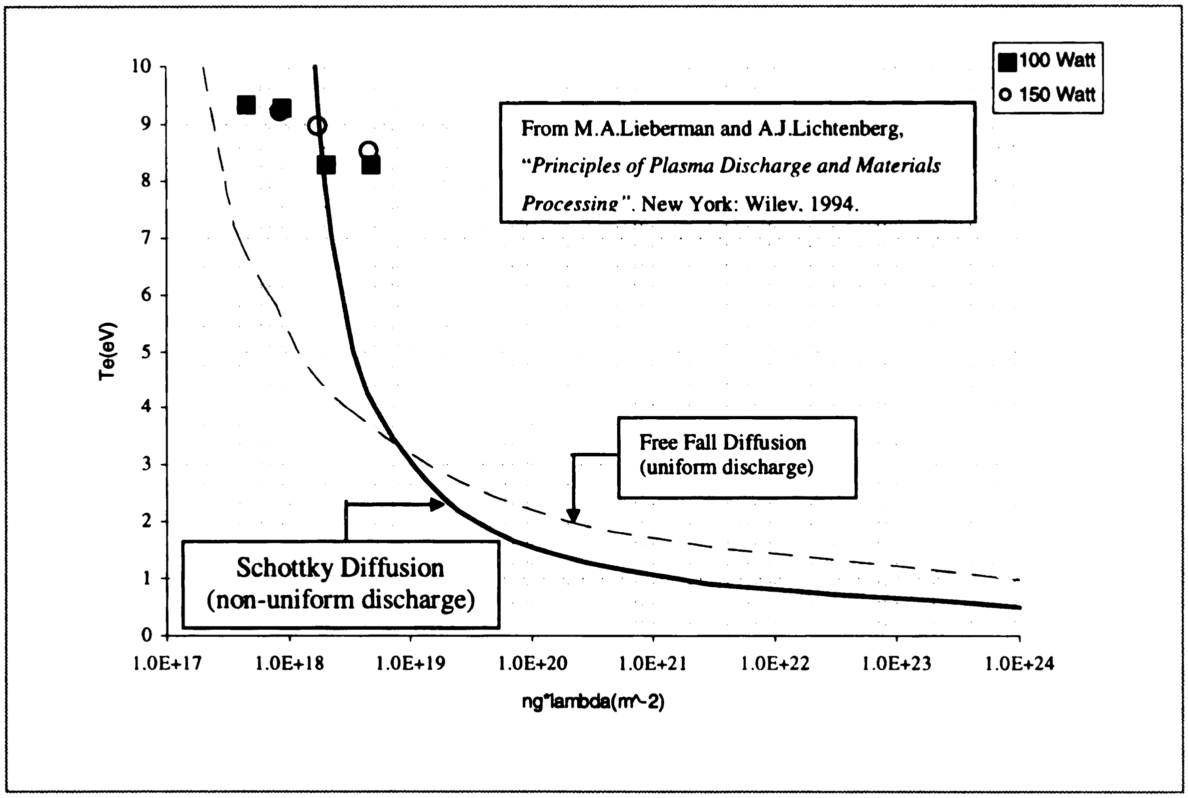

Figure 4.17 Experimental electron temperature (data points) plotted against the universal curves for free-fall and Schottky diffusion Argon gas discharges. MPDR 7 – SF plasma source

Input power 100 &150 Watt, chamber pressures of 1, 2, 4, & 8mTorr and gas flow rate fixed at 20sccm

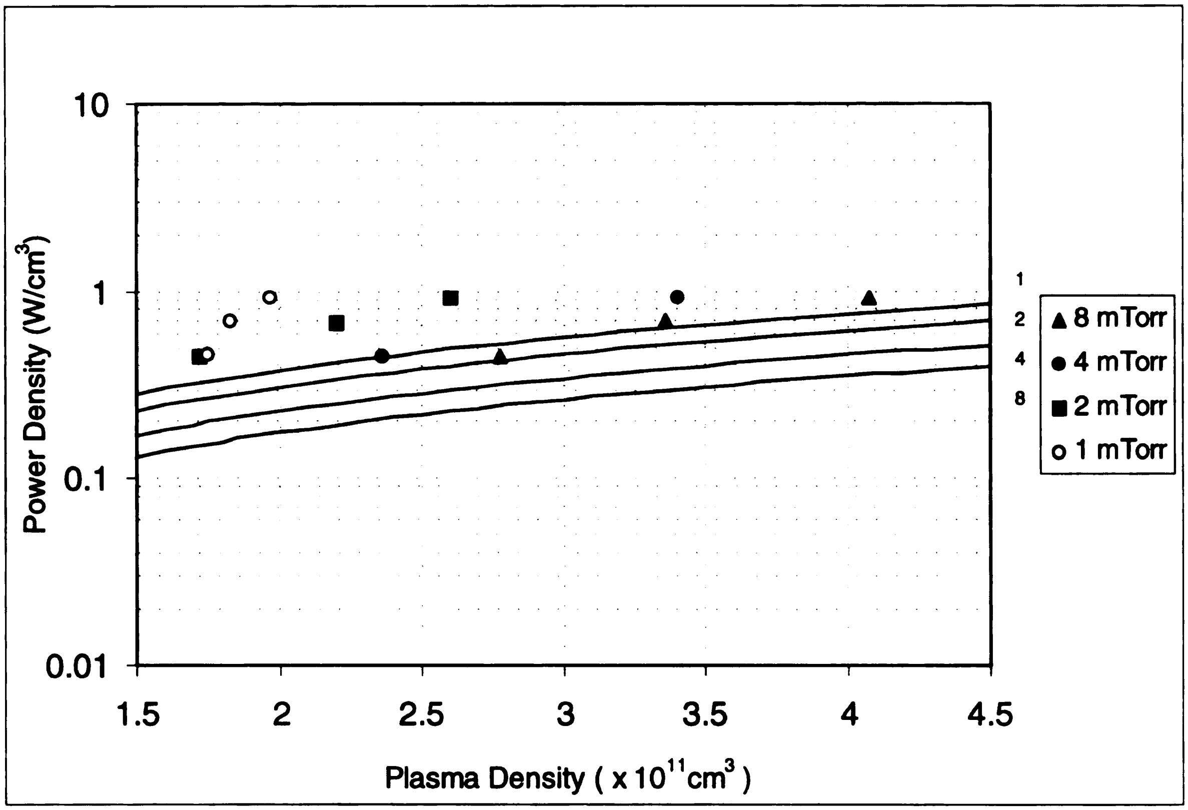

Figure 4.18 Power density load lines for MPDR 7 – SF
Pressure range 1 – 8mTorr
Solid curves represents global model predictions, and the experimental data is plotted as symbols.

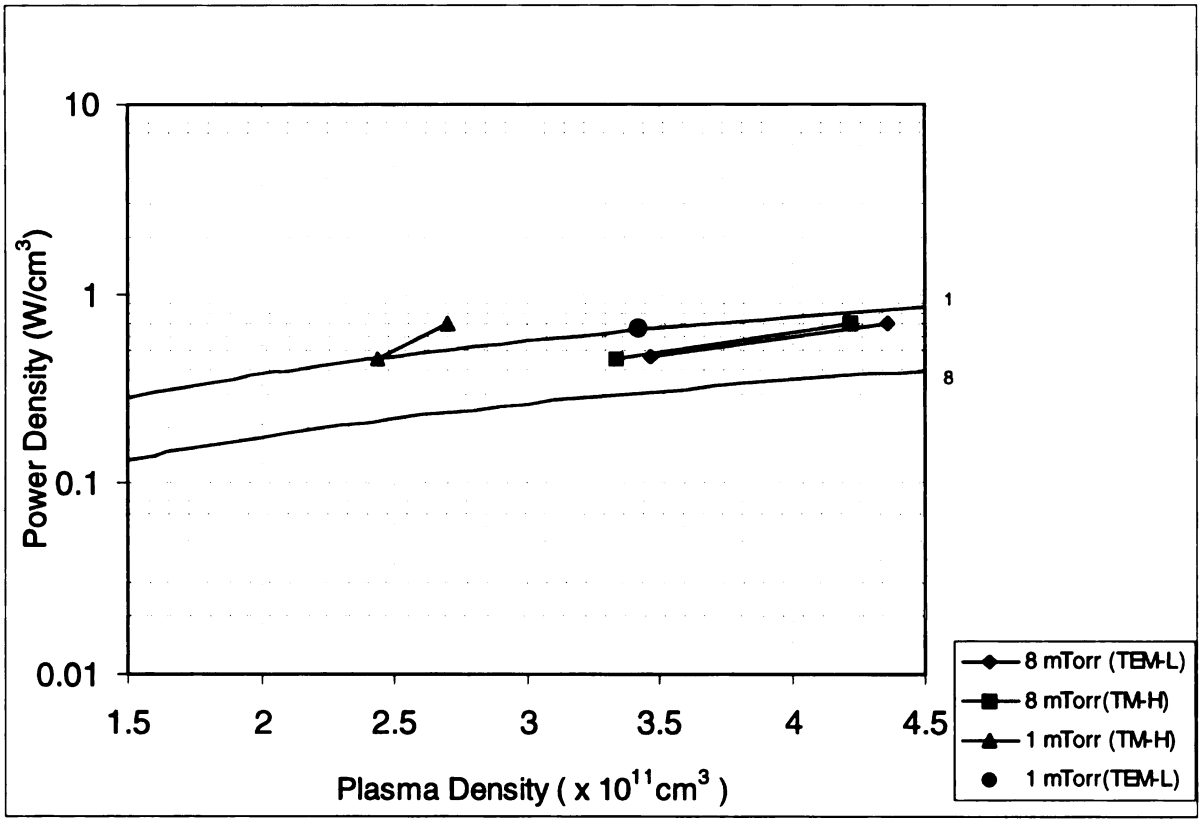

Figure 4.19 Power density load lines for MPDR 7 – EFP
Pressure range 1 – 8mTorr
Solid curves represents global model predictions, and the experimental data is plotted as symbols.

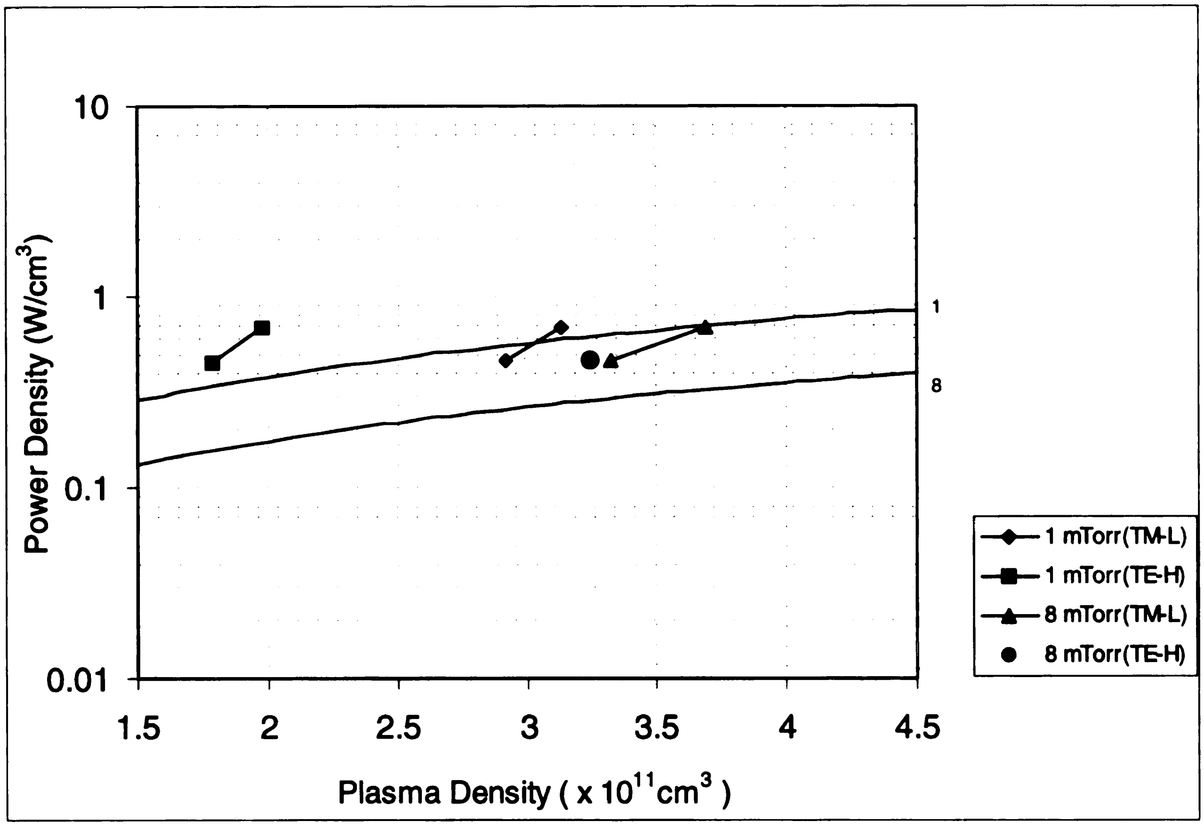

Figure 4.20 Power density load lines for MPDR 7 – EFL
Pressure range 1 – 8mTorr
Solid curves represents global model predictions, and the experimental data is plotted as symbols.

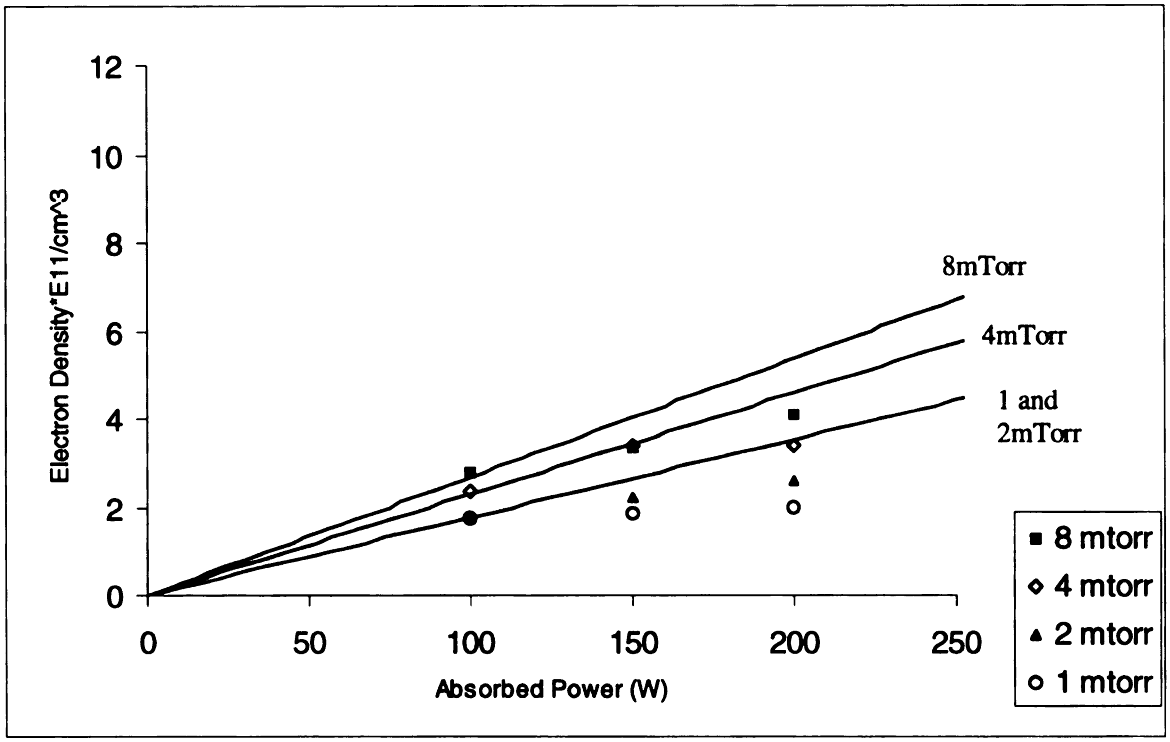

Figure 4.21 The Absorbed power load lines for MPDR 7 SF plasma source.

The solid lines are plotted using the measured electron temperature in the global model equations and the experimental data is displayed in symbols.
For input power of 100Watt.

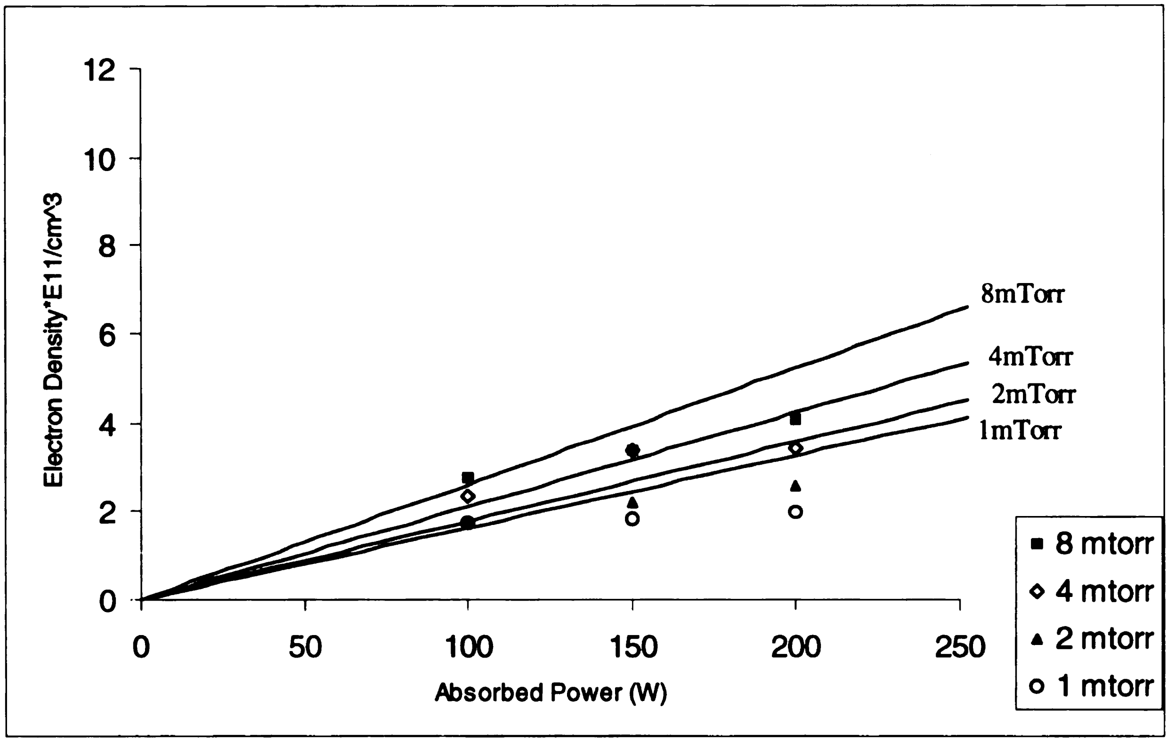

Figure 4.22 The Absorbed power load lines for MPDR 7 SF plasma source.

The solid lines are plotted using the measured electron temperature in the global model equations and the experimental data is displayed in symbols.
For input power of 150Watt.

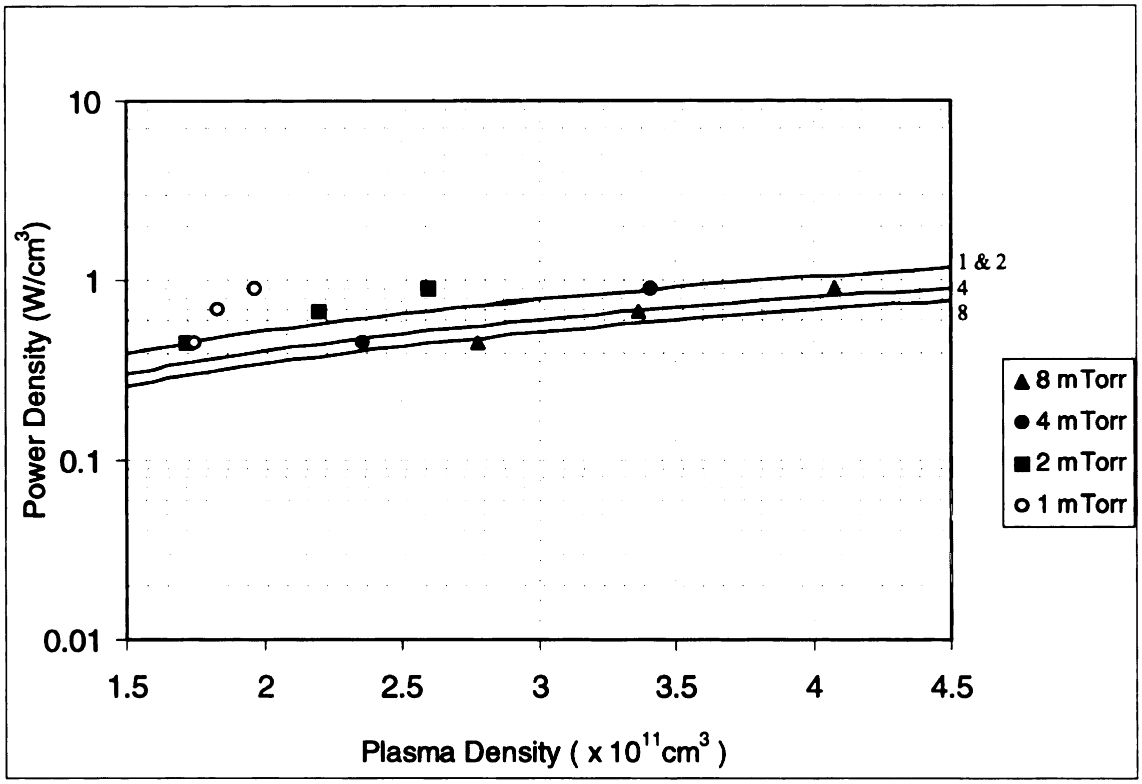

Figure 4.23 The Absorbed power load lines for MPDR 7 SF plasma source.

The solid lines are plotted using the measured electron temperature in the global model equations and the experimental data is displayed in symbols.
For input power of 150Watt.

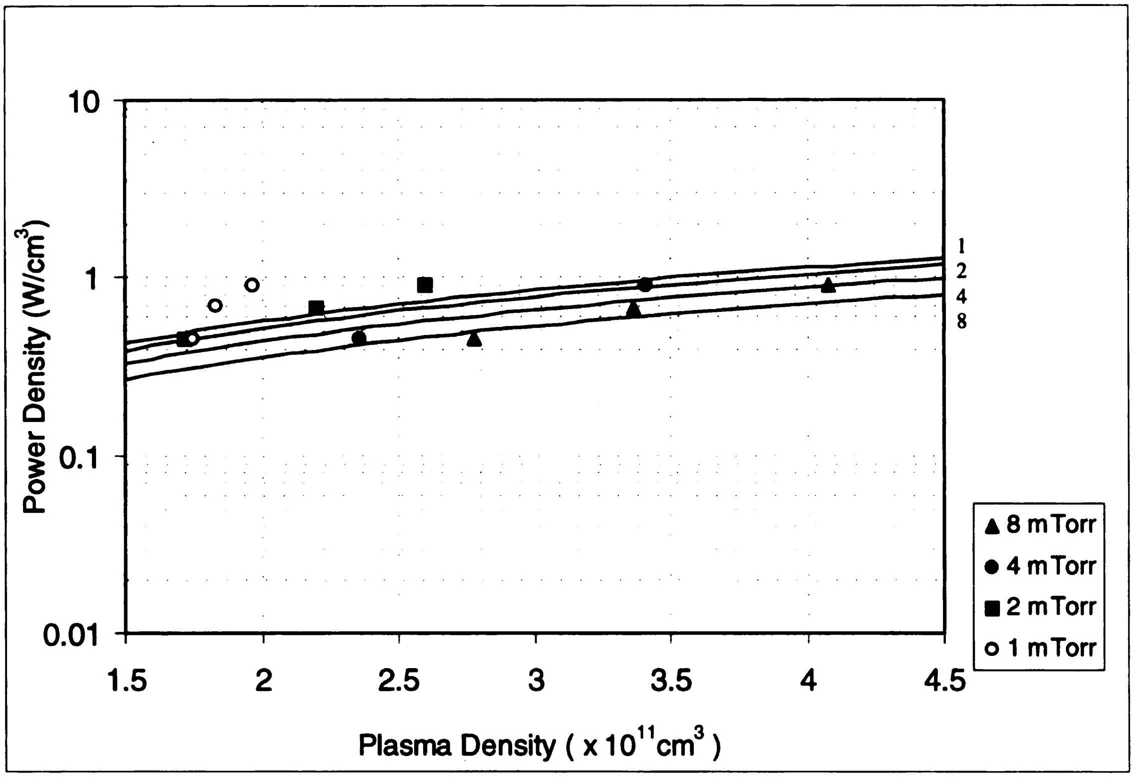

Figure 4.24 The Absorbed power load lines for MPDR 7 SF plasma source.

The solid lines are plotted using the measured electron temperature in the global model equations and the experimental data is displayed in symbols.
For input power of 150Watt.

4.9 Plasma source performance figure of merit – Ion production cost (eV/ion)

The ion production cost is a useful figure of merit that is helpful for comparing different plasma source designs. This section evaluates the performance of the three plasma sources in terms of ion production cost. The plasma source ion production costs are discussed in Sections 4.9.1 and 4.9.2. Similarities between the five excitation modes are discussed in the Section 4.9.3. The comparison of the ion production cost for the three MPDR sources is made in the Section 4.9.4 and then in the Section 4.9.5 these ion production costs are collectively compared with the other ECR reactor designs. In the Section 4.9.6 a summary of some interesting questions is given.

4.9.1 Experimental measurement of ion production cost

The ion production cost is defined as a ratio of the total input microwave power absorbed (P_{abs}) to the total ion current that can be extracted from the source opening at the z = 0 plane. This is also defined as the energy required to create a useful ion. It is assumed that despite the influence of the confining magnets, ions are still lost to the discharge chamber walls. The ion production cost takes into account only those ions, which diffuse downstream in the process chamber. The source efficiency which is determined by the ion production cost, is given by the relation [28]:

$$\eta = P_{abs} / \int_{A_s} \vec{J}_s . d\vec{S} \qquad (4.11)$$

where P_{abs} is the total power absorbed by the plasma source, J_s is the ion saturation current density at the z = 0 plane. The experimentally measured ion saturation current density, J_s, is given by:

$$J_s = I_s / A_p, \tag{4.12}$$

where I_s is the saturation current and A_p is the probe area = 2 π r x probe height + π r^2. The probe height and radius 'r' are 0.56 cm and 0.047 cm respectively and thus the probe area is 0.1723 cm^2. Assuming that the density is constant over the z = 0cm plane and then integrating the above equation yields:

$$\eta = P_{abs} / [(I_s / A_p) \times \pi R^2], \tag{4.13}$$

where "R" is the 3.5cm discharge chamber radius.

In the experimental data presented here the saturation current (I'_s) was measured using double Langmuir probes which were located at the z = 3cm plane, and the absorbed power (P_{abs}) was taken as the difference between the incident power (P_{inc}) and the reflected power (P_{ref}) i.e. $P_{abs} = P_{inc} - P_{ref}$. The P_{inc} and P_{ref} were read directly from the HP power meters. See Figure 2.2 in the Chapter Two. The discharge density at the source opening (z = 0 cm) was determined by multiplying I'_s, measured at the z = 3cm plane, by a factor of two to estimate the ion saturation current I_s at the z = 0cm plane.

It should be noted here that during the course of experimentation the electron temperature (T_e), which was measured with double Langmuir probes, varied under different input conditions. For example in case of end feed probe excitation T_e varied between 1.9 – 3.00 eV and for the end feed loop excitation it varied between 2.1 – 3.1 eV. This in return caused variations in the ion saturation current (I_s) thereby influencing the ion production costs. Thus the data displayed in the Figures 4.18 – 4.20 may not correspond to the ion production cost data presented later in this section.

4.9.2 Derivation of ion production cost from global model equations

The source efficiency, defined earlier by the equation 4.11, is the ratio of total power absorbed by the plasma source (input) to the flux diffusing downstream in the process chamber. The power balance equation (4.10) can be rewritten in terms of characteristic discharge length, d_{eff}, as

$$P_{abs} = (en_o u_B E_T \pi R^2 L) / d_{eff}, \tag{4.14}$$

where $\pi R^2 L$ defines the discharge volume. The diffusing flux, J_s, in the equation 4.11 is the flux of ions or electrons passing through the discharge opening at z = 0cm plane and is expressed as

$$J_s = en_o u_B h_L \tag{4.15}$$

Using this definition of flux and integrating it over the source opening, the denominator in the equation 4.11 can now be written as

$$\int_{A_s} \vec{J}_s . d\vec{S} = en_o u_B h_L \pi R^2 \tag{4.16}$$

Using the equation 4.14 and 4.16, the plasma source efficiency can now be expressed as

$$\eta = E_T\, L / d_{eff}\, h_L \tag{4.17}$$

By substituting d_{eff} from equation 4.7,

$$\eta = 2E_T \{1 + (L/R)(h_R/h_L)\} \tag{4.18}$$

This equation indicates that the ion production cost is a function of L, R, E_T, h_R, and h_L. L and R are the reactor geometry variables (U_2), and E_T, which is also a function of pressure, is an internal variable (X). The terms h_R, and h_L can be best described by the input variables space (U). However the equation (4.18) predicts that ion production costs are independent of input power.

4.9.3 Similarities between the five electromagnetic excitations

As seen from the Table 4.5 in Section 4.8, the three investigated MPDR plasma sources can excite five different electromagnetic excitations. The SF and the EFL (high mode) both excite the same TE_{111} mode. Thus these two excitations under the same input pressure and power conditions may yield similar ion production costs. The two end feed low mode excitations, i.e. the low mode in EFP and EFL, both couple to the discharge through near probe fields and TM (or TEM modes). Thus these two excitations may also yield very similar ion production costs under the same input conditions.

4.9.4 Performance comparison of three MPDR plasma sources

Figures 4.25 (a), (b) and (c) compare the performance, i.e. the ion production cost versus the SF, EFL and the EFP excitations as the pressure and the absorbed power are changed. The experiments clearly demonstrate that the ion production costs are a strong function of pressure and P_{abs}. A careful analysis of experimental data yields interesting observations and conclusions. Some of these are summarized below:-

(1) Ion production costs increase as the absorbed power increases, i.e. while the ion/electron density increases with an increase in the absorbed power the incremental power required to add an additional ion/electron pair also increases. This is clearly shown in the Figure 4.25a where the ion production costs vs. P_{abs} are presented for the SF excited plasma source. Earlier researchers, F.Sze and P.Mak [12, 14],

have also reported the degradation in the source efficiency with the increase in absorbed power for the larger diameter plasma sources (MPDR 325 and MPDR 13).

(2) From the equation (4.18), in Section 4.9.2, we see that the global model predicts that the plasma source efficiency should be independent of the absorbed power. But the experimental results in this thesis and also from the experimental work of the earlier researchers show that the source efficiency is a function of absorbed power. These experimental results, collectively, indicate that there are important experimental phenomenon which are not included in the global model. For example, the experiments point out that E_T is a function of absorbed power or is indirectly a function of the electric fields impressed on the discharge.

(3) The Figure 4.25b compares the theory with the experimental results for the side feed excitation. The theoretical data presented in the figure is obtained using the global model power balance equation, which employs both theoretical and experimental electron temperature (T_e). Following conclusions are drawn from the Figure 4.25b:-

(a) At higher pressures of 4 and 8 mTorr, the theory and experimental results agree within approximately 30%.

(b) At the low pressures of 1 and 2 mTorr the measured ion production costs are almost a factor of two higher than those predicted by the global model.

(c) The theory predicts an increase in the ion production cost from 308eV/ion at 8mTorr to 402eV/ion at 1mTorr, which is a 30% increase. Whereas the experimental data show a much larger increase in the ion production cost as the chamber pressure is decreased. For example as the pressure changes from 8mTorr to 1mTorr the ion production costs increase more than 50% for 100Watt and more than 80% for 150 and 200Watt.

(d) The agreement between the theory and the experimental results improves once experimental electron temperature (T_e) is used in the global model power balance equation.

(4) The Figure 4.25c compares the theory with the experimental results for the three plasma sources. For all the five excitations at a high pressure of 8mTorr and 100Watt of absorbed power, the ion production cost vary between 320 – 350 eV/ion and for 150Watt it vary between 355 – 440 eV/ion. That is the source efficiencies differ by less than 10% at 100Watt and ~ 20% at 150Watt. Thus it could be easily said here that the three investigated sources become more efficient when they were operated at higher pressure and low power. At these higher pressures their efficiencies are similar. However the source efficiency can degrade by a factor of two as we decrease the

operating pressure to 1mTorr. This is consistent with the earlier investigations [14].

(5) It is noted from the Figure 4.25c that the TE_{111} mode becomes least efficient when the MPDR 7 – SF and EFL plasma sources are operated at a high power (150Watt). Also note that these TE_{111} excitations become dramatically less efficient as pressure is reduced thereby giving much higher ion production costs than that predicted from the global model. The ion production cost increases from 425 eV/ion at 8mTorr to 800 eV/ion at 1mTorr. This difference may be due in part to the higher impressed EM fields in the cavity applicator at lower pressures which produces higher conducting wall coupling losses. The electric field measurements presented in the Figure 4.6 of Section 4.2 show an increase in the impressed electric fields as the pressure is reduced. The difference in the ion production costs may also be related to different heating and the diffusion mechanisms when the directions of the impressed electric field are varied on the low-pressure plasmas. This must be investigated further.

(6) It is seen from the Figure 4.26a that the TE_{111} mode produces similar ion production cost in both the SF and EFL excitations. This supports the observation discussed earlier that these two excitations are similar thus may produce similar ion production costs. Under the same input conditions of pressure and power the ion production costs are approximately the same for a similar excitation mode. The side feed

probe and the end feed coupling methods must have similar coupling efficiencies.

(7) From the Figure 4.26b it is seen that where the ion production cost data is available it indicates very similar ion production costs for both low EFL and EFP modes thereby supporting the idea that these two excitations are similar.

(8) Figure 4.26c displays a comparison of the high modes in the EFL and EFP excitations. It is seen that the TM_{01} mode, which is the high mode in the EFP excitation, is more efficient than the high mode (TE_{111}) excited by the EFL excitation. This implies that the high TM_{01} modes couple more efficiently to the discharge than the high TE_{111} mode excitations.

(9) Again referring back to the Figure 4.26b, it is noted that the ion production cost vary less than 30% for the low mode excitation in the end feed sources over the entire range of experimental input conditions. In fact the most efficient ion production cost occurs at 1mTorr with the EFL low mode exciting the discharge. The fact that the ion production cost do not dramatically increase at low pressures suggests that some unknown heating and/or diffusion processes are sustaining the discharge at low pressure when these low modes excite the discharge.

4.10 Performance comparison of the three plasma sources with other designs

Figure 4.27 compares the three MPDR ion and plasma sources investigated in this thesis with larger diameter MPDR 325 plasma source and three other ECR reactor designs. The three different reactor concepts are: 1) divergent field ECR plasma source (div), 2) distributed ECR plasma source (decr), and 3) slotted antenna type ECR plasma sources (slan) in two discharge diameters i.e. 4cm diameter (μslan) and 16cm diameter (slanI). These plots represent the data already published in the reference [1,14] and is reproduced here for comparison. The efficiencies for the different ECR configurations vary over a large range. It may be noted that the MPDR concept for both compact and larger diameter sources stands out in terms of efficiency. While the reasons for the differences in between the efficiencies of the different reactor concepts are not understood, the large dissimilarities may be due to inefficient microwave coupling in the div, decr, and slan type reactors. Within the MPDR clan of plasma sources the larger diameter sources are found out to be more efficient than the compact plasma sources.

4.11 Summary

On the basis of the experimental results and their analysis presented in this section the following important questions have been left unanswered:-

- The influence of the conducting wall on the source efficiency needs to be determined.
- Since the most efficient discharges have some or substantial near field coupling to the discharge, does this near field plasma coupling play an important role in increasing plasma source efficiency?
- Why is TM_{01} mode coupling is more efficient than the TE_{111} mode coupling?

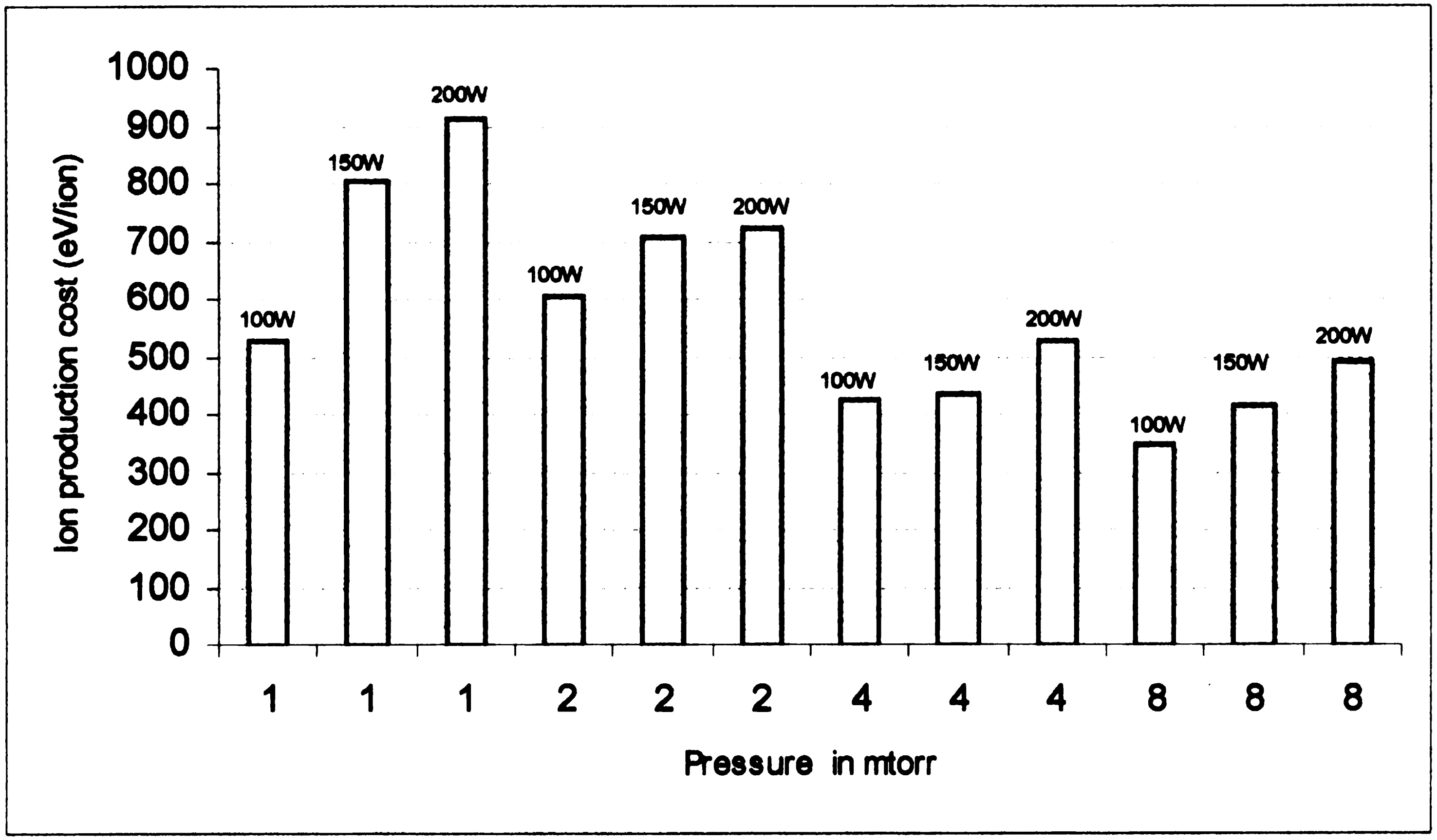

Figure 4.25a Ion production cost versus pressure – MPDR 7 – SF plasma source

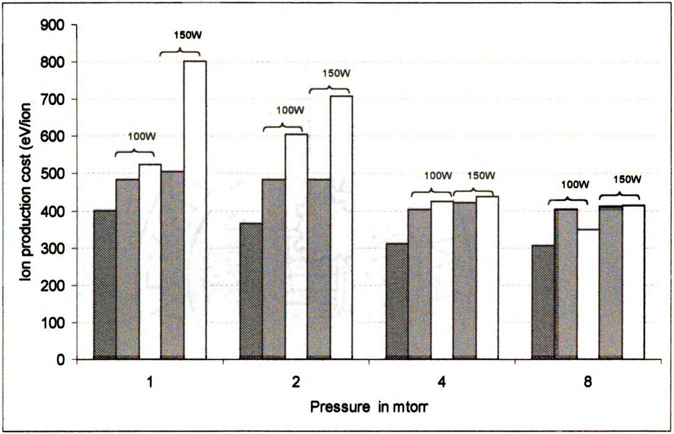

Figure 4.25b Ion production cost versus pressure -Theoretical and experimental performance comparison for side feed excitation geometry.

= Ion production costs obtained using global model power balance equation - Employing theoretical Te.

= Ion production costs obtained using global model power balance equation - Employing experimental Te.

= Experimental ion production costs for MPDR 7 – SF plasma source.

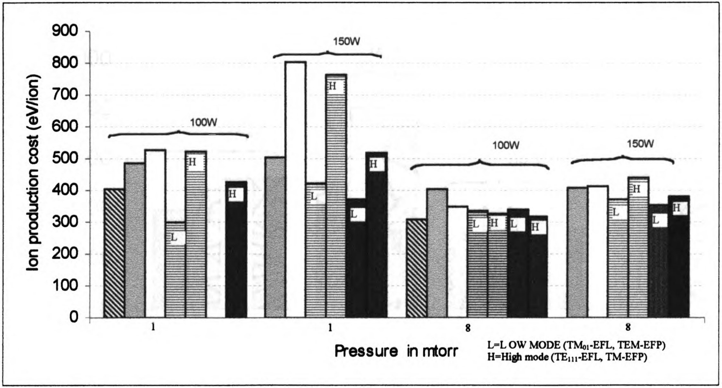

Figure 4.25c Ion production cost versus pressure -Theoretical and experimental performance comparison for the three MPDR plasma sources.

= Ion production costs obtained using global model power balance equation - Employing theoretical Te.

= Ion production costs obtained using global model power balance equation - Employing experimental Te.

= Experimental ion production costs for MPDR 7 – SF plasma source.

= Experimental ion production costs for MPDR 7 – EFL plasma source.

= Experimental ion production costs for MPDR 7 – EFP plasma source.

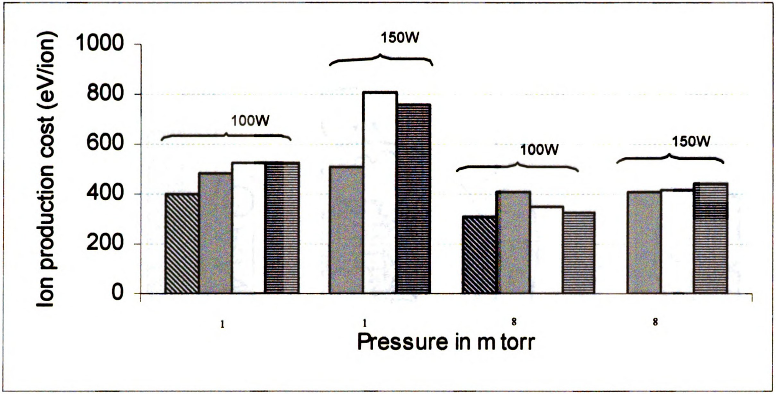

Figure Ion 4.26a production cost versus pressure -Theoretical and experimental performance comparison for the TE_{111} in the SF and EFL excitation geometries.

= Ion production costs obtained using global model power balance equation - Employing theoretical Te.

= Ion production costs obtained using global model power balance equation - Employing experimental Te.

= Experimental ion production costs for MPDR 7 – SF plasma source.

= Experimental ion production costs for MPDR 7 – EFL plasma source.

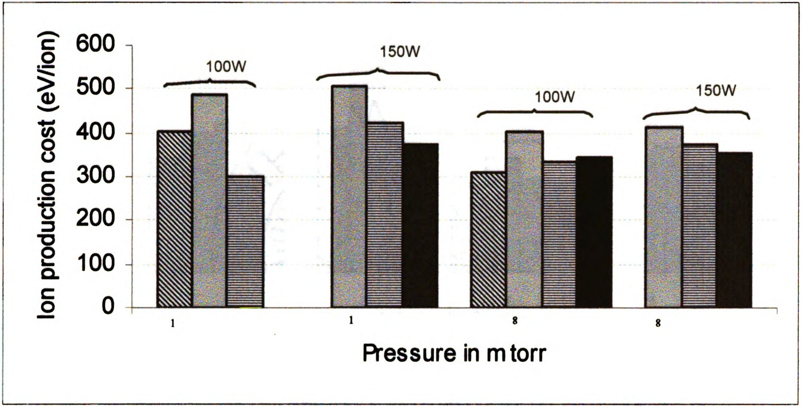

Figure 4.26b Ion production cost versus pressure -Theoretical and experimental performance comparison for the TM_{01} / TEM mode (low modes) in the EFP and EFL excitation geometries.

= Ion production costs obtained using global model power balance equation. Employing theoretical Te.
= Ion production costs obtained using global model power balance equation. Employing experimental Te.

= Experimental ion production costs for MPDR 7 – EFL plasma source.
= Experimental ion production costs for MPDR 7 – EFP plasma source.

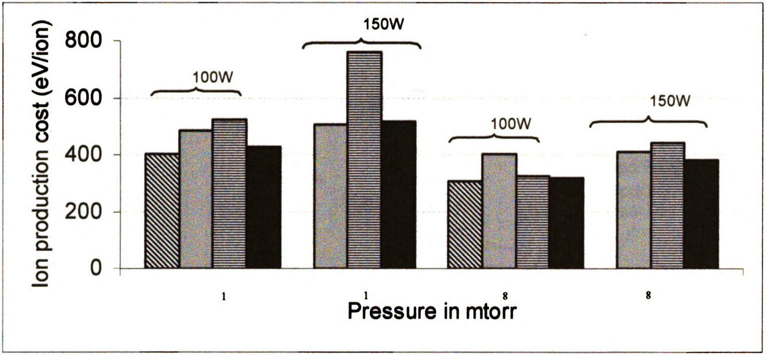

Figure 4.26c Ion production cost versus pressure -Theoretical and experimental performance comparison for the TE_{111} and TM_{01} mode (high modes) in the EFP and EFL excitation geometries.

= Ion production costs obtained using global model power balance equation - Employing theoretical Te.

= Ion production costs obtained using global model power balance equation - Employing experimental Te.

= Experimental ion production costs for MPDR 7 – EFL plasma source.

= Experimental ion production costs for MPDR 7 – EFP plasma source.

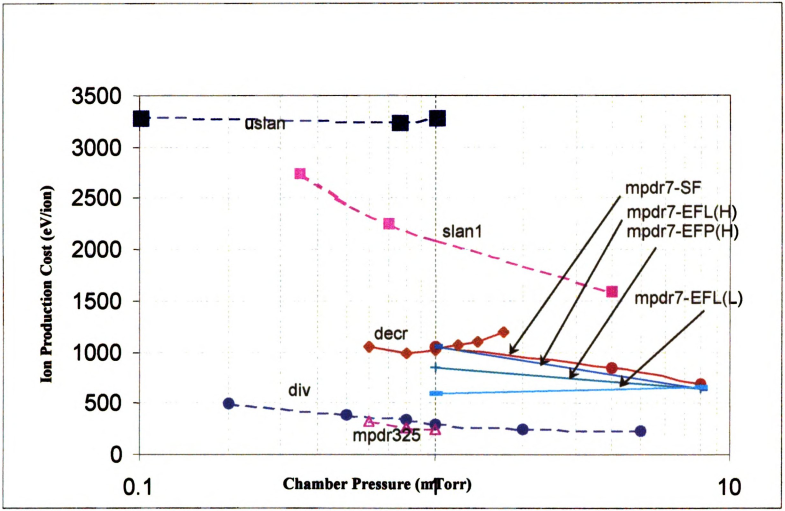

Figure 4.27 Ion production cost versus pressure – A comparison of the investigated sources with different reactor concepts.

Chapter 5

Conclusion

5.1 Work done - Salient features

(1) A new bottom end plate was designed and fabricated that fit the MPDR 7 - SF cavity applicator to a 7cm discharge. The design of this bottom end plate adopter is given in Figure 2.4 in Chapter 2.

(2) Performance characterization of MPDR 7 – SF plasma source is carried out by measuring a selected group of internal variables (X) and output variables (Y).

(3) The influence of coupling structure on the plasma source performance is experimentally evaluated for the three MPDR plasma sources employing three different coupling geometries.

(4) The experimental results are compared with the predictions from the global plasma model and the differences are analyzed.

5. 2 Characterization of MPDR 7 – SF plasma source

5.2.1 Electric fields

(1) A single mode was excited in the cavity which and was identified as TE_{111} mode.

(2) The location of excitation antenna probe does influence the spatial electric field strength in the cavity applicator i.e. the impressed electric fields

measured near the probe are higher than the predictions from single mode excitation. These higher fields are associated with the evanescent probe fields.

(3) The plasma-loaded cavity Q is a function of absorbed power (P_{abs}) and chamber pressure. The plasma loaded cavity Q increases as the pressure decreases. Whereas with an increase in P_{abs}, Q increases slightly.

5.2.2 Electron energy distribution function (EEDF)

(1) The measured EEDFs more closely follow the Druyvesteyn distribution rather then the Maxwellian distribution.

(2) The absence of high-energy electrons supports the utilization of MPDR 7 – SF plasma source in the plasma based processing applications.

5.2.3 Electron temperature and plasma potential

(1) Both electron temperature (T_e) and plasma potential (V_p) are weak functions of P_{abs} and chamber pressure.

5.2.4 Electron density

(1) The lowest and the highest electron densities recorded for the MPDR 7 - SF plasma source are 1.74 x 10^{11}/cm^3 (at 100 Watt and 1 mTorr) and 4.08 x 10^{11}/cm^3 (at 200 Watt and 8 mTorr) respectively.

(2) The MPDR 7 - SF plasma source sustained high-density plasmas (greater than or around 1 x 10^{11}/cm^3) specifically at low pressures and generally under all input conditions.

(3) An increase in electron density has been recorded with a corresponding increase in the operating power and the chamber pressure.

5.3 Experimental results of the three plasma sources

5.3.1 Comparison of the experimental results with the global model

(1) The experimentally measured electron temperatures were higher than the electron temperatures predicted by the global model.

(2) When the experimentally measured electron temperatures are inserted into the global model power balance equation the agreement between the experimental and the global model load lines improves.

(3) The experimentally measured plasma load lines do not match the load lines obtained from the global model equations. The theoretical load lines produce higher electron densities for a given input power P_{abs}. The slopes

of the load lines, i.e. Δn_e vs. ΔP_{abs}, are lower for the experimental data, i.e. as P_{abs} increases the differences the theory an experiment increase.

(4) According to the global model, ion production costs, η, are independent of P_{abs}. However the experimental measurements indicate that ion production costs are functions of P_{abs} and chamber pressure. Ion production costs increase as pressure decreases and increase as power increases.

(5) The experimental measurements demonstrate that the discharge properties vary as P_{abs} varies. The difference between global model predictions and experimental data increases as input power increases and chamber pressure decreases.

5.3.2 Influence of the coupling structure on the source performance

(1) Overall efficiencies do not have a major dependence upon loop or probe applicator excitations but appear to be dependent upon the type of mode excited, i.e. efficiencies depend on TE vs. TM mode excitation and/or on near field coupling.

(2) The three investigated MPDR plasma sources maintained a stable and controllable discharge for the entire input parameter space. However it was observed that it is easier to maintain a discharge under low-pressure conditions by the side feed excitation.

(3) The ion production costs vary considerably with mode excitation i.e. the five different excitation modes yield different efficiencies. These differences can be greater than a factor of two.

(4) The most efficient operation (i.e. the lowest ion production costs) occurs with low mode excitation in the presence of near field coupling, i.e., either low mode loop or probe near field coupling.

(5) "High mode" excitations are the least efficient. Using the results from other investigators, it is unlikely that the efficiency differences can be attributed to applicator conducting wall losses.

(6) The most inefficient operation is with TE_{111} mode excitation. At low pressures of 1mTorr and with TE_{111} mode excitation, the plasma source is more than two times as lossy as excitation with a low mode.

5.4 Comparison of the three investigated sources with other designs

(1) MPDR ion and plasma sources are the most efficient as compared to the other ECR reactor designs.

(2) The larger diameter MPDR 325 plasma source is most efficient when compared to the compact MPDR plasma sources.

5.5 Suggestions for an improved plasma source design

The experiments demonstrate that overall source efficiency is improved by near field coupling. Thus an improved plasma source design may incorporate probe or loop coupling placed very close to the discharge. This type of near field coupling may be optimized by varying the geometry of the coupling structure adjacent to the quartz dome/discharge interface. Experiments also have demonstrated that the TM mode excitation yields better efficiencies than TE mode excitation. Combining these two major experimental observations would result in a plasma source design with end feed probe coupling that excites TEM, or TM modes in the coaxial section, and has near field coupling at the end of the probe. This coupling may be improved by placing a flat disk on the end of the excitation probe.

5.6 Recommendations for the future research

(1) The measured electron temperatures are higher than the predictions from the global model. The measured plasma densities are lower than the densities predicted from the global model and ion production costs are a function of input power. Thus it is thus imperative to verify the accuracy of these experimental measurements by repeating selected experiments. If the differences between global model and experiments are proven to be valid,

then the global plasma model should be modified to accommodate the phenomenon responsible for these differences.

(2) The measured plasma source efficiency is different for the five-excitation modes. The conducting wall losses might be different for each excited mode i.e. they may be relatively lower or higher. Earlier researchers (P. Mak and M. Perrin) have shown that the wall losses are very small i.e. less than 3-5 % of P_{abs}. It is therefore unlikely that the efficiency differences can be attributed to the applicator conducting wall losses. It is still required to validate the earlier results by measuring the wall losses for the five different excitations evaluated in this thesis.

(3) Characterize, in greater detail, the end excited source performance in terms of : 1) P_{abs} vs. ne and T_e, and 2) ne and T_e vs. chamber pressure.

(4) It is seen that the influence of Pabs on the plasma source efficiencies is significant. This might be contributed by the neutral and ion gas heating in the discharge. The influence of gas heating should be evaluated further.

(5) Experimentally verify the concept of an improved plasma source design, which is discussed in the Section 5.5.

5.7 Concluding remarks

The experimental evaluation of the three MPDR ion and plasma sources which is presented in this research work gives a better understanding of the characterization of low pressure and high density argon gas discharge and most importantly the influence of microwave excitation geometry on the plasma discharge parameters.

REFERENCES

[1] J. Asmussen, T. Grotjohn, P. Mak, M. Perrin, "The design and application of electron cyclotron resonance discharges," IEEE Trans. Plasma Sci., vol. 25, pp1196-1221, 1997.

[2] J. Asmussen and J. Root, "Ion generation apparatus and methods for the use thereof," U.S. Patent #4,507,588, (Mar.26, 1985).

[3] J.M. Cook and K. Donohoe, "Etching issues at 0.35 μm and below," Solid State Technol. 34(4), 119-124 (1991).

[4] J. Root and J. Asmussen, "MSU Microwave Ion Source," presented at the MSU/NASA workshop on Advance Propulsion Concepts using Time Varying Electromagnetic Fields, East Lansing, Michigan, Feb. 24-25 (1982).

[5] M. Dahimene and J. Asmussen, 19th EPIB conference, (1984).

[6] M. Dahimene and J. Asmussen, "The performance of a microwave ion source immersed in a multicusp static magnetic field," J. Vac. Sci. Technol., B4(1), 126-130 (1986).

[7] J. Asmussen and M. Dahimene, " The experimental test of a microwave ion beam source in oxygen," J. Vac. Sci. Technol., B5(1), 328-331 (1987).

[8] L. Mahoney and J. Asmussen, " A compact, resonant cavity, five centimeter, multicusp, ECR broad-beam ion source," Rev. Sci.Instrum., 61(1), 285-287 (1990).

[9] L. Mahoney, " The design and testing of a compact electron cyclotron resonant microwave cavity ion source, M.S. Thesis, Dept. of Electrical Engineering, Michigan State University (1989).

[10] A. Srivastava, M. Dahimene, T. Grotjohn and J. Asmussen, " Experimental characterization of a compact ECR ion source," Rev. Sci.Instrum., 63(4), 2556-2558 (1992).

[11] F. Sze, D. Reinhard, B. Mussen and J. Asmussen, " Experimental performance of a large-diameter multipolar microwave plasma disk reactor," J. Vac. Sci. Technol. B8(6), 1759-1762 (1990).

[12] F. Sze, " Design and experimental investigation of a large diameter electron cyclotron resonant plasma source," Ph.D. Thesis, Dept. of Electrical Engineering Michigan State University (1990).

[13] B. Mussen, F. Sze, D. Reinhard, and J. Asmussen, J. Vac. Sci. Technol. B9(6), 3521 (1991).

[14] P. Mak "An experimental evaluation of a 12.5-cm diamter multipolar microwave electron cyclotron resonance plasma source," Ph.D. Thesis, Dept. of Electrical Engineering Michigan State University (1997).

[15] M. Perrin "The electromagnetic evaluation of a compact ECR microwave plasma source," M.S. Thesis, Dept. of Electrical Engineering, Michigan State University (1996).

[16] Micro-Now Instruments, "Owner's manual Model 429B1 microwave power oscillator," (1986).

[17] M. Dahimene, Ph.D. Thesis. Michigan State University, (1987).

[18] I. Langmuir and H. Mott-Smith, Gen.Elec. Rev. 26 (1923).

[19] W. Lochte-Holtgreven, " Plasma diagnostics," North-Holland Publishing Company, Amsterdam (1968).

[20] E. Johnson and L. Malter, " Double-probe method for determination of electron temperature in steady and time-varying gas discharges," Phys. Rev. 76, 1411-1412 (1949).

[21] B. Chapman, "Glow discharge processes," New York, NY: Wiley (1980).

[22] M. J. Druyvesteyn, " Der Niedervoltbogen," Z. Phys. 64, 781-798 (1930).

[23] H. Rundle, D. Clark and J. Deckers, " Electron Energy Distribution Functions in an O_2 discharge," Can. J. Phys. Vol. 51, 144-148 (1973).

[24] S. Burkart, " Coaxial E-field probe for high-power microwave measurement," IEEE Trans. Microwave Theory Tech. MTT-33 (3), 262-265 (1985).

[25] J.A. Hopwood, " Macroscopic properties of a multipolar ECR microwave cavity plasma source for anisotropic silicon etching", Ph.D. Dissertation, Michigan State University, (1990).

[26] M.A.Lieberman and A.J.Lichtenberg, " Principles of Plasma Discharge and Materials Processing", New York: Wiley, (1994).

[27] E.A. McDaniel, " Collisional phenomena in ionized gases, New York ", NY: Wiley, (1964).

[28] J.R. Brophy and P.J. Wilbur, " Simple performance model for ring and line cusp ion thrusters ", AIAA Journal, 23(11), 1731 – 1736, (1985).